

Giant dipole resonance in hot rotating nuclei

D.R. Chakrabarty^{1,a}, N. Dinh Dang^{2,3}, and V.M. Datar⁴

¹ (Ex) Nuclear Physics Division, Bhabha Atomic Research Centre, Mumbai-400085, India

² Nishina Centre for Accelerator-based Science, RIKEN, 2-1 Hirosawa, Saitama 351-0198, Japan

³ Institute of Nuclear Science and Technique, VINATOM, Nghia Do, Cau Giay, Hanoi, Vietnam

⁴ INO Cell, Tata Institute of Fundamental Research, Mumbai-400005, India

Received: 19 November 2015 / Revised: 1 April 2016

Published online: 26 May 2016 – © Società Italiana di Fisica / Springer-Verlag 2016

Communicated by N. Alamanos

Abstract. Over the last several decades, extensive experimental and theoretical work has been done on the giant dipole resonance (GDR) in excited nuclei covering a wide range of temperature (T), angular momentum (J) and nuclear mass. A reasonable stability of the GDR centroid energy and an increase of the GDR width with T (in the range ~ 1 – 3 MeV) and J are the two well-established results. Some experiments have indicated the saturation of the GDR width at high T . The gradual disappearance of the GDR vibration at much higher T has been observed. Experiments on the Jacobi transition and the GDR built on superdeformed shapes at high rotational frequencies have been reported in a few cases. Theoretical calculations on the damping of the collective dipole vibration, characterised by the GDR width, have been carried out within various models such as the thermal shape fluctuation model and the phonon damping model. These models offer different interpretations of the variation of the GDR width with T and J and have met with varying degrees of success in explaining the experimental data. In this review, the present experimental and theoretical status in this field will be discussed along with the future outlook. The interesting phenomenon of the pre-equilibrium GDR excitation in nuclear reactions will be briefly addressed.

1 Introduction

The isovector giant dipole resonance (GDR) in nuclei is described as the collective dipole vibration of protons against neutrons. The GDR built on the nuclear ground state (GS) has been studied, for more than seven decades, in almost all stable nuclei via photoabsorption experiments. The absorption cross-section as a function of γ -ray energy (E_γ) is described, except for very light nuclei, by a single-component (for spherical nuclei) or a multi-component (for deformed nuclei) Lorentzian function

$$\sigma(E_\gamma) = \sum_i \frac{\sigma_{mi} E_\gamma^2 \Gamma_{Di}^2}{(E_\gamma^2 - E_{Di}^2)^2 + E_\gamma^2 \Gamma_{Di}^2}, \quad (1)$$

where E_{Di} , Γ_{Di} and σ_{mi} are, respectively, the resonance energy, width and peak cross-section of the i -th component. In axially-symmetric deformed nuclei there are two components with their energies related to the nuclear deformation. The widths of the GDR components arise due to the damping of the collective motion. The Thomas-Reiche-Kuhn (TRK) sum rule sets a limit to the total integrated cross-section, in the absence of velocity-dependent

and exchange forces [1], as

$$\int_0^\infty \sigma(E_\gamma) dE_\gamma = TRK = 60 \frac{NZ}{A} \text{ MeV} \cdot \text{mb}, \quad (2)$$

with N , Z and A denoting the neutron, proton and mass numbers, respectively, of the nucleus. The experimental integrated cross-sections exceed TRK by a factor $(1 + \alpha)$. For the range of integration up to ~ 30 MeV (spanning the GDR region), the value of α is found to be ~ 0.1 – 0.2 whereas for the integration up to the meson threshold at ~ 140 MeV, α is ~ 0.5 – 0.7 .

Brink and Axel [2, 3] hypothesised about six decades ago that nuclei should manifest the GDR built on excited states with a similar resonance profile as that for the GS. The GDR built on low-lying excited states was first seen experimentally in proton capture reactions [4] and, on continuum states, in the fission fragment γ -ray spectrum of ^{252}Cf [5]. The first observation of the GDR in hot and rotating nuclei, formed in heavy-ion fusion reactions [6], was made about three and a half decades ago. This opened up an extensive field of experimental and theoretical research.

In the microscopic picture of the GDR built on the GS, the resonance is a coherent state of many one particle-one hole ($1p1h$) excitations across the Fermi surface. Its width

^a e-mail: dr_chakrabarty@yahoo.com

Γ_Q ($\sim 4\text{--}5$ MeV in medium-mass and heavy nuclei) comes from the quantal effects and consists of three parts [7] as

$$\Gamma_Q = \Gamma^{LD} + \Gamma^\downarrow + \Gamma^\uparrow. \quad (3)$$

The Landau width Γ^{LD} is essentially the variance $\sigma = \sqrt{\langle E^2 \rangle - \langle E \rangle^2}$ of the energy distribution of $1p1h$ states forming the giant resonance. The spreading width Γ^\downarrow is caused by the coupling of these states to $2p2h$ (doorway) states and the subsequent progressive coupling to complex $np\text{--}nh$ states. The escape width Γ^\uparrow arises from the coupling to the continuum causing direct particle decays feeding the hole states in residual nuclei. In medium-mass and heavy nuclei, the major contribution to Γ_Q comes from Γ^\downarrow . In light nuclei, both Γ^\uparrow and Γ^{LD} are also important.

Within the semiclassical methods such as the Landau-Vlasov kinetic theory [8–10] or the phenomenological approach to nuclear friction [11], Γ^{LD} corresponds to the collisionless damping or one-body dissipation (long mean free path), whereas Γ^\downarrow arises from the collisional damping or two-body dissipation (short mean free path). In the hydrodynamic theory of collective motion, which is based on short mean free paths, the dissipative effects are usually the bulk phenomena caused by the viscous shearing stresses between the adjacent layers of a fluid. In collective theories, the damping of the giant resonance arises from the friction (*i.e.*, viscosity) between the oscillating neutron and proton fluids [12].

The understanding of the GS-GDR width in various nuclei, both spherical and deformed, has provided valuable information on the nuclear structure and the effective nucleon-nucleon interaction in the nuclear medium. The observation of the GDR in heavy-ion fusion reactions, therefore, was recognised as a tool for studying the properties of hot and rotating nuclei over a wide range of temperature T (related approximately to the excitation energy as $E_X \sim AT^2/8$ —see later) and angular momentum J . (In this review, J will be an integer or a half-integer and the unit \hbar will be implicitly assumed.) In all these measurements, the basic observation so far is that for a given nucleus, the GDR energy is nearly constant at all T and J . The integrated photoabsorption cross-section (on excited states) exhausts $\sim 100\%$ of TRK except at very high T (~ 4 MeV). However, the GDR width generally increases with J and T showing that the Brink-Axel hypothesis holds only partially.

The experimental study of the GDR in excited nuclei has developed over the years from a simple inclusive measurement of high-energy γ -rays in a nuclear reaction to elaborate exclusive ones. The need for the exclusive measurements arises from the fact that in a heavy-ion fusion reaction, the compound nucleus (CN) is populated over a wide range of J and the GDR γ -rays are emitted at various decay steps as the nucleus cools down to $T = 0$. An inclusive measurement, therefore, gives an average effect over a range of J and T . Moreover, the spectrum may be contaminated by non-fusion events. Various types of exclusive measurements have been designed over the years. In a measurement in coincidence with the low-energy γ -ray multiplicity, it is possible to suppress the non-fusion

events (expected to populate low J) and extract the J -dependence of the width. A measurement in coincidence with evaporation residues rules out the non-fusion events and that in coincidence with individual residues can select a particular decay chain giving more detailed information. The coincidence with high-spin isomers addresses the high- J region. Attempts have been made to extract the spectrum from the initial steps of decay using the subtraction technique, *i.e.*, from the difference of two spectra measured at different values of E_X and mass (differing by 1 or 2 neutrons) of the CN. Finally, particularly at high energies, the velocity spectrum of the coincident residue nuclei has been used to characterise the effective E_X and mass of the nuclei emitting high-energy γ -rays.

There are different theoretical approaches for understanding the J - and T -dependence of the damping of the GDR. One of these, used widely in the interpretation of the experimental data, is based on the thermal shape fluctuation model (TSFM). Although an increase of the width is generally expected at higher T because the GDR can couple to a denser configuration of states, a detailed consideration revealed [13] that the intrinsic width hardly increases with T . In a simple language, this happens because of the following reasons. First, the damping width of the particle and hole states constituting the GDR shows a weak T -dependence, both being well above and below the Fermi surface, respectively. Second, this weak dependence further cancels out due to the correlation between particle and hole contributions, which reabsorbs the vibration they have excited. The essential arguments in the TSFM for explaining the observed increase in width are the increase of nuclear deformation with J and the increase of shape fluctuation with T . A larger deformation implies a wider splitting of the GDR energies. The Coriolis effect at high rotational frequencies produces further splitting. The observed GDR width, which is an ensemble average over those for various shapes, thus, goes up with T and/or J .

In other theoretical approaches, the damping of the GDR is attributed to the inter-particle collisions, as in the macroscopic collisional damping model (CDM), or to the coupling of the GDR to non-collective particle-hole (ph), particle-particle (pp) and hole-hole (hh) configurations at finite T , as in the microscopic phonon damping model (PDM). According to another model, the observed increase of the width at higher T arises from the higher evaporation widths (related to short lifetimes) of the initial and final states connecting the GDR γ -ray transition.

The experimental study of the GDR over a wide range of J and up to a moderate T (~ 2.5 MeV) had the primary motivation of addressing the nuclear shape evolution and fluctuations and comparing with various theories. The measurements at higher T (up to ~ 5 MeV) addressed the saturation of the GDR width and the vanishing of the collective vibration. The latter phenomenon can, possibly, be related to the liquid-to-gas phase transition in hot nuclei. Besides the excitation of the statistical GDR in an equilibrated system, the excitation of the GDR is possible, at the pre-equilibrium stage, in reactions with charge-asymmetric entrance channels. This phenomenon of pre-equilibrium GDR (PEQGDR) has been studied in

many cases addressing the beam energy dependence, the projectile-target charge asymmetry and the reaction dynamics. Using the GDR as a tool, other important studies were made on the fission dynamics and the isospin symmetry in hot nuclei. This field of research has been reviewed [7, 14–19] earlier by different authors. A compilation of the experimental data on the statistical GDR (except at very high energies) till mid-2006 can be found in ref. [20]. The present review will mainly address the experimental and theoretical aspects of the damping of the GDR with T and J obtained from the studies on the statistical GDR. The other topic touched upon will be the PEQGDR.

2 Experimental methods

In the experimental study of the GDR in excited nuclei, high-energy γ -ray spectra, in the range $E_\gamma \sim 5$ –50 MeV, are measured using various detector configurations. A typical γ -ray spectrum has three characteristic parts as shown in fig. 1. A high-energy ($E_\gamma > 25$ MeV) bremsstrahlung tail, falling exponentially with E_γ and arising from the initial nucleon-nucleon (NN) collisions, is seen at high beam energies (E_b) of ~ 10 MeV/nucleon or more. At $E_\gamma \sim 10$ –25 MeV, a bump, characterising the emission of the GDR γ -rays, is superimposed on a falling spectrum. For $E_\gamma \sim 5$ –10 MeV, the spectrum shows another exponential decrease with a steeper slope. This part arises from the statistical γ -rays emitted below the particle-emission threshold. The overall exponential fall in ~ 5 –25 MeV range arises due to the decrease of the nuclear level density (NLD) with the decrease in E_X . Briefly stated, the method of extracting information on the GDR from the bremsstrahlung-subtracted γ -ray spectra is as follows. A calculation is performed within the statistical model of nuclear reactions in which the GDR strength function as well as the NLD parameters are important inputs. From a comparison of the calculated and experimental spectra, the best set of GDR parameters is obtained. Suitably designed exclusive measurements are performed to extract the dependence of the GDR width on T and J .

2.1 Detector systems

Since the GDR in nuclei has a width of ~ 3 –10 MeV, the energy resolution demanded of the high-energy γ -ray detector is not very stringent. On the other hand, the cross-section decreases exponentially down to a few nb/MeV at the high-energy end of the γ -ray spectrum. The detector should, therefore, have a high detection efficiency and a good line shape of the response function (implying a good confinement of the electromagnetic shower produced by the incident high-energy photon). The background due to pulse pileup and cosmic-ray-induced events has to be reduced to an insignificant level. In general, nuclear reactions produce neutrons and light charged particles with much higher cross-sections compared to the high-energy γ -rays. While charged particles can be stopped in most

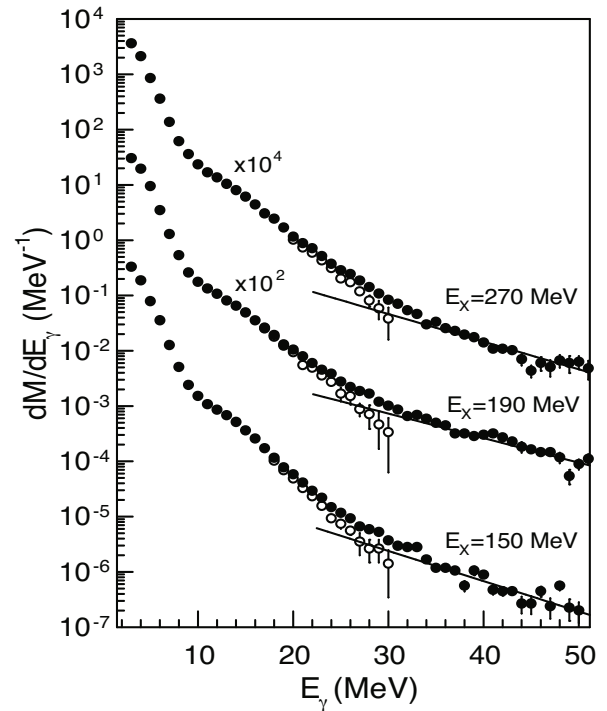


Fig. 1. Measured γ -ray spectra (solid circles) from $^{116}\text{Sn} + ^{12}\text{C}$ and $^{116}\text{Sn} + ^{24}\text{Mg}$ reactions at $E_b = 17$ and 23 MeV/nucleon for different E_X in the compound system. Solid lines represent fits to the bremsstrahlung component for $E_\gamma \geq 35$ MeV. Open circles show bremsstrahlung-subtracted data. (Adapted from ref. [21].)

cases, the most significant background arises from neutrons. These can be discriminated from the γ -rays using the time-of-flight (TOF) technique, which demands a good time resolution of the detector.

In the beginning, NaI(Tl) detectors were used mainly because of their availability. In the very early experiments, multiple detectors of typical dimensions 5''(dia) \times 6''(length) were employed. Many experiments were performed with a single big, typically 10''(dia) \times (10–15)''(length), detector by the Stony Brook, Seattle and KVI groups. In recent years, NaI(Tl) detectors (single or close-packed arrays) are used in some laboratories (IUAC Delhi, PLF Mumbai, Warsaw). The most extensively used high-energy γ -ray detectors are based on BaF₂ scintillators. These have a slightly worse energy resolution than NaI(Tl) but a better timing enabling a good neutron discrimination at a smaller distance from the source. The problem of summing and pileup is avoided by using multiple detectors in a closed-packed array. Moreover, the pulse shapes can discriminate between particles and γ -rays. The BaF₂ arrays, consisting of 7 to ~ 200 elements, have been used by a number of experimental groups. Some examples of these arrays are HECTOR (Milano-Copenhagen) [22], MEDEA (GANIL) [23], LAMBDA (VECC Kolkata) [24] and the arrays of various sizes at Seattle, Stony Brook, RIKEN, Saclay, PLF Mumbai, Michigan, Argonne National Lab (ANL), Oak Ridge and Texas A&M. Bismuth Germanate (BGO) detectors, having a little worse time resolution but

high density and high Z content, implying a better confinement of the electromagnetic shower, have also been employed. Some examples are seen in the experiments performed in Legnaro and Chalk River.

The response of the detector system for various γ -ray energies should be measured in order to analyse the experimental γ -ray spectrum. In the E_γ -range ~ 0.5 – 6.1 MeV, radioactive sources such as ^{22}Na , ^{137}Cs , ^{60}Co , ^{88}Y , Am-Be, Pu- ^{13}C are used. For higher E_γ , different nuclear reactions are employed. Some examples are $^{12}\text{C}(p, p'\gamma)$ and $^{11}\text{B}(d, n\gamma)$ producing $E_\gamma = 15.1$ MeV and $^{11}\text{B}(p, \gamma)$ producing $E_\gamma > 18$ MeV. The measured spectra at specific values of E_γ are compared with simulations of the detector response calculated using Monte Carlo based computer codes such as EGS4 [25] or GEANT4 [26]. A good agreement gives the confidence to use the simulated response function at other γ -ray energies. The theoretical spectrum is generally folded with the response function before comparing with the experiment.

In the exclusive measurements, high-energy γ -rays are measured in coincidence with the low-energy γ -ray multiplicity M_γ (to gate on J), heavy reaction products (to gate on complete or incomplete fusion events) or γ -ray transitions in residue nuclei (to select fusion events or a particular decay chain). The M_γ -detector is an array of small-sized detectors with high intrinsic efficiency and is kept at a close distance from the target in order to have a large solid angle (typically 50–80% of 4π). These consist of BGO detectors (PLF Mumbai, RIKEN, Legnaro, Chalk River, ANL, Daresbury), BaF₂ detectors (VECC, Milano-Copenhagen group) or NaI(Tl) detectors (IUAC Delhi, PLF Mumbai, KVI Groningen, Heidelberg, Strasbourg). The heavy reaction products are detected in mass spectrometers (ANL, Rochester), in parallel-plate avalanche counters (PLF Mumbai, Milano-Copenhagen group, Grenoble, RIKEN, Texas A&M, Darmstadt, GANIL, Saclay) or in detector arrays such as TRASMA (LNS Catania) [27]. The evaporation-residue γ -rays are detected in detector setups with high-energy resolution such as NORDBALL (Copenhagen) [28], GASP (Legnaro) [29], and EUROBALL (Europe) [30]. In some experiments, high-energy γ -rays were measured in coincidence with inelastically scattered projectiles detected in a magnetic spectrometer (NSCL, Michigan).

2.2 Statistical model analysis

The experimentally measured γ -ray spectrum is compared with the statistical model (SM) calculation to extract the properties of the GDR. In low-energy heavy-ion reactions, the assumption of the formation of an equilibrated CN is justified. At higher beam energies, the incomplete fusion (ICF) process and the pre-equilibrium (PEQ) particles emission become important, removing energy from the composite system. However, eventually an equilibrated nucleus is formed within a range of E_X and J which should be properly estimated. The high-energy γ -ray spectrum from the equilibrated nucleus is calculated with the SM incorporating the GDR built on excited states.

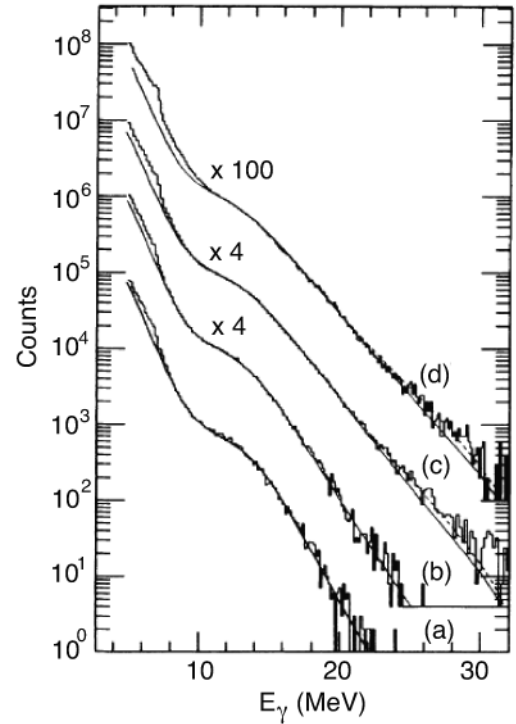


Fig. 2. Gamma-ray spectra and results of the SM calculations in the reactions $^{19}\text{F} + ^{93}\text{Nb}$ at $E_b = 80$ (a), 100 (b) and 160 MeV (d) and $^{16}\text{O} + ^{94}\text{Mo}$ at $E_b = 140$ MeV (c). (Adapted from ref. [31].)

The SM has been discussed by many authors [14, 15] and the essential points are mentioned here. High-energy γ -rays are emitted in competition with various particles from an equilibrated excited nucleus. The cross-section for each depends on the effective transmission coefficient and the final state density. For the γ -ray emission, the effective transmission coefficient is derived from the inverse photoabsorption cross-section on the final state (eq. (1)), which contains the GDR parameters. The final state density is defined mainly by the NLD. An important input to the calculation is, therefore, the E_X - and J -dependence of the NLD. The generally used prescription for this dependence is the Ignatyuk-Reisdorf prescription [32, 33]. This incorporates the E_X -dependence of the nuclear shell effect and the deformation-dependence of the NLD parameter a . At high E_X or T , different T -dependences have also been used [34–36]. The most commonly used computer code for the SM calculation is CASCADE [37] with various modifications done by different groups. The SM has been remarkably successful in describing the experimental cross-sections varying over many orders of magnitude as can be seen in fig. 2.

The temperature T at a certain E_X and J is defined as

$$U = aT^2,$$

where a ($\sim A/7 - A/13 \text{ MeV}^{-1}$) is the NLD parameter [32] describing the increase of the NLD with U or as

$$\frac{1}{T} = \frac{1}{\rho} \left(\frac{d\rho}{dU} \right),$$

where ρ is the NLD at U . The thermal energy U is obtained from E_X after subtracting the rotational energy and the pairing energy. The relevant T corresponds to the final state with excitation energy E_{Xf} after the GDR γ -ray emission where $E_{Xf} = E_{Xi} - E_D$. Here, i and f refer to the initial and the final states, respectively, and E_D is the GDR energy.

The GDR parameters are extracted from a comparison of the experimental and calculated spectra (convoluted with the detector response function). For a more sensitive comparison, both spectra are often presented as linearised plots obtained after dividing them by another calculated spectrum using a constant electric dipole ($E1$) strength [31]. Another way of presenting the data [38] is to divide the experimental spectrum by the ratio of the calculated cross-section and the input absorption cross-section (eq. (1)).

As mentioned earlier, the experimental spectrum arises from all decay steps. In the calculation, the GDR parameters are generally kept the same at all steps and the extracted quantities represent those for an average T and J . While comparing with the theories, therefore, the average T and J should be carefully defined. In another approach [39–44], a calculated or prescribed (T, J)-dependence of the width is incorporated in the SM calculation (instead of keeping it constant at all decay steps). In most of the cases, the comparison of the experiment and theory is done by comparing the measured and calculated GDR widths. However, as has been emphasised in ref. [40], a more demanding test of the theory comes from the comparison of the spectral shapes.

For incorporating the theoretical results on the shape evolution and fluctuations, the absorption cross-sections for a given set of deformation parameters β and γ (we use the same symbol used for gamma-rays) are defined through the GDR parameters as follows. The GDR is generally split into three components [15] with the energy

$$E_{Di} = E_{D0} \exp \left[-\sqrt{\frac{5}{4\pi}} \beta \cos \left(\gamma - \frac{2\pi i}{3} \right) \right], \quad (4)$$

for the i -th component. Here, E_{D0} is the GDR energy for the spherical shape and $\gamma = 0^\circ, 60^\circ$ and 30° corresponds to prolate, oblate and triaxial shapes, respectively. The widths of the components are defined as

$$\Gamma_{Di} = \Gamma_0 \left(\frac{E_{Di}}{E_{D0}} \right)^\delta, \quad (5)$$

where Γ_0 represents the width for the spherical shape. The exponent δ is ~ 1.5 – 2.0 as deduced [45, 46] from the GS systematics. The energies and widths of the components are used to calculate the cross-sections (eq. (1)) and the ensemble-averaged cross-sections (over different shapes) are utilised in the SM calculation at particular values of T and J .

2.3 Angular distribution measurement

The measurement of the angular distribution of the GDR γ -rays provides a tool to derive information on the nuclear

deformation. The angular anisotropy for $E1$ radiation is described as $W(\theta) \sim 1 + a_2 P_2(\cos \theta)$ where P_2 is the Legendre polynomial of order 2. Although in heavy-ion reactions, the nucleus is formed in a highly aligned state (projection M along the beam direction $\ll J$), the angular anisotropy becomes very small for a spherical nucleus for the following reason. From an initial state with spin J_i , the transitions take place to final continuum states with spin J_f with $\Delta J = J_i - J_f = 0$ or ± 1 . Each component has a non-zero a_2 . (For high J , $a_2 = 0.5$ and -0.25 for $\Delta J = 0$ and ± 1 , respectively). For a given E_γ , the NLD of the final states for $\Delta J = 0$ is almost the same as the average NLD for $\Delta J = \pm 1$. The observed a_2 thus adds up to a very small value. For a deformed nucleus, the anisotropy persists because the components separate in γ -ray energy. This topic has been discussed by many authors [7, 14–16]. We therefore present only the main results.

For an axially-symmetric prolate or oblate shape (the case for triaxial shape can be generalised), the GDR splits up into two components corresponding to the vibrations along different axes. For a collective rotation, the rotation axis is perpendicular to the symmetry axis implying $K = 0$, where K is the projection of J along the symmetry axis. In this case, for a prolate nucleus, the γ -rays associated with the low- and high-energy components have (for $J \gg 0$) $a_2 = -0.25$ and $+0.125$, respectively, where θ is measured with respect to the beam direction. For an oblate shape, these values are just reversed. In non-collective (NC) rotations, the rotation axis is parallel to the symmetry axis implying $K \sim J$. In this case, the above a_2 coefficients for an oblate shape are -0.25 and $+0.5$ with reversed values for a prolate shape. In some experiments (for example, in γ -ray measurements in coincidence with fission fragments), it is possible to measure the angular distribution with respect to the rotation axis. The angular anisotropy gets enhanced with the above a_2 coefficients being multiplied by -2.0 . In an actual case, each GDR component has a width and the anisotropy has to be convoluted with the strength function. This dilutes the anisotropy and results in a change of sign of the a_2 coefficient, as a function of E_γ , across the mean GDR energy. This feature is thus an indicator of the nuclear deformation. A further dilution of anisotropy arises from a distribution of the angle between the spin and symmetry axis at finite T . This is termed as the orientation fluctuation. In spite of these dilutions, in many cases, it has been possible to derive information on the nuclear deformation from the angular-distribution measurements supplementing that obtained from the spectral shapes.

2.4 Multiplicity-gated measurements

The inclusive experimental spectrum comes from a range of E_X and J as discussed above. For disentangling the effect of J , exclusive measurements have been made in coincidence with M_γ as mentioned earlier. The CN populated at a higher angular momentum J_{CN} results in a higher residue spin J_R after cooling and, hence, to a higher M_γ . Conversely, M_γ is a measure of J_{CN} . In practice, however,

the method is not as straightforward. The low-energy γ -rays are detected in a M_γ -detector array of a finite granularity and efficiency. For a given M_γ , the number of detectors fired, called the fold F , is less than M_γ because of the finite efficiency and multiple hits in an individual detector. The response function of M_γ to F , therefore, needs to be known. This depends on the geometry of the array and the E_γ -dependent efficiency which can be simulated or measured experimentally [47].

Different methods [48–50] have been used for analysing the measured F -gated γ -ray spectra. In one method [48], the M_γ -distribution for a certain F -window is calculated using the above mentioned response function. The corresponding J_{CN} -distribution, needed in the SM calculation, is obtained using an approximate relation $J_{CN} = 2M_\gamma + J_S$. Here, the parameter J_S represents the angular momentum carried away by the evaporated particles and statistical γ -rays below the particle-emission threshold. In another method [50], first the J_R -distribution is calculated with the SM for each J_{CN} . A convolution of these distributions with the J_R -to- F response function is then used to derive the J_{CN} -distributions for various F -windows. The J_R -to- F response is obtained assuming a combination of $\Delta J = 1$ and $\Delta J = 2$ γ -ray transitions along the yrast line and multiplying the resultant M_γ distribution by the M_γ -to- F response for each J_R . From the CASCADE code, the average $\langle J \rangle$ and $\langle T \rangle$ are calculated for each F -window and the J - and T -dependent GDR parameters are thus derived from the measured spectra.

The mapping of J_{CN} to J_R actually depends on the energy of the intermediate γ -rays emitted and a Monte Carlo approach is, therefore, necessary for a correct analysis. This being time consuming, a faster method has been devised [51] to calculate the exact J_R -gated γ -ray spectrum by making a number of SM calculations. In the first calculation, the J -dependent cross-sections are stored for various E_X , A , Z and E_γ encountered in the decay cascade. Subsequent SM calculations, done with the stored cross sections for each combination, create the J_R -distribution in various residues and the cross-section matrix $\sigma(E_\gamma, J_R)$ is thus obtained. This is converted to the $\sigma(E_\gamma, F)$ matrix after convoluting with the J_R -to- F response mentioned earlier. The modified CASCADE code for obtaining the first matrix is termed as the simulated Monte Carlo Cascade (SMCC) because it provides the results of a Monte Carlo SM calculation. By projecting the second matrix on the E_γ -axis for different F , the F -gated γ -ray spectra are finally obtained.

2.5 Evaporation residue- and isomer-gated measurements

Besides the exclusive measurements described in the earlier subsection, two other types of measurements are those in coincidence with evaporation residues (ER) and isomers. The ER detection is done by catching the residues in a charged particle detector such as a parallel-plate avalanche counter (PPAC), phoswich detector arrays or other elaborate detector systems including recoil mass separators. The TOF of the particles, the energy deposited in

the detector and the particle identification are used in different combinations to characterise the ER. In some experiments, the ER-gating is done by using the characteristic low-energy γ -rays from the residue nuclei detected in high-efficiency detector arrays with a good energy resolution. For gating with high J , some experiments report measurements in coincidence with high-spin isomers in suitable residue nuclei. The delayed γ -rays are measured in detectors around a catcher foil (to stop the residues) placed at a suitable distance downstream of the target. The time spectrum of these γ -rays measured in coincidence with prompt γ -rays from the target, is used to characterise the particular isomer. The analysis of the data in coincidence with ER or high-spin isomers requires the use of a Monte Carlo version of the SM code.

3 Theoretical models

The theoretical models for describing the GDR damping can be classified into two categories based on the microscopic foundation and the semiclassical approaches using macroscopic theories.

The model Hamiltonian adopted in microscopic theories of collective excitations has the form

$$H = H_{mf} + H_{pair} + H_{res}, \quad (6)$$

where H_{mf} , H_{pair} , and H_{res} describe the motion of independent nucleons in the mean field, the monopole pairing interaction between them, and the residual two-body interaction, respectively. Their explicit forms in terms of the creation and annihilation operators a_k^\dagger and a_k of particles on orbitals k , with single-particle energies ϵ_k , are given as

$$\begin{aligned} H_{mf} &= \sum_k \epsilon_k a_k^\dagger a_k, \\ H_{pair} &= - \sum_{kk'} G_{kk'} a_k^\dagger a_{\bar{k}'}^\dagger a_{\bar{k}} a_k, \\ H_{res} &= \sum_{kk' ll'} V_{kk' ll'} a_k^\dagger a_{k'}^\dagger a_l a_l - \sum_k V(k). \end{aligned} \quad (7)$$

In eq. (7), the sums over proton and neutron indices are implied. The symbol \bar{k} denotes the conjugate state (for example, $|j\bar{m}\rangle \equiv (-)^{j+m}|j-m\rangle$ in the spherical basis). The last sum in H_{res} represents the interaction already included to generate the mean field, such as the Hartree-Fock (HF) field or that described by the realistic Woods-Saxon potentials.

In open-shell nuclei, the effect of monopole pairing is usually included in the Hartree-Fock-Bogoliubov (HFB) theory or the BCS theory (the special case of the HFB theory with constant pairing $G_{kk'} = G$). The HFB or BCS equations can be derived by using the formalism of quasiparticles according to the Bogoliubov transformation

$$\alpha_k^\dagger = u_k a_k^\dagger - v_k a_{\bar{k}}, \quad \alpha_k = (a_k^\dagger)^\dagger, \quad u_k^2 + v_k^2 = 1, \quad (8)$$

where u_k and v_k are the Bogoliubov coefficients, defined later. This allows the Hamiltonian (eq. (7)) to be expressed in terms of the quasiparticle operators α_k^\dagger and α_k

and to carry out all derivations within the quasiparticle representation.

The extension of the microscopic approach such as the RPA (QRPA) to finite T is carried out by replacing the expectation value of an observable \mathcal{O} in the ground state with that in the grand canonical ensemble (GCE), *viz.*,

$$\langle \mathcal{O} \rangle \equiv \text{Tr}[\mathcal{O}e^{-\beta(H-\lambda\hat{N})}] / \text{Tr}e^{-\beta(H-\lambda\hat{N})}, \quad \beta = 1/T. \quad (9)$$

Since the particle number fluctuates within the GCE, the Lagrange multiplier λ (chemical potential) is introduced to preserve the average particle number $N = \langle \hat{N} \rangle$ at each T .

To derive the equations to determine the GDR properties, *viz.*, its energy and width or the full strength function, various equivalent methods, such as the variational principle, linearisation of equation of motion, or double-time Green functions [52], are applied with respect to the Hamiltonian (eq. (7)) or its quasiparticle representation.

3.1 Finite-temperature random-phase approximation

The early microscopic approaches in the study of collective excitations at finite T were formulated by extending the existing approaches at $T = 0$ to non-zero T . Among them the most popular one is the theory of small amplitude vibrations, called the random-phase approximation (RPA), or quasiparticle RPA (QRPA) in the quasiparticle representation including pairing.

The QRPA at finite T (FT-QRPA) describes the excitations generated by the coherent superpositions of the quasiparticle-pair operators in thermal equilibrium. These operator superpositions define the QRPA phonon operator Q_ν^\dagger in the form

$$Q_\nu^\dagger = \sum_{k>l} \left(\frac{X_{kl}^\nu A_{kl}^\dagger - Y_{kl}^\nu A_{kl}}{\sqrt{D_{kl}}} + \frac{x_{kl}^\nu B_{kl}^\dagger - y_{kl}^\nu B_{kl}}{\sqrt{d_{kl}}} \right), \quad (10)$$

with

$$\begin{aligned} A_{kl}^\dagger &= \alpha_k^\dagger \alpha_l^\dagger, & B_{kl}^\dagger &= \alpha_k^\dagger \alpha_l, \\ A_{kl} &= (A_{kl}^\dagger)^\dagger, & B_{kl} &= (B_{kl}^\dagger)^\dagger. \end{aligned} \quad (11)$$

The average values of the commutators between the quasiparticle pair creation A_{kl}^\dagger and annihilation A_{kl} operators, and those between quasiparticle scattering B_{kl}^\dagger and B_{kl} operators in the GCE are

$$\begin{aligned} \langle [A_{kl}, A_{k'l'}^\dagger] \rangle &= \delta_{kk'} \delta_{ll'} D_{kl}, & D_{kl} &= (1 - n_k - n_l), \\ \langle [B_{kl}, B_{k'l'}^\dagger] \rangle &= \delta_{kk'} \delta_{ll'} d_{kl}, & d_{kl} &= (n_l - n_k), \end{aligned} \quad (12)$$

where the quasiparticle occupation number $n_k \equiv \langle \alpha_k^\dagger \alpha_k \rangle$ is described by the Fermi-Dirac distribution of non-interacting quasiparticles, *viz.*,

$$n_k = \frac{1}{e^{\beta E_k} + 1}, \quad E_k = \sqrt{(\epsilon_k - \lambda - Gv_k^2) + \Delta(T)^2}. \quad (13)$$

The pairing gap $\Delta(T)$ in the quasiparticle energy E_k is found as the solution, at finite T , of the gap equations such as the finite-temperature BCS (FT-BCS), the modified BCS (MBCS) or the FTBCS1 equation. The last two cases include the effect of the thermal fluctuation of the quasiparticle numbers which is neglected in the conventional FT-BCS theory (see sect. 3.2). The Bogoliubov coefficients u_k and v_k are expressed in terms of the single-particle energy ϵ_k , the chemical potential λ , and the quasiparticle energy E_k as

$$u_k^2 = [1 + (\epsilon_k - \lambda - Gv_k^2)/E_k]/2$$

and

$$v_k^2 = [1 - (\epsilon_k - \lambda - Gv_k^2)/E_k]/2.$$

The term Gv_k^2 is often omitted because of its small contribution or its effect being already taken into account in the phenomenological mean-field, such as the Woods-Saxon, potential.

The FT-QRPA equations are obtained by linearising the equations of motion $\langle [A_{kl}^\dagger, [H-\lambda N, Q_\nu^\dagger]] \rangle = \omega \langle [A_{kl}^\dagger, Q_\nu^\dagger] \rangle$ and $\langle [B_{kl}^\dagger, [H-\lambda N, Q_\nu^\dagger]] \rangle = \omega \langle [B_{kl}^\dagger, Q_\nu^\dagger] \rangle$ under the assumption that the phonon operators (eq. (10)) are ideal boson operators, *viz.*, they satisfy the equation $\langle [Q_\nu, Q_{\nu'}^\dagger] \rangle = \delta_{\nu\nu'}$. Together with eq. (12), this equation leads to the normalisation condition

$$\sum_{k>l} (X_{kl}^\nu X_{kl}^{\nu'} - Y_{kl}^\nu Y_{kl}^{\nu'} + x_{kl}^\nu x_{kl}^{\nu'} - y_{kl}^\nu y_{kl}^{\nu'}) = \delta_{\nu\nu'}. \quad (14)$$

Equation (12) is often referred to as the quasi-boson approximation (QBA). The QBA leads to a set of linear equations for the eigenvectors $X_{kk'}^\nu$, $Y_{kk'}^\nu$, $x_{kk'}^\nu$ and $y_{kk'}^\nu$, as well as the eigenvalues ω_ν , which are the energies of phonon excitations.

The FT-RPA and FT-QRPA equations were derived for the first time [53, 54] by using a separable residual interaction $V_{kk' ll'} = \kappa^{(L)} F_{kl}^{(L)} (F_{l'k'}^{(L)})^*$, where $\kappa^{(L)}$ is the strength parameter (positive for isovector and negative for isoscalar ph matrix elements) and L denotes the multipolarity. The use of the separable force allows the elimination of the amplitudes $X_{kk'}^\nu$, $Y_{kk'}^\nu$, $x_{kk'}^\nu$ and $y_{kk'}^\nu$ to obtain a dispersion equation for the phonon energies ω in the form [54]

$$\begin{aligned} 1 - \kappa^{(L)} \sum_{k>l} [F_{kl}^{(L)}]^2 \left[\frac{[u_{kl}^{(+)}]^2 (E_k + E_l) D_{kl}}{\omega^2 - (E_k + E_l)^2} \right. \\ \left. - \frac{[v_{kl}^{(-)}]^2 (E_k - E_l) d_{kl}}{\omega^2 - (E_k - E_l)^2} \right] = 0, \end{aligned} \quad (15)$$

with $u_{kk'}^{(+)} = u_k v_{k'} + v_k u_{k'}$, $v_{kk'}^{(-)} = u_k u_{k'} - v_k v_{k'}$. In the absence of pairing, $u_{ph}^{(+)} = 1$ and $v_{pp}^{(-)} = v_{hh'}^{(-)} = 0$, so the second sum on the left-hand side of eq. (15) vanishes, bringing it back to the RPA dispersion equation [53, 55].

The set of FT-QRPA equations has been derived, using the general residual ph interaction, by various authors [56–60]. The FT-RPA and FT-QRPA equations were

used in the early microscopic calculations of the GDR energy and the distribution of $E1$ transition probabilities at finite T [55–62].

At $T = 0$, the spectrum of phonon excitations, obtained as solutions of the RPA (QRPA) equation, represents the distribution of independent coherent ph (two-quasiparticle) excitations. In other words, the RPA (QRPA) can describe only the GDR energy and its Landau width Γ^{LD} , which is a small fraction of the GDR width in medium-mass and heavy nuclei. At $T \neq 0$, d_{kl} becomes finite because of the distortion of the Fermi surface, leading to the pp and hh transitions in addition to the ph ones, which exist already at $T = 0$. The contribution of pp and hh transitions is present as the last sum on the left-hand side of eq. (15). This is related to the new two-quasiparticle poles ($E_k - E_l$), generated by the quasiparticle scattering operators B_{kl}^\dagger and B_{kl} , which lead to the new solutions ω between them. However, the numerical calculations performed in refs. [55–59, 61] did not show any significant change of the Landau width Γ^{LD} with T . The new phonon states owing to the new quasiparticle poles turn out to be non-collective, whose corresponding $E1$ transition probabilities are small. The fact that the FT-QRPA (RPA) represents the independent phonon excitations also means that there is no coupling between the collective ph phonons, which generate the GDR at $T = 0$, with each other and with the new pp and hh non-collective states that appear at $T \neq 0$. Therefore, no increase in the spreading width is obtained within the FT-QRPA.

3.2 Thermal fluctuation of pairing field

Within the conventional FT-BCS theory, the temperature-dependent gap $\Delta(T)$ and the chemical potential $\lambda(T)$ are defined by the equations

$$\Delta = G \sum_k (1 - 2n_k) u_k v_k, \quad (16)$$

$$N = 2 \sum_k [(1 - 2n_k) v_k^2 + n_k]. \quad (17)$$

They produce a pairing gap $\Delta(T)$ which collapses at a critical temperature $T_c \simeq 0.57\Delta(0)$ signaling the phase transition from the superfluid to normal phase as in infinite systems. However, atomic nuclei are finite systems exhibiting large thermal fluctuations whose effects cannot be neglected. Several approaches have been proposed for taking into account the thermal fluctuation of the pairing field. These are the macroscopic approach based on the Landau theory of phase transition [63–65], the static-path approximation (SPA) [66, 67], the shell model [68] and Monte Carlo shell models [69], the ensemble-averaged pairing [70], the modified Hartree-Fock-Bogoliubov (MHFB) theory [71], which, in the limit of constant pairing, is the modified BCS (MBCS) theory [72–74], and the FT-BCS1 [75]. Among them, the MHFB (MBCS) and the FTBCS1 take into account the quasiparticle-number fluctuations (QNF) neglected in the FT-BCS theory.

Within the macroscopic approaches or the SPA, thermal fluctuations lead to the average pairing gap in the

form

$$\langle \Delta(T) \rangle = \frac{\int_0^\infty \Delta e^{-\beta F(\Delta)} d\mathcal{D}[\Delta]}{\int_0^\infty e^{-\beta F(\Delta)} d\mathcal{D}[\Delta]}, \quad (18)$$

with the free energy $F(\Delta)$ and the metric $\mathcal{D}[\Delta] = \Delta d\Delta$ [66, 67] taken based on the two-dimensional character of the pairing fields $\zeta = \Delta e^{i\theta}$ with the gauge angle θ [76].

In the approach based on the three principal statistical ensembles [70], an exact gap Δ_α is defined from the pairing energy $\mathcal{E}_{pair}^{(\alpha)}$ as,

$$\Delta_\alpha = \sqrt{-G\mathcal{E}_{pair}^{(\alpha)}}, \quad \mathcal{E}_{pair}^{(\alpha)} = \langle \mathcal{E} \rangle_\alpha - \langle \mathcal{E} \rangle_\alpha^{(0)},$$

$$\langle \mathcal{E} \rangle_\alpha^{(0)} \equiv 2 \sum_j \Omega_j \left[\epsilon_j - \frac{G}{2} f_j^{(\alpha)} \right] f_j^{(\alpha)}, \quad (19)$$

where α denotes the GCE, the canonical ensemble (CE) or the micro-canonical ensemble (MCE), and $f_k^{(\alpha)}$ gives the ensemble average of the state-dependent occupation numbers. The total energies $\langle \mathcal{E} \rangle$ within the GCE and CE are given as

$$\langle \mathcal{E} \rangle_\alpha = - \frac{\partial \ln \mathbf{Z}(\beta)_\alpha}{\partial \beta}, \quad (20)$$

with the grand partition function $\mathcal{Z}(\beta, \lambda)$ [1] given by

$$\mathcal{Z}(\beta, \lambda) = \iint_0^\infty \rho(\mathcal{E}, N) e^{-\beta(\mathcal{E} - \lambda N)} dN d\mathcal{E}$$

$$= \sum_n e^{\beta \lambda n} Z(\beta, n). \quad (21)$$

Here, $Z(\beta, n)$ denotes the partition function at temperature T and particle number fixed at n as

$$Z(\beta, n) = \sum_s p_s(\beta, n), \quad p_s(\beta, n) = d_s^{(n)} e^{-\beta \mathcal{E}_s^{(n)}}. \quad (22)$$

In eq. (22) $\mathcal{E}_s^{(n)}$ are the exact eigenvalues obtained by diagonalising the pairing Hamiltonian [77]. Within the GCE, the chemical potential λ should be chosen as a function of T so that the average particle number $\langle N \rangle$ of the system remains equal to N . The summations over n and s in eqs. (21) and (22) take into account the degeneracy $d_s^{(n)}$ of each s^{th} state in the n -particle system. For the total energy within the MCE, one puts $\mathcal{E}_{pair}^{(\alpha)} \equiv \mathcal{E}_{pair}(s)$ with $\langle \mathcal{E} \rangle_{\text{MCE}} \equiv \mathcal{E}_s^{(N)}$. The term $\langle \mathcal{E} \rangle_\alpha^{(0)}$ denotes the contribution from the energy $2 \sum_k \epsilon_k f_k^{(\alpha)}$ of the single-particle motion described by the first term on the right-hand side of the Hamiltonian (eq. (7)) and the energy $-G \sum_k [f_k^{(\alpha)}]^2$ of the uncorrelated single-particle configurations caused by the pairing interaction in the Hamiltonian.

The MBCS and FTBCS1 take the thermal fluctuations of the pairing field into account in terms of the QNF. Within the MBCS this is realised by means of the secondary Bogoliubov transformation from quasiparticle operators α_k^\dagger and α_k to modified quasiparticle operators, $\bar{\alpha}_k^\dagger$

and $\bar{\alpha}_k$, *viz.*,

$$\begin{aligned}\bar{\alpha}_k^\dagger &= \sqrt{1 - n_k} \alpha_k^\dagger - \sqrt{n_k} \alpha_{\bar{k}}, \\ \bar{\alpha}_{\bar{k}} &= \sqrt{1 - n_k} \alpha_{\bar{k}} + \sqrt{n_k} \alpha_k^\dagger.\end{aligned}\quad (23)$$

The MBCS equations obtained by using this transformation have the form

$$\bar{\Delta} = G \sum_k \left[(1 - 2n_k) u_k v_k - \sqrt{n_k(1 - n_k)} (u_k^2 - v_k^2) \right], \quad (24)$$

$$N = 2 \sum_k \left[(1 - 2n_k) v_k^2 + n_k - 2\sqrt{n_k(1 - n_k)} u_k v_k \right], \quad (25)$$

where the last terms on the right-hand side of eqs. (24) and (25) arise because of the finite QNF $\sqrt{\delta \mathcal{N}_k^2} \equiv \sqrt{n_k(1 - n_k)}$.

The FTBCS1 uses the exact relation

$$\begin{aligned}\langle D_k D_l \rangle &= \langle D_k \rangle \langle D_l \rangle + \delta \mathcal{N}_{kl}, \\ \delta \mathcal{N}_{kl} &= \langle \mathcal{N}_k \mathcal{N}_l \rangle - \langle \mathcal{N}_k \rangle \langle \mathcal{N}_l \rangle,\end{aligned}\quad (26)$$

and the mean-field contraction for the term

$$\delta \mathcal{N}_{kl} \simeq 2\delta \mathcal{N}_k^2 \delta_{kl},$$

with the quasiparticle occupation number

$$n_k = \frac{1}{2}(1 - \langle D_k \rangle),$$

to derive the gap equation as a sum of a level-independent part Δ and a level-dependent part $\delta \Delta_k$ in the form

$$\Delta_k = \Delta + \delta \Delta_k, \quad (27)$$

where

$$\Delta = G \sum_{k'} \langle D_{k'} \rangle u_{k'} v_{k'}, \quad \delta \Delta_k = 2G \frac{\delta \mathcal{N}_k^2}{\langle D_k \rangle} u_k v_k. \quad (28)$$

Despite the quantitative difference, the pairing gaps obtained in these approaches have a prominent common feature that they do not collapse at the critical temperature T_c , but monotonically decrease with increasing T and remain finite at $T \gg T_c$. In other words, thermal fluctuations in finite systems such as nuclei smooth out the sharp superfluid-to-normal phase transition of infinite systems, as shown in fig. 3.

The effect of pairing on the GDR energy within the FT-QRPA was obtained in ref. [61] for the spherical nucleus ^{58}Ni . When the QRPA phonon operators are constructed from the superpositions of two FTBCS quasiparticle operators, the GDR energy weakly decreases with T in the ranges $0 < T \ll T_c$ and $T > T_c$. Near $T = T_c$, it shows a sudden bending down with a break at T_c . The same feature was reported within the FT-QRPA for the rotating deformed nucleus ^{164}Er in ref. [60]. The decrease of the GDR energy with T is a feature of FTRPA but the sudden bending at $T = T_c$ is caused by the collapse of the pairing gap at $T = T_c$ within the FTBCS. Thermal fluctuations of the pairing field smooth out this singularity as has been shown in ref. [62].

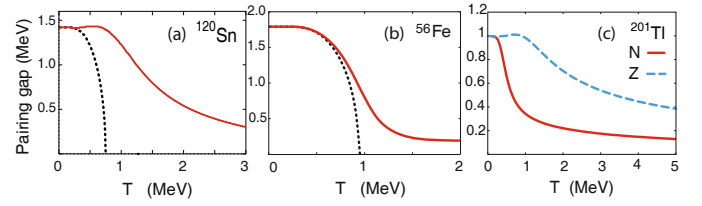


Fig. 3. (Colour online) T -dependence of pairing gaps. (a) BCS (dotted line) and MBCS (solid line) gap (eq. (24)) for neutrons in ^{120}Sn . (b) BCS (dotted line) and level-weighted FTBCS1 (solid line) gap (eq. (27)) for neutrons in ^{56}Fe . (c) Exact canonical gaps for neutrons (solid line) and protons (dashed line) in ^{201}Tl . (Adapted from refs. [71, 75, 78].)

3.3 Quasiparticle-phonon model

In order to describe the GDR spreading width Γ^\downarrow , the coupling to $2p2h$ configurations need to be taken into account. This is realised within the quasiparticle-phonon model (QPM) [79] by constructing the excited states, which are generated by an excitation operator, consisting of one and two QRPA phonon operators, acting on the QRPA phonon vacuum $|0\rangle$.

This approach has been extended to finite temperatures in ref. [80] where the phonon structure, *viz.*, its energy ω_{Li} as well as the X and Y amplitudes, are found within the FT-QRPA. The resulting approach is referred to as FT-QPM. The equation for finding the energies η of the excited states at finite T within the FT-QPM has the form

$$\det \left\| [\omega_{Li}(T) - \eta] \delta_{ii'} - \frac{1}{2} \sum_{\substack{L_1 i_1 \\ L_2 i_2}} \frac{U_{L_1 i_1}^{L_2 i_2}(Li, T) U_{L_1 i_1}^{L_2 i_2}(Li', T) (1 + \nu_{L_1 i_1} + \nu_{L_2 i_2})}{\omega_{L_1 i_1}(T) + \omega_{L_2 i_2}(T) - \eta} \right\| = 0, \quad (29)$$

where the phonon occupation numbers ν_{Li} follow the Bose-Einstein distribution

$$\nu_{Li} = 1/[\exp(\beta \omega_{Li}) - 1]$$

for ideal bosons and $U_{L_1 i_1}^{L_2 i_2}(Li, T)$ are functions of X and Y amplitudes, obtained within the FT-QRPA (see eq. (19) in ref. [80]). Compared to the spectrum of one-phonon excitations within the FT-QRPA, the spectrum of excited states given by eq. (29) is richer because of the solutions between the two-phonon poles $\omega_{L_1 i_1}(T) + \omega_{L_2 i_2}(T)$. This enrichment implies the spreading of the GDR distribution obtained within the FT-QRPA. In this way the GDR acquires a spreading width Γ^\downarrow within the QPM.

The strength function of the GDR ($L = 1$) is calculated within the QPM as

$$b(EL, \eta) = \frac{1}{\pi} \text{Im} \left\{ \sum_{ii'} \mathcal{A}_{ii'}(\eta + i\varepsilon) \mathcal{M}_{Li} \mathcal{M}_{Li'} / \mathcal{F}(\eta + i\varepsilon) \right\}, \quad (30)$$

where \mathcal{M}_{Li} are the matrix elements of the EL transitions from thermal equilibrium to the one-phonon excitations, $\mathcal{F}(\eta+i\varepsilon)$ is the determinant of the left-hand side in eq. (29) at complex energies $\eta+i\varepsilon$, $\mathcal{A}_{ii'}$ are its minors, and ε is a smoothing parameter, which may take into account the escape width Γ^\uparrow .

The GDR strength functions for ^{58}Ni and ^{90}Zr , calculated [80] by using either the pairing gap smoothed by thermal fluctuations within the macroscopic approach [61, 63–65] or a constant pairing gap, are rather insensitive to the change of T . This is exemplified in fig. 4(a) for ^{90}Zr . The values of the full width at half maximum (FWHM) of the GDR main peak, obtained within the FT-QPM, are ~ 1.9 , 2.1 and 2.0 MeV, respectively, at $T = 0, 1$ and 3 MeV. These results are in disagreement with the experimental observations. For example, the results of the measurement in ref. [38] showed that the GDR width in ^{90}Zr is ~ 9.7 MeV at $T \sim 1.7$ MeV, which is ~ 5.5 MeV more than the GS-GDR width of ~ 4.2 MeV.

3.4 Particle-vibration coupling model

When one phonon in the two-phonon component of the excitation operator is non-collective, *i.e.*, dominated by a single two-quasiparticle component, the treatment of the GDR damping within the QPM is equivalent to that offered by the particle-vibration coupling model (PVCVM) [81–84]. In the latter, the spreading width Γ^\downarrow is caused by the coupling between ph configurations and phonons, which represent the surface vibrations. A similar model has been developed in ref. [84] by taking into account the coupling to $ph \otimes$ phonon configurations and using the Landau-Migdal effective interaction. The PVCVM has been extended to finite temperatures in ref. [85] to study the T -dependence of the GDR spreading width Γ^\downarrow .

The strength function of the EL excitations with multipolarity L is calculated within this model as

$$S_a(E) = \frac{S_0}{\pi} \times \frac{\Gamma(E+i\varepsilon)/2 + \varepsilon}{[E_a - E - \Delta E_a(E+i\varepsilon)]^2 + [\Gamma(E+i\varepsilon)/2 + \varepsilon]^2}, \quad (31)$$

where ε is a smoothing parameter. The energy shift ΔE_a and the width Γ are calculated as the real and imaginary parts, respectively, of the self-energies for single particles and vibrations. These are functions of single-particle and phonon occupation numbers, as well as the particle-vibration coupling strength. The energies of the vibrations (phonon energies) are found by solving the FT-RPA equation

$$1 + \kappa F G_L^0(\omega, T) = 0, \quad (32)$$

with

$$G_L^0(\omega, T) = \sum_{kl} \frac{\langle k || R_0(\partial U / \partial r) Y_L || l \rangle^2}{F^2} \times \frac{f_l - f_k}{(2L+1)} \left(\frac{1}{\epsilon_k + \epsilon_l - \omega} + \frac{1}{\epsilon_k - \epsilon_l + \omega} \right), \quad (33)$$

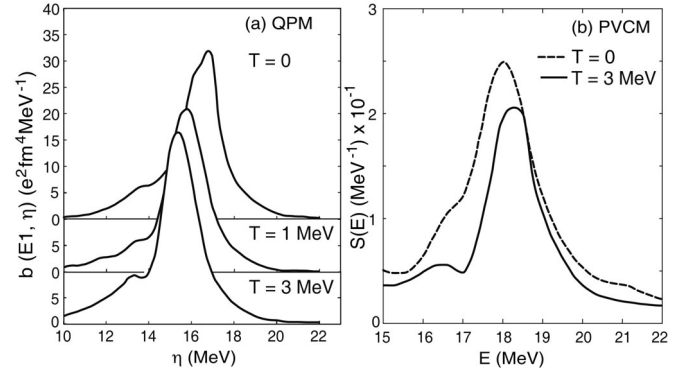


Fig. 4. Calculated GDR strength function for ^{90}Zr as a function of dipole excitation energy, η in (a) and E in (b). Left panel shows the results of QPM at $T = 0$ – 3 MeV using the smoothing parameter $\varepsilon = 0.5$ MeV. Right panel shows the results of PVCVM at $T = 0$ and 3 MeV. (Adapted from refs. [80] and [85].)

and

$$F = \int R_0 \frac{\partial U}{\partial r} R_0 \frac{\partial \rho}{\partial r} r^2 dr, \quad (34)$$

where U is the mean-field potential. The results of calculations, within the PVCVM, for ^{90}Zr (fig. 4(b)) and ^{208}Pb show that the GDR energy is not sensitive to the change of T and the GDR width becomes even smaller at $T = 3$ MeV compared to that at $T = 0$.

Summarising the results obtained within the QPM and PVCVM, one concludes that the straightforward extension of these microscopic models to finite temperatures does not lead to a significant increase in the GDR spreading width Γ^\downarrow . Hence, other mechanisms are called for in order to describe the experimentally observed increase in the GDR width.

3.5 Phonon damping model

3.5.1 Non-rotating closed-shell nuclei

The phonon damping model (PDM) was first proposed [86, 87] to describe the GDR damping in closed-shell nuclei. Within this model, the GDR width arises due to the coupling of the structureless GDR phonon to non-collective ph , pp and hh configurations. The PDM Hamiltonian is written as

$$H = \sum_s (\epsilon_s - \lambda) a_s^\dagger a_s + \sum_q \omega_q Q_q^\dagger Q_q + \sum_{ss'q} F_{ss'}^{(q)} a_s^\dagger a_{s'} (Q_q^\dagger + Q_q), \quad (35)$$

where the three terms, respectively, describe the single-particle field, the phonon field and the coupling between them. Q_q^\dagger and Q_q are the creation and destruction operators of a phonon with energy ω_q . The indices s and s' denote particle ($s = p$, $\epsilon_s - \lambda > 0$) or hole ($s = h$, $\epsilon_s - \lambda < 0$). The index $q = \{L, i\}$ represents the i -th

phonon state of multipolarity L (the projection M of L in the phonon index is omitted for simplicity).

The propagator of the GDR phonon, which is damped due to coupling to the quasiparticle field, is

$$G_q(E) = \frac{1}{2\pi} \frac{1}{E - \omega_q - P_q(E)}, \quad (36)$$

where the polarization operator $P_q(E)$ appears because of the coupling between ph pairs and phonons in the last term of the right-hand side of the Hamiltonian (eq. (6)). It has the form

$$P_q(E) = \sum_{ss'} [F_{ss'}^{(q)}]^2 \frac{f_s - f_{s'}}{E - \epsilon_{s'} + \epsilon_s}, \quad (37)$$

where f_s is the single-particle occupation number given by

$$f_s = 1 / \{ \exp[(\epsilon_s - \lambda)/T] - 1 \}. \quad (38)$$

The energy $\bar{\omega}$ of the giant resonance (damped collective phonon) is found as a solution of the equation $\bar{\omega} - \omega_q - P_q(\bar{\omega}) = 0$, where $q = 1$ corresponds to the GDR with $E_D \equiv \bar{\omega}$.

The phonon damping $\gamma_q(\omega)$ is calculated as the imaginary part of the analytic continuation of $P_q(E)$ into the complex energy plane, *viz.*,

$$\begin{aligned} \gamma_q(\omega) &= \text{Im}[P_q(\omega \pm i\varepsilon)] \\ &= \pi \sum_{ss'} [F_{ss'}^{(q)}]^2 (f_{s'} - f_s) \delta(\omega - \epsilon_s + \epsilon_{s'}). \end{aligned} \quad (39)$$

The GDR width is given as $\Gamma_D = 2\gamma E_D$ and is conveniently decomposed into the quantal (Γ_Q) and thermal (Γ_T) widths as $\Gamma_D = \Gamma_Q + \Gamma_T$, where

$$\Gamma_Q = 2\pi \sum_{ph} [F_{ph}^{(1)}]^2 (f_h - f_p) \delta(E_D - \epsilon_p + \epsilon_h) \quad (40)$$

and

$$\begin{aligned} \Gamma_T &= 2 \left\{ \sum_{p>p'} [F_{pp'}^{(1)}]^2 (f_{p'} - f_p) \delta(E_D - \epsilon_p + \epsilon_{p'}) \right. \\ &\quad \left. + \sum_{h>h'} [F_{hh'}^{(1)}]^2 (f_{h'} - f_h) \delta(E_D - \epsilon_h + \epsilon_{h'}) \right\}. \end{aligned} \quad (41)$$

The quantal width Γ_Q does not vanish even at $T = 0$ since in this case $f_h = 1$ and $f_p = 0$. It is responsible for the spreading width of the GDR built on the ground state. The thermal width Γ_T vanishes at $T = 0$. At $T \neq 0$, a non-zero Γ_T arises due to the coupling to pp and hh configurations. These configurations appear because of the distortion of the Fermi surface at finite T which leads to finite differences $f_{p'} - f_p$ and $f_{h'} - f_h$. As T increases, the difference $f_h - f_p$ decreases resulting in a slight decrease in the quantal width Γ_Q . The same feature was also obtained within the PVCMM in sect. 3.4. On the other hand, the differences $f_{p'} - f_p$ and $f_{h'} - f_h$ increase sharply with

T up to a moderate T , reach a plateau at higher T and decrease as T increases further. This leads to a total width which increases up to $T \sim 3$ MeV and reaches a plateau at $T \sim 3-4$ MeV in medium-mass and heavy nuclei. The PDM thus describes the increase in the GDR width at low and moderate T and its saturation at high T [86, 87].

A version of the PDM, which explicitly involves the coupling to two-phonon configurations in the second order of the interaction vertex, was proposed in refs. [88–90]. Here, higher-order Green functions were included in deriving the equation for the propagator (eq. (36)). It was shown that the mechanism for generating the quantal width Γ_Q within the PDM is similar to that of the spreading width in the PVCMM discussed in sect. 3.4. However, it can be seen from the polarization operator that the width increase at finite T within the PDM is driven by the differences $f_{p'} - f_p$ and $f_{h'} - f_h$ of the single-particle occupation numbers in the thermal width Γ_T .

The line shape of the GDR is described by the strength function $S_D(\omega)$, which is derived from the spectral intensity in the standard way using the analytic continuation of the Green function (eq. (36)) and by expanding the polarization operator (eq. (37)) around $\omega = E_D$. The final form of $S_D(\omega)$ is [87]

$$S_D(\omega) = \frac{1}{\pi} \frac{\gamma_1(\omega)}{(\omega - E_D)^2 + \gamma_1^2(\omega)}. \quad (42)$$

3.5.2 Inclusion of thermal pairing

In open-shell nuclei, the PDM Hamiltonian in the quasiparticle representation consists of three terms, describing the quasiparticle mean field, the phonon field and the interaction between them. The GDR quantal and thermal widths including pairing are given as

$$\Gamma_Q = 2\pi \sum_{ph} [F_{ph}^{(1)}]^2 [u_{ph}^{(+)}]^2 (1 - n_p - n_h) \delta(E_D - E_p - E_h), \quad (43)$$

$$\Gamma_T = 2\pi \sum_{s>s'} [F_{ss'}^{(1)}]^2 [v_{ss'}^{(-)}]^2 (n_{s'} - n_s) \delta(E_D - E_s + E_{s'}), \quad (44)$$

with

$$ss' = pp', hh',$$

where the quasiparticle occupation numbers n_k and the quasiparticle energies E_k are defined in eq. (13) and $u_{kk'}^{(+)}$ and $v_{kk'}^{(-)}$ are given in eq. (15).

The increase in the total width at low T is compensated by the T -dependence of the thermal pairing. Because of the thermal fluctuations in finite nuclei, the pairing gap does not collapse at the critical temperature of the superfluid-to-normal phase transition but decreases monotonically with increasing T as has been discussed in sect. 3.2. This turns the smooth Fermi surface due to pairing at $T = 0$ to the Heaviside step-function distribution, thus, reducing the effect of coupling to pp and hh

configurations. Depending on the pairing force, in different open-shell nuclei, this compensation at low T causes the GDR width to remain insensitive to T or may even decrease at $T \leq 1$ MeV. At $T > 1$ MeV, the effect of thermal pairing becomes small and the GDR width starts to increase because of the increase in Γ_T [91]. The effect of pairing on the GDR width at low T is model-independent and holds also in other models such as the TSFM as discussed later.

3.5.3 Inclusion of angular momentum

The PDM has been extended to include the effect of angular momentum at finite T in ref. [92]. To describe the NC rotation of a spherical nucleus, the z -projection M of the total angular momentum J is added to the PDM Hamiltonian (eq. (35)) as $-\gamma\hat{M}$, where γ is the Lagrange multiplier, which is sometimes interpreted as the angular velocity or rotation frequency in analogy to classical rotation. This rotation frequency γ and the chemical potential λ are defined from the equations for total angular momentum M (equal to J for spherical nuclei) and particle number, respectively. The phonon damping $\gamma_q(\omega)$ becomes [92]

$$\gamma_q(\omega) = \varepsilon \sum_{k>k'} [\mathcal{F}_{kk'}^{(q)}]^2 \left[\frac{f_{k'}^+ - f_k^+}{(\omega - E_k^- + E_{k'}^-)^2 + \varepsilon^2} + \frac{f_{k'}^- - f_k^-}{(\omega - E_k^+ + E_{k'}^+)^2 + \varepsilon^2} \right], \quad (45)$$

where

$$f_k^\pm = \frac{1}{e^{\beta(\epsilon_k - \lambda \mp \gamma m_k)} + 1}.$$

An extension of the PDM including both pairing and angular momentum is impractical because the GDR width is insensitive to a moderate change in angular momentum (for example, up to $\sim 30\hbar$ in ^{120}Sn). However, at large values of angular momentum, the effect of thermal pairing either vanishes or becomes negligible.

3.5.4 Selection of parameters and ingredients of numerical calculations

Numerical calculations within the PDM adopt the single-particle energies obtained from the Woods-Saxon potential at $T = 0$. Except for the neutron and proton Fermi levels (chemical potentials $\lambda_{N,Z}$), which change with T to conserve the average neutron and proton numbers, respectively, the single-particle energies are kept unchanged with T , based on the results of refs. [93, 94]. The matrix elements for the coupling of the GDR to ph configurations, which cause the quantal width Γ_Q (eq. (40)), are all set equal to F_1 . Those for the coupling of the GDR to pp and hh configurations, which cause the thermal width Γ_T (eq. (41)), are all set equal to F_2 . This assumption of a constant coupling strength is well justified in the so-called

weak coupling limit [1, 68] when the width of a collective mode is much smaller than the energy range ΔE (of the order of E_D) over which this mode is coupled to the background states (see ref. [1], Vol. I, appendix 2D-3). Based on the results in sects. 3.3 and 3.4, which show the insensitivity of the quantal width Γ_Q to the change of T , it is assumed that the microscopic mechanism of the spreading width Γ_Q at $T = 0$ is known from the QPM and/or the PVCMM. Therefore, for the calculations of the GDR width and strength function at zero angular momentum, the unperturbed phonon energy ω_q and the parameter F_1 are chosen so that after the ph -GDR coupling is switched on, the calculated GDR energy E_D and the quantal width Γ_Q reproduce the corresponding experimental values for the GDR in the ground state ($T = 0$). The parameter F_2 is fixed at $T = 0$ so that E_D does not change much with T (see sect. II B of ref. [91] for a detailed discussion). For the calculations in hot and rotating nuclei, the latter criterion is hard to be fulfilled. Therefore, F_2 is chosen to reproduce one data point for the width at a given J and T , whereas the GDR energy E_D is fixed at the experimental value.

The analysis of the numerical results carried out within the PDM for ^{88}Mo in refs. [92, 95] shows that the GDR width increases with J for $T \leq 3$ MeV and saturates at $T \simeq 3.5$ MeV for $J \geq 50$. At higher J (≥ 70) the width saturates at any value of T .

3.6 Collisional damping model

We now discuss various macroscopic approaches to the GDR damping encompassing various models, the first one being the collisional damping model (CDM) [96–99]. The CDM follows the ideology of the microscopic approaches in the study of the isovector volume vibrations in spin-isospin symmetric (or asymmetric) nuclear matter at finite temperatures. In this model, the inter-particle collision is responsible for the damping of the isovector vibration, which includes the parts corresponding to Landau, spreading and escape widths in microscopic theories. The isovector response of a uniform nuclear matter is described by the linearised two-component Landau-Vlasov equation [8–10] that includes an inter-particle collision term as

$$\frac{\partial \delta f}{\partial t} + \frac{\mathbf{p}}{m} \cdot \nabla_r \delta f - \nabla_r U_0 \cdot \nabla_p \delta f - \nabla_r \delta U \cdot \nabla_p f_0 = J(\delta f), \quad (46)$$

where $\delta f \equiv \delta f_\pi - \delta f_\nu$ with π and ν denoting protons and neutrons, respectively. The variation δU is the Wigner transform of that of the self-consistent potential with respect to the equilibrium value U_0 . The parameters of the potential are adjusted to reproduce the nuclear matter incompressibility modulus K . The unperturbed distribution f_0 is the Fermi-Dirac distribution similar to that given in eq. (38). The right-hand side of eq. (46) is the collision term $J(\delta f_i)$, which represents the change of the distribution function because of the relaxation. No dependence on angular momentum is considered in this approach.

Assuming independent dissipation rates, the collision term is decomposed into $J_{wall}(\delta f_i)$ owing to the one-body

wall dissipation [100], the collision integral $J_{coll}(\delta f_i)$ for the two-body collisions, and $J_{\uparrow}(\delta f_i)$ arising from the emission of particles to the continuum. In the relaxation time approximation, it has the following form

$$J(\delta f_i) = J_{wall}(\delta f_i) + J_{coll}(\delta f_i) + J_{\uparrow}(\delta f_i) \\ = -\frac{(\delta f_i)_{L \geq 2}}{\tau_{wall}} - \frac{(\delta f_i)_{L=1}}{\tau_{coll}} - \frac{(\delta f_i)_{L \geq 2}}{\tau_{\uparrow}}. \quad (47)$$

The constraints on multiplicities L comes from the fact that the one-body term $J_{wall}(\delta f_i)$ does not contain the components with $L = 0$ and 1 for the distorted distribution function δf_i in the momentum space because of the conservation of particle number and total momentum. The same holds for $J_{\uparrow}(\delta f_i)$ assuming that the change of the average particle and current densities in the nuclear interior owing to particle emission is negligible up to $T = 4\text{--}5$ MeV. As for the two-body collision integral $J_{coll}(\delta f_i)$, the component $L = 1$ corresponds to the oscillation of protons against neutrons in the phase space of the GDR, conserving the particle-number and momentum distributions. The relaxation time τ_{coll} is a function of the frequency ω_0 of the collective vibration and temperature. The dependence of τ_{coll} on ω_0 arises from the memory (retardation) effects in correspondence to the Landau description [101]. These three components $J_{wall}(\delta f_i)$, $J_{coll}(\delta f_i)$, and $J_{\uparrow}(\delta f_i)$ are related to the Landau width Γ^{LD} , the spreading width Γ^{\downarrow} , and the escape width Γ^{\uparrow} , respectively. In the long-relaxation time regime ($\omega_0\tau \gg 1$) [10], the GDR width is given by eq. (3) with

$$\Gamma^{LD} = \frac{2}{\tau_{wall}}, \quad \Gamma^{\downarrow} = \frac{2}{\tau_{coll}}, \quad \Gamma^{\uparrow} = \frac{2}{\tau_{\uparrow}}. \quad (48)$$

The propagation of sound wave in an infinite Fermi liquid in the same condition is different from that in finite nuclei by the absence of the one-body wall dissipation and particle emission [101, 102].

The relaxation times τ_{wall} , τ_{coll} , and τ_{\uparrow} are estimated as

$$\tau_{wall} = \frac{8R\xi^{(L)}}{3v_F[1 + (\pi^2/6)(T/\epsilon_F)^2]}, \\ \tau_{coll} = \frac{\alpha}{T^2 + (\omega_0/2\pi)^2}, \\ \tau_{\uparrow} = \frac{\pi}{mR^2T^2}e^{B_n/T}, \quad (49)$$

where $v_F = p_F/m^*$ is the Fermi velocity, R is the nuclear radius, and B_n is the neutron binding energy.

In the numerical calculations, the CDM adopts the parameter $\xi^{(L)} = 10/L$, which is obtained by using, for Γ_{CDM}^{LD} , the Landau width predicted by a simplified version of the RPA at zero temperature [103–105]. Hence, one has $\xi^{(1)} = 10$ for the GDR. The parameter α is calculated from the in-medium cross-sections for NN scattering with relative energies close to the Fermi energy. Adopting the free space (vacuum) NN cross-sections $\sigma_{pp} = \sigma_{nn} = 2.5 \text{ fm}^2$, $\sigma_{pn} = \sigma_{np} = 5.0 \text{ fm}^2$, and nuclear matter density

$\rho_0 = 0.18 \text{ fm}^{-3}$, the authors of ref. [99] found the values $\alpha = 2.3 \text{ MeV}$ and 5.4 MeV by using the free-space (vacuum) and the in-medium NN cross-sections, respectively. The relaxation time τ_{\uparrow} is neglected in the numerical calculations within the CDM because of its small value up to $T \sim 4 \text{ MeV}$.

3.7 Fermi liquid-drop model

The FLDM is based on the same linearised Landau-Vlasov eq. (46), but instead of the assumption in eq. (47), the collision term on the right-hand side includes only a memory-dependent two-body integral $J_{coll}(\delta f_i)$ to describe the dissipative behaviour that leads to the spreading width Γ^{\downarrow} of the giant multipole resonance [106, 107]. In this respect, the FLDM is the macroscopic correspondence to the QPM and the PVCN discussed in sects. 3.3 and 3.4. As with the CDM, only giant multipole resonances in non-rotating nuclei (zero angular momentum) are considered within the FLDM.

The collision term is taken in the general form as

$$J_{coll}(\delta f_i) = \int_{-\infty}^t A(t-t')\delta f(t')dt', \quad (50)$$

which accounts for the retardation effects included in $A(t-t')$ in the lowest order of the deviation of the correlation function from its equilibrium value. Assuming a periodic oscillation $\delta f \sim \exp(-i\omega t)$, the FLDM considers the high-frequency oscillations in Fermi liquids as phonons, which are created and absorbed when quasiparticles collide.

The width Γ^{\downarrow} of the collective vibration is obtained within the FLDM as [106]

$$\Gamma^{\downarrow} = 2q \frac{\omega_0^2 \tau_{coll}}{1 + q(\omega_0 \tau_{coll})^2}, \quad q \simeq \frac{1}{2}(1 + F_0) \left(1 + \frac{1}{3}F_1\right), \quad (51)$$

with the Landau parameters F_0 and F_1 [10]. The relaxation time τ_{coll} is given as

$$\tau_{coll} = \frac{\tilde{\tau}}{1 + \zeta(\omega_0/2\pi T)^2}, \quad \tilde{\tau} = \frac{12\pi^2}{m^3 \bar{w} T^2}, \quad (52)$$

where \bar{w} denotes the average of the scattering amplitudes, over angles, of the relative momentum of the colliding particles near the Fermi surface (the collision probability). Assuming $\zeta = 1$ (the Landau value) [10, 101], and parameterising the thermal relaxation time $\tilde{\tau}$ as

$$\tilde{\tau} = \frac{\alpha}{T^2}, \quad (53)$$

one recovers from eq. (52) the relaxation time τ_{coll} in eq. (49) adopted in the CDM. It is then clear that the spreading width Γ^{\downarrow} obtained within the CDM (48) is a special case of that predicted by the FLDM in eq. (51). The former is valid for the width in the long-relaxation time regime of the latter, *i.e.*, when $\omega_0 \tau_{coll} \gg q^{-1/2}$ in eq. (51). The condition $\omega_0 \tau \gg 1$ of the long-relaxation

time is equivalent to the long mean free path of quasiparticles as compared to the wave length (the zero-sound or rare-collision regime). The other short-relaxation time limit $\omega_0\tau \ll 1$ is equivalent to the condition of short mean free path of quasiparticles meaning that the mean free path of nucleons is smaller than the nuclear radius (the first-sound or frequent-collision regime [10]).

The width Γ^\downarrow given by eq. (51) describes both the regimes of short-relaxation time ($\omega_0\tau \ll 1$ or $T \gg \omega_0$) and long-relaxation time ($\omega_0\tau \gg 1$ or $T \ll \omega_0$) as well as the smooth transition between them. This width goes to zero with $\omega_0\tau$, whereas the width Γ^\downarrow in eq. (48) increases as $\omega_0\tau$ decreases.

As has been mentioned previously, the FLDM predicts only the spreading width or the collisional width, but not the FWHM of the GDR because the width Γ^\downarrow in eq. (51) does not include the Landau width Γ^{LD} owing to the effect of one-body dissipation (long mean free path), which is important in the zero-sound regime. It does not include the escape width Γ^\uparrow either as its contribution to the total width is negligible and, hence, is not included in most models. In some models, it is included by means of smoothing parameters converting the discrete GDR strength function to a continuous line shape.

3.8 Thermal shape fluctuation model

3.8.1 Adiabatic coupling model

The adiabatic coupling model (ACM) [108, 109] assumes that the time scale for thermal fluctuations is larger than the time for the dipole vibration to adjust to the changed shape. Therefore, the GDR strength function can be averaged over all possible quadrupole shapes with deformation $\alpha_{2\mu}$ and orientations [109]. The angular momentum projected GDR cross-section $\sigma(\omega)$ at a given T is calculated within the ACM as a thermal average over the shape-dependent cross-sections $\sigma(\omega, \alpha_{2\mu}, \omega_J)$ as

$$\sigma(\omega) = \frac{1}{Z_J} \int \frac{\mathcal{D}[\alpha]}{\mathcal{I}(\beta, \gamma, \theta, \psi)^{3/2}} \times \sigma(\omega, \alpha_{2\mu}, \omega_J) \exp[-F(T, \alpha_{2\mu}, J)/T], \quad (54)$$

where ω is the photon energy and $\sigma(\omega, \alpha_{2\mu}, \omega_J)$ is calculated at the saddle-point frequency

$$\omega_J = (J + 1/2)/\mathcal{I}(\beta, \gamma, \theta, \psi).$$

The volume element $\mathcal{D}[\alpha]$ is

$$\mathcal{D}[\alpha] = \beta^4 \sin(3\gamma) d\beta d\gamma d\Omega. \quad (55)$$

The partition function Z_J is calculated as

$$Z_J = \int \mathcal{D}[\alpha] \mathcal{I}^{-3/2} \exp[-F(T, \alpha_{2\mu}, J)/T]. \quad (56)$$

For the free energy, the ACM employs an expansion based on the Landau theory of phase transition around the saddle point at a constant J [110, 111] as

$$F(T, \alpha_{2\mu}, J) \equiv F(T, \beta, \gamma, J) = F(T, \beta, \gamma, 0) + (J + 1/2)^2 / [2\mathcal{I}(\beta, \gamma, \theta, \psi)], \quad (57)$$

where

$$\mathcal{I}(\beta, \gamma, \theta, \psi) \equiv \hat{\omega} \cdot \mathbf{I} \cdot \hat{\omega} = I_1 \cos^2 \psi \sin^2 \theta + I_2 \sin^2 \psi \sin^2 \theta + I_3 \cos^2 \theta \quad (58)$$

is the moment of inertia about the rotation axis, expressed in terms of the principal moments of inertia I_k , and the Euler angles $\Omega = (\psi, \theta, \phi)$. $F(T, \beta, \gamma, 0)$ denotes the cranking free energy at $\omega_J = 0$.

The free energy $F(T, \beta, \gamma, 0)$ and the principal moments of inertia are calculated using either the liquid-drop model (LDM), the Nilsson-Strutinsky approach including shell corrections or the Landau parameterisation [110, 111]. The last one attempts to combine both the LDM free energy and the shell corrections into one expansion, but this parameterisation is not adequate because it deviates from the results of Nilsson-Strutinsky calculations at larger deformations.

In the Nilsson-Strutinsky method, the free energy F is presented as the sum of the LDM free energy F_{LDM} and the shell correction F_{SHL} , *viz.*,

$$F = F_{LDM} + F_{SHL}. \quad (59)$$

The ACM approximates F_{SHL} by the parameterisation

$$F_{SHL}(\beta, \gamma, T) = \sum_{l=0}^{even} A_l j_l(B_l \beta) C_l T / \sinh(C_l T) + \sum_{l=3}^{odd} A_l j_l(B_l \beta) \cos(3\gamma) C_l T / \sinh(C_l T), \quad (60)$$

j_l being the spherical Bessel functions. The parameters A_l , B_l and C_l are found by fitting the results of the Nilsson-Strutinsky calculations for oblate, prolate, and triaxial shapes for $\beta \leq 1.0$ and $T = 0.25$ –3 MeV.

The shell correction to the moment of inertia is also parameterised as

$$I_3^{SHL}(\beta, \gamma, T) = \sum_{l=0}^{even} A_l^I j_l(B_l^I \beta) C_l^I T / \sinh(C_l^I T) + \sum_{l=3}^{odd} A_l^I j_l(B_l^I \beta) \cos(3\gamma) C_l^I T / \sinh(C_l^I T) + \sum_{l \geq 1} \alpha_l j_l(k_l \beta) \cos(\gamma + 2\pi/3) \eta_l T / \sinh(C_l T), \quad (61)$$

$$I_1^{SHL}(T, \beta, \gamma) = I_3^{SHL}(T, \beta, \gamma + 2\pi/3), \\ I_2^{SHL}(\gamma) = I_3^{SHL}(T, \beta, \gamma - 2\pi/3),$$

with the parameters A_l^I , B_l^I , C_l^I , α_l , k_l , and η_l determined in a similar way as for the free energy (eq. (60)).

Pairing is neglected in the original version of the ACM [109] on the ground that it vanishes at $T = T_c$ within the FT-BCS theory according to eqs. (16) and (17). The GDR frequency is calculated as that of a rotating deformed harmonic oscillator having three fundamental modes with energies given by eq. (4) with $E_{D0} = 80A^{-1/3}$ MeV.

The GDR Hamiltonian in the intrinsic frame is written as

$$H_{GDR} = \sum_k (p_k^2 + E_k^2 d_k^2) + \boldsymbol{\omega}_{rot}(\mathbf{d} \times \mathbf{p}), \quad (62)$$

where d_k and p_k are the coordinates and conjugate momenta of the GDR vibration, and $\boldsymbol{\omega}_{rot}$ is the rotation frequency. The GDR cross-section in the intrinsic frame is calculated by using the Breit-Wigner distribution as

$$\begin{aligned} \sigma(\omega, \alpha_{2\mu}, \omega_J) &= \frac{8\pi^2 e^2 \hbar NZ}{3mc} \frac{1}{A} \sum_{\mu\nu} |\langle \nu | d_\mu | 0 \rangle|^2 \omega \\ &\times [f^{BW}(\omega, E_\nu, \Gamma_\nu) - f^{BW}(\omega, -E_\nu, \Gamma_\nu)] \\ &= \sigma_0 \sum_{\mu\nu} |\langle \nu | d_\mu | 0 \rangle|^2 E_\nu f^L(\omega, E'_\nu, \Gamma_\nu), \end{aligned} \quad (63)$$

where μ denotes the spherical components of the dipole mode and $|\nu\rangle$ are the eigenstates of the model Hamiltonian. The parameterised intrinsic widths of the three components, centered at E_ν , are given by eq. (5) where E_{D0} and Γ_{D0} are defined earlier. The value of δ , as mentioned earlier, is typically 1.8. The Breit-Wigner distribution $f^{BW}(\omega, E_D, \Gamma)$ has the form

$$f^{BW}(\omega, E_D, \Gamma) = \frac{1}{\pi} \frac{\Gamma/2}{[(\omega - E_D)^2 + (\Gamma/2)^2]}, \quad (64)$$

whereas $f^L(\omega, E'_\nu, \Gamma_\nu)$ is the Lorentzian distribution

$$\begin{aligned} f^L(\omega, E'_\nu, \Gamma_\nu) &= \frac{\omega}{E_\nu} [f^{BW}(\omega, E_\nu, \Gamma_\nu) - f^{BW}(\omega, -E_\nu, \Gamma_\nu)] \\ &= \frac{2}{\pi} \frac{\omega^2 \Gamma_\nu}{[\omega^2 - (E'_\nu)^2]^2 + \omega^2 \Gamma_\nu^2}, \end{aligned} \quad (65)$$

with $(E'_\nu)^2 = E_\nu^2 + (\Gamma_\nu/2)^2$. The normalisation factor σ_0 on eq. (63) ensures the integrated cross-section of the GDR to be equal to TRK .

In some recent TSFM calculations, the liquid-drop part of the potential energy surface (PES) is calculated within the Lublin-Strasbourg-Drop (LSD) model [112–114]. The model can explain the experimental nuclear masses over a wide range and the fission barriers in heavy nuclei. The entropy and the free energy are calculated within a five-dimensional deformation space. The chemical potentials and the grand partition function are calculated using the single-particle energies obtained from the deformed Woods-Saxon potentials with an optimised parameterisation of the spin-orbit part [115, 116]. The GDR is generated by the Hamiltonian of the cranking harmonic oscillator [114] and the GDR cross-sections are given by the Lorentzian functions in eq. (1) with the width Γ_ν evaluated by eq. (5) using $\delta = 1.9$. The rotation leads to a Coriolis splitting of the two GDR frequencies for the oscillation perpendicular to the rotation axis and the GDR strength function consists, in general, of five components.

3.8.2 Fitting formula for the liquid-drop GDR width

In ref. [117] a phenomenological fit for the GDR width, calculated within the TSFM for many nuclei in the liquid-drop limit, was obtained. This fit, sometimes referred to

as the phenomenological TSFM (pTSFM), expresses the GDR width as a function of T , A and J as

$$\begin{aligned} \Gamma_D(T, J, A) &= \Gamma_D(T, J = 0, A) \left[L\left(\frac{J}{A^{5/6}}\right) \right]^{4/[T/T_0+3]}, \\ \Gamma_D(T, J = 0, A) &= \Gamma_0(A) + c(A) \ln\left(1 + \frac{T}{T_0}\right). \end{aligned} \quad (66)$$

The reference temperature $T_0 = 1 \text{ MeV}$ is used in the pTSFM calculations. The experimental ground-state GDR width is adopted for $\Gamma_0(A)$. The scaling functions $L(x)$ and the prefactor $c(A)$ are fitted as

$$L(x) \simeq 1 + \frac{1.8}{1 + e^{(1.3-x)/0.2}}, \quad c(A) = 6.45 - A/100. \quad (67)$$

The scaling law (eq. (66)) was examined in ref. [118] using the experimental GDR widths from the extensive compilation in ref. [20]. A large scatter of experimental widths (up to 40%) implied that the parameterisation is not universal and not independent of mass.

3.8.3 Inclusion of pairing-field fluctuation in TSFM

In some recent work, the TSFM was extended to include the fluctuations in the pairing field [119, 120]. The nuclear shapes were related to the GDR observables using a model Hamiltonian, which describes the motion of nucleons within an anisotropic harmonic oscillator potential with the residual separable dipole-dipole and monopole pairing interactions, as

$$H = H_{osc} + \eta D^\dagger D - G P^\dagger P, \quad (68)$$

where H_{osc} stands for the anisotropic harmonic oscillator Hamiltonian. The parameter η characterises the isovector component of the neutron and proton average field and G denotes the strength of the pairing interaction. The oscillator frequencies ω_ν^{osc} ($\nu = x, y, z$) change to $\omega_\nu = \omega_\nu^{osc} - \chi \omega^P$, with $\omega^P = [(Z\Delta_Z + N\Delta_N)/(Z+N)]^2$ under the pairing interaction, which also renormalises the dipole-dipole interaction strength to $\eta = \eta_0 - \chi_0 \sqrt{T} \omega^P$ with Z and N denoting proton and neutron systems, respectively.

The GDR cross-section is given as a sum of Lorentzians (eq. (1)). The widths of the components were obtained using eq. (5) with $\Gamma_0 = (0.026 \pm 0.005) E_0^\delta$ [45]. The peak cross-sections of the components were fixed by the sum rule (eq. (2)) with $\alpha = 0.3$ for all nuclei. The other parameters η_0 (or η) and χ_0 (or χ) were adjusted to reproduce the experimental width of the GS-GDR.

The averaged GDR cross-section was calculated using eqs. (1), (4), (5) and (54), with the metric $\mathcal{D}[\beta, \theta, \gamma, \Delta]$. The latter is defined by combining the metrics in eqs. (18) and (54) as [119–121]

$$\mathcal{D}[\beta, \theta, \gamma, \Delta] = \beta^4 d\beta \sin \theta d\theta |\sin 3\gamma| d\gamma \Delta d\Delta, \quad (69)$$

where $d\Omega \equiv d\phi d\psi$ is omitted because the orientation fluctuations are negligible [121].

The total free energy (F_{TOT}) at a fixed deformation was calculated by using the finite temperature Nilsson-Strutinsky method as

$$F_{TOT} = E_{LDM} + \sum_{\tau=\pi,\nu} \delta F_{\tau}, \quad (70)$$

where the liquid-drop energy E_{LDM} was obtained by summing up the Coulomb and surface energies corresponding to a triaxially-deformed shape with deformation parameters β and γ . The shell correction $\delta F_{\tau} \equiv F_{\tau} - \tilde{F}_{\tau}$ was calculated by using the proton (π) and neutron (ν) single-particle energies obtained in the triaxial Nilsson potentials. With the pairing fluctuations, the corresponding free energy was determined in the GCE as

$$\begin{aligned} F &= \langle H_0 \rangle - \lambda N - TS \\ &= \sum_i (\epsilon_i - \lambda - E_i) - 2T \sum_i \ln[1 + \exp(-E_i/T)] + \frac{\Delta^2}{G}, \end{aligned} \quad (71)$$

where H_0 is the nuclear Hamiltonian, λ is the chemical potential, N is the particle number, S is the entropy, and ϵ_i are the single-particle energies obtained by diagonalising H_0 within a harmonic oscillator basis comprising the first 12 major shells. The quasiparticle energies E_i and the pairing gap Δ were obtained from the FT-BCS eqs. (16) and (17) by assuming a constant pairing strength $G_{\pi,\nu} = [19.2 \pm 7.4(N - Z)]/A^2$. The smoothed free energy was found by Strutinsky's method. The total entropy is given as $S = \sum_i s_i = -2 \sum_i [n_i \ln n_i + (1 - n_i) \ln(1 - n_i)]$, with the quasiparticle occupation numbers n_i following the Fermi-Dirac distribution (eq. (13)). The calculations without pairing ($\Delta = 0$) considered the CE, where the expression for free energy reduces to that given in refs. [122, 123].

3.8.4 On the consistency of TSFM

In a theoretical work [124], an inconsistency in various TSFM calculations was pointed out. In these calculations, the GDR strength function is computed by using a deformed harmonic oscillator model whereas the free energy F is calculated within the Nilsson-Strutinsky approach (eq. (70)). Hence, the same Hamiltonian is not employed consistently. In order to address this issue, calculations were performed using a model Hamiltonian with an effective quadrupole-quadrupole interaction, *viz.*,

$$H = H_0 - \frac{1}{2} \chi_Q \sum_{\mu} (-1)^{\mu} \hat{Q}_{\mu} \hat{Q}_{\mu}, \quad (72)$$

where H_0 stands for the spherical part and $\hat{Q}_{\mu} = (r^2/b^2)Y_{2\mu}$ is the quadrupole operator with the harmonic-oscillator length $b = \sqrt{\hbar/(m\omega_0)}$, and $\omega_0 = 41A^{-1/3}$ MeV. The parameter $\chi_Q = 120A^{-5/3}f_c$ MeV includes the core polarization factor $f_c \geq 1$ owing to an inert core. This

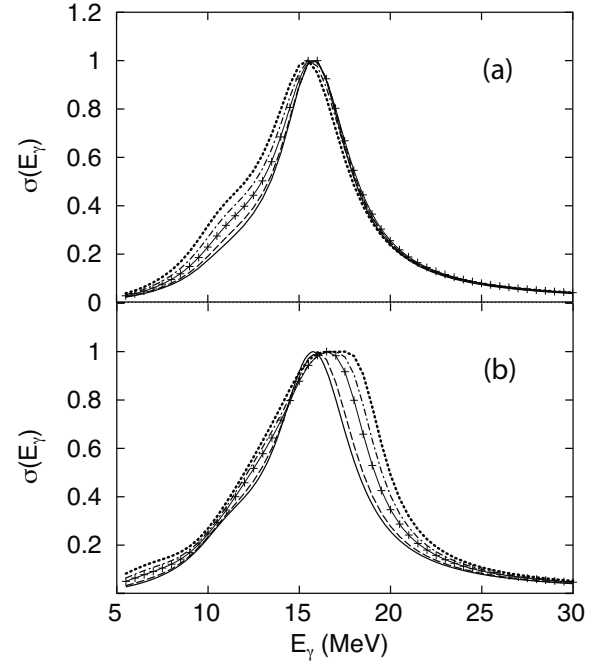


Fig. 5. (a) GDR photoabsorption cross-section in ^{120}Sn at $J = 0$. Solid, dashed, cross-solid, dash-dotted, and dotted curves correspond to $T = 0.5, 1, 2, 3,$ and 4 MeV, respectively. (b) Same as in (a) but at $T = 0$ and $J = 0, 26, 55, 69,$ and 83 , respectively. (Adapted from ref. [124].)

Hamiltonian corresponds to a (β, γ) -dependent one-body mean-field Hamiltonian of the Nilsson type. Therefore, the spherical single-particle energies were calculated using the spherical Nilsson potential with A -dependent Nilsson parameters. The GDR cross-section was calculated within the SPA as

$$\begin{aligned} \sigma(E_{\gamma}, \omega, T) &= \\ &= \frac{\int e^{(\omega_0\beta)^2/(2\chi_Q T)} z(\beta, \gamma, \omega) \sigma(E_{\gamma}, \beta, \gamma, \omega, T) d\mathcal{D}[\beta, \gamma]}{\int e^{(\omega_0\beta)^2/(2\chi_Q T)} z(\beta, \gamma, \omega) d\mathcal{D}[\beta, \gamma]}, \end{aligned} \quad (73)$$

with [125]

$$z(\beta, \gamma, \omega) = \text{Tr} \exp[-(\hat{H}' - \omega \hat{J}_x - \lambda_{\pi} Z - \lambda_{\nu} N)/T], \quad (74)$$

$$\hat{H}' = \sum_i \hat{h}_i,$$

$$\hat{h}(\beta, \gamma) = h_0 - \omega_0 \beta \frac{r^2}{b^2} \left[\cos \gamma Y_{20} + \frac{1}{\sqrt{2}} \sin \gamma (Y_{22} + Y_{2-2}) \right], \quad (75)$$

and $d\mathcal{D}[\beta, \gamma]$ defined in eq. (55).

The results of the calculations for the GDR cross-section in ^{120}Sn (fig. 5) show a weak increase in the GDR width with T and J . Angular momentum has a somewhat stronger effect yielding an increase of $\sim 22\%$ at $J = 69$

compared to the value at $J = 0$ (at $T = 2$ MeV). The conclusion drawn from this work was that the TSFM calculations, done consistently, do not lead to a sufficient increase in the (T, J) -dependent GDR width as observed experimentally.

4 Experimental observations and comparison with theory

Following the first observation of the GDR built on excited states in heavy-ion fusion reactions [6], this phenomenon was observed in deep inelastic reaction products [126] in the $^{136}\text{Xe} + ^{181}\text{Ta}$ reaction. An analysis of the high-energy γ -ray spectra for various E_X revealed, for the first time, that the GDR width increases with E_X . The authors also suggested a decrease in the GDR energy with the increase in E_X . Many experiments over the years have refuted the second observation and the GDR centroid energy is now considered to be a stable quantity in a particular nucleus being independent of E_X and J . The inferred GDR strength corresponds to $\sim 100\%$ of TRK except at very high E_X . The increase of GDR width with E_X and/or J , however, has been a universal observation in all later studies.

In very early years, a few experiments were performed in coincidence with M_γ and tagging with high-spin isomers [127, 128] to characterise the evolution of the width. A few other experiments established that the GDR γ -rays are emitted from an equilibrated CN by 1) the measurements of GDR γ -rays from the first-step decay using the subtraction technique [129] and comparing with the SM, 2) studying the correlation between particles and high-energy γ -rays [130, 131] and 3) measuring the γ -ray spectra in different entrance channels forming the same CN [132]. Another important observation in the early experiments was on the two-component GDR in excited nuclei implying deformation. This was first seen [133] in ^{166}Er which is prolate in its ground state. The deduced oblate shape demonstrated a transition from the prolate to oblate shape at $T \sim 1.6$ MeV. In another experiment [134] on the same nucleus and on ^{160}Er , the deduced shape was prolate at a slightly lower E_X (by ~ 12 MeV). It was realised that the GDR studies provide a powerful tool to explore the evolution of nuclear shape as a function of J and T .

As mentioned earlier, a nucleus manifests both J -driven deformation and T -induced shape fluctuation. The observed GDR width corresponds to an ensemble average over different shapes each exhibiting a single- or a multi-component strength function. At higher rotational frequencies, the Coriolis effect yields a further splitting. Moreover, in the ensemble average, higher values of β are emphasised because of the β^4 -factor in the volume element of the integral (eq. (55)). The extraction of the equilibrium-shape evolution as a function of J , thus, becomes difficult, particularly, at high T . However, this provides the scope of addressing the wider subject of the evolution of the PES around the equilibrium deformation with J and T .

4.1 Statistical GDR up to a moderate T : earlier experiments

In many experimental studies at moderate T (up to ~ 2.5 MeV), the aim was to extract the (T, J) -dependence of the GDR width, addressing the shape evolution and shape fluctuations and comparing with various theoretical models, particularly, the TSFM. In this section, we briefly discuss a few important experiments (reported prior to the year 2000) which have also featured in earlier reviews [7, 14, 15]. The discussion is categorised into various mass regions. A general mass-dependent feature is that for a given J , the angular frequency of rotation is lower in heavier nuclei because of the larger moment of inertia. The J -driven effect on the shape evolution, therefore, shows up at a higher J compared to that in lighter nuclei. In spherical nuclei in the mass region of $A \sim 110$, the shape evolution is generally towards the oblate shape at high J . In the mid-shell region around $A \sim 160$, many nuclei are prolate deformed and eventually change to an oblate shape at high J and/or T . In some heavy nuclei of mass $A \sim 200$, a change from the spherical to prolate shape is predicted. In all cases, the rapidly rotating nuclei in the liquid-drop regime (above a certain T) have the rotation axis mostly along the symmetry axis.

4.1.1 Experiments in light nuclei ($A \leq 100$)

Besides the higher rotational frequency for a given J , the temperature T for a given E_X is also higher in light nuclei as compared to heavy nuclei. The latter arises because of the smaller NLD parameter a . The effect of shape evolution and shape fluctuations is, therefore, generally more pronounced in light nuclei. A spectacular manifestation of the shape transition at high rotational frequency is the Jacobi transition where an oblate nucleus makes a transition to a highly deformed triaxial, almost prolate, nucleus.

The first evidence of the Jacobi transition was seen in ^{45}Sc [135] populated in the $^{18}\text{O} + ^{27}\text{Al}$ reaction at $E_X = 50\text{--}89$ MeV. In these inclusive measurements, the maximum angular momentum J_{max} populated in the CN changed from 20 to 36 at various E_X . From the analysis of the high-energy γ -ray spectra, the GDR width was seen to increase drastically at higher E_X . The fits needed a high-energy GDR component at $E_\gamma \sim 25$ MeV with its strength going up with E_X and, hence, J . The high-energy component implied the GDR vibration along a short axis consistent with a very large deformation. The calculation of the PES showed NC oblate shapes, with the equilibrium deformation parameter β_{eq} changing from 0.09 to 0.26 for J changing from ~ 13 to 24. The phase transition to the Jacobi shape was predicted at $J = 29$ with β_{eq} increasing to ~ 0.68 at $J \sim 32$. The TSFM calculations incorporating these PESs agreed with the experiment for $E_\gamma = 11\text{--}20$ MeV. On the other hand, the calculations, done by switching off the Jacobi transition, failed to explain the data. This finding strengthened the evidence for the shape transition. The angular distribution

measurements, however, were not well reproduced by the calculations.

In the mass region $A \sim 60$, the study was on the general effect of the width increase and the search for very large deformations. In the experiment on ^{63}Cu [136], the CN was formed in four incident channels at $E_X = 22\text{--}77\text{ MeV}$ and $\langle J \rangle \sim 2\text{--}23$, corresponding to $\langle T \rangle = 0.7\text{--}1.9\text{ MeV}$. The extracted GDR widths increased from 7.5 to 10.6 MeV. It was concluded that in this range the effect of T is more pronounced than that of J . In another experiment [137], ^{63}Cu was studied over a higher range of T ($\langle T \rangle = 1.8\text{--}2.5\text{ MeV}$) and for $\langle J \rangle = 15\text{--}23$, using the reaction $^{18}\text{O} + ^{45}\text{Sc}$. In the same work, ^{59}Cu was populated at higher J - and T -ranges ($\langle J \rangle = 13\text{--}32$ and $\langle T \rangle = 1.7\text{--}2.1\text{ MeV}$) using the $^{32}\text{S} + ^{27}\text{Al}$ reaction. The extracted GDR widths ranged from 9.1 to 14.4 MeV signifying a large deformation at high spins. In the case of ^{59}Cu , particularly, the J -range populated at higher E_X was beyond the critical value for the Jacobi transition. The experimental data were compared with the TSFM calculation with the PES, showing the Jacobi transition. The agreement was good for the spectral shape. In this case also, the calculations done by suppressing this shape transition failed to reproduce the data. The angular distribution again was not well reproduced. The evidence of a large J -driven deformation was seen in ^{59}Cu in another experiment [138].

In the experiments on Mo and Zr nuclei [38, 139], the effect of shape fluctuations was clearly manifested. In these inclusive measurements, ^{90}Zr and ^{92}Mo were formed in $^{18}\text{O} + ^{72}\text{Ge}$, $^{28}\text{Si} + ^{64}\text{Ni}$ and $^{16}\text{O} + ^{76}\text{Se}$ reactions with $E_X = 43\text{--}94\text{ MeV}$ and $\langle J \rangle = 9\text{--}33$ with corresponding $\langle T \rangle = 1.35\text{--}2.0\text{ MeV}$. In this range, the equilibrium shape is expected to change from spherical to NC oblate with $\beta_{eq} = 0.02\text{--}0.16$. The SM analysis of the high-energy γ -ray spectra showed a large change in the GDR width from 7.6 to 12.1 MeV although β_{eq} does not change very much. The thermal shape fluctuation is thus the dominant effect. The angular anisotropy data implied an increase of deformation with J . The spectral shape and the angular distributions (for $E_\gamma = 11\text{--}20\text{ MeV}$) agreed with the TSFM calculation including the orientation fluctuation and suggested a spherical to NC oblate shape transition.

An interesting observation was on the comparison between ^{92}Mo and ^{100}Mo , the latter being populated in the $^{18}\text{O} + ^{82}\text{Se}$ reaction at $E_X = 49\text{--}73\text{ MeV}$, $\langle J \rangle = 9\text{--}24$ and $\langle T \rangle = 1.35\text{--}1.45\text{ MeV}$. The extracted GDR widths showed a small change from 9.8 to 10.1 MeV in contrast to that seen in ^{92}Mo . The nucleus ^{92}Mo is semimagic with the $N = 50$ shell closure and has a stiff spherical shape, whereas ^{100}Mo is a softer nucleus due to more neutrons occupying the mid-shell region. This shows up in the GS-GDR widths of $\sim 5.4\text{ MeV}$ for the former and $\sim 7.9\text{ MeV}$ for the latter. Large fluctuations giving rise to a large width is therefore expected in ^{100}Mo even at low T . The difference in the GDR widths of the two nuclei was similar to that in the GS-GDR widths up to $T \sim 1.5\text{ MeV}$. This was interpreted as the persistence of the shell effect up to this T . An extrapolation of the GDR widths to higher T

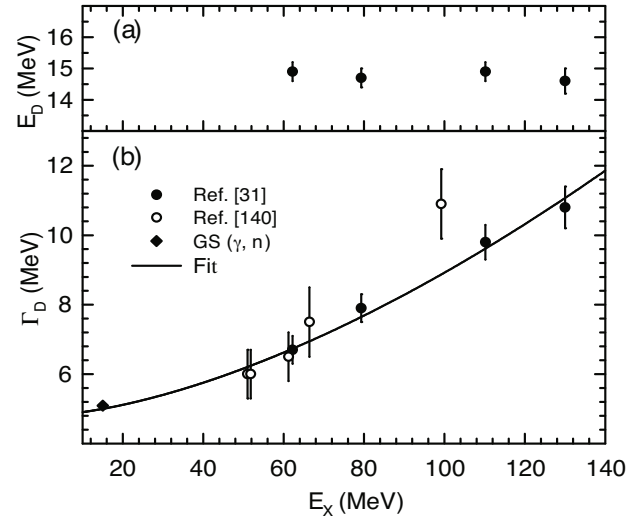


Fig. 6. E_X -dependence of (a) GDR energy and (b) GDR width in Sn-isotopes from different experiments. The GS-GDR width from photoabsorption experiment is also shown. Solid line shows the empirical fit (see text). (Adapted from ref. [31].)

suggested that these would be the same for the two nuclei at $T \sim 2\text{ MeV}$. Although this observation could be interpreted as due to the vanishing of shell effects at the higher T , larger shape fluctuations could also reproduce the same effect.

4.1.2 Experiments in Sn isotopes ($A \sim 106\text{--}120$)

Extensive studies have been made on Sn isotopes, which are spherical in the GS, covering a wide range of E_X and J . In the initial experiments [31, 133, 140], covering the range $E_X \sim 50\text{--}130\text{ MeV}$, an increase of the width with E_X was firmly established (fig. 6). This dependence was parameterised as $\Gamma_D = 4.8 + 0.0026 E_X^{1.6}$ [31]. This relation has often been referred to in the literature. However, in the experiment an increase of E_X was associated with an increase in J . This is not reflected in the above relation. In the same work, the SM calculations were done with a proposed (E_X, J) -dependence of the width at various decay steps. It was not possible to explain the spectra at all excitation energies with only an E_X -dependence of the width but a combined E_X - and J -dependence, *viz.*, $\Gamma_D = 4.5 + 0.0004 E_X^2 + 0.006 J^2$ was needed.

The exclusive J -dependence of the GDR width was experimentally seen [141] by making F-gated measurements in the $^{48}\text{Ti} + ^{61}\text{Ni}$ and $^{48}\text{Ti} + ^{62}\text{Ni}$ reactions populating ^{109}Sn at $E_X = 80\text{ MeV}$ and ^{110}Sn at $E_X = 92\text{ MeV}$, respectively. The GDR width was observed to increase from ~ 11 to 13 MeV for $\langle J \rangle$ changing from 40 to 55. The measured angular distribution of γ -rays, with respect to the beam axis, showed that the a_2 coefficient changed from negative to positive values for E_γ increasing across E_D , as expected for a deformed nucleus. The magnitude of the minimum a_2 increased with J . This observation was supported by the TSFM as against the CDM. According to

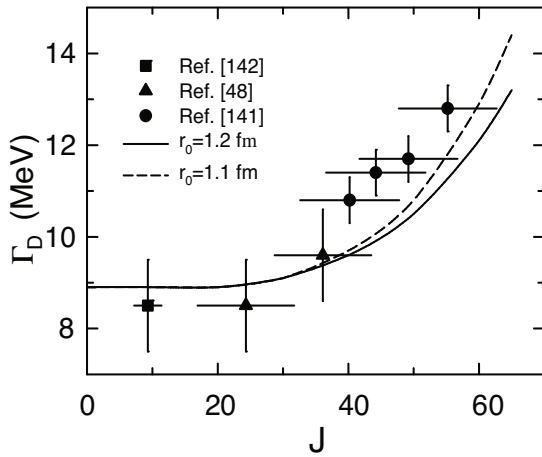


Fig. 7. J -dependence of GDR width in Sn isotopes from different experiments. Solid and dashed lines show results of the TSFM calculations for two moments of inertia defined by different radius parameters r_0 . (Adapted from ref. [48].)

the latter model, the minimum a_2 should not change with J . Thus the observed change in the width was deduced as a J -driven effect consistent with a NC oblate shape with the deformation increasing with J .

The study was extended to a lower J region in an experiment [48] on the $^{58}\text{Ni} + ^{48}\text{Ti}$ reaction populating ^{106}Sn at $E_X = 80$ MeV. The F-gated γ -ray spectra were measured in coincidence with the evaporation residues for suppressing the non-fusion events contaminating the low F-gated data. The GDR width was seen to change from 8.5 to 9.6 MeV for $\langle J \rangle$ changing from 24 to 36. The average temperature was deduced as $\langle T \rangle \sim 1.8$ MeV. Combining the results for higher and much lower values of J (discussed below), it can be concluded that the width increases mildly with J up to $J \sim 30$ and rapidly above this value. This pattern of J -dependence, shown in fig. 7, is consistent with the TSFM because, at a lower J , the effect of the J -driven deformation is masked by the thermal shape fluctuation. However, the value of J at which the rapid increase takes over goes up with A . This happens because the deformation is actually driven by the rotational frequency and for heavier nuclei, as mentioned above, the rotational frequency is less at a given J .

The GDR width at low angular momenta ($J < 20$) was measured using inelastic α -particle scattering exciting the target nucleus over a wide range of E_X and transferring low values of J [143]. Since the effect of J should be small at low values of J , these experiments addressed the exclusive effect of T on the GDR width. High-energy γ -ray spectra, in coincidence with the scattered particles of various energies, were analysed to extract the width. The analysis assumed that the excited target equilibrates to an equivalent CN state (with $E_X = \Delta E$, ΔE being the energy loss of the scattered projectile) before emitting the γ -rays. The experiment was done with ^{120}Sn (and ^{208}Pb) targets using 160 and 200 MeV α -particle beams. The E_X -range studied in ^{120}Sn was 30–130 MeV (and in ^{208}Pb , 40–110 MeV). The extracted GDR widths showed an increase with E_X

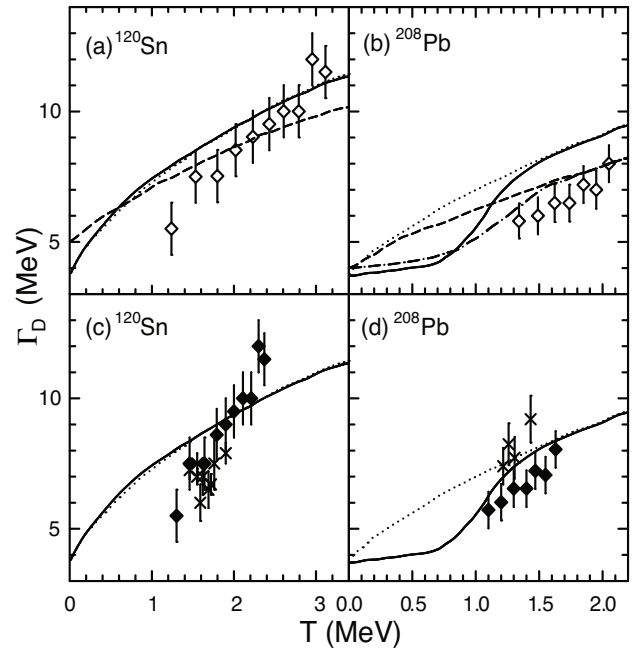


Fig. 8. T -dependence of GDR width in ^{120}Sn and ^{208}Pb . Open diamonds in (a) and (b) are from ref. [143]. In (c) and (d), solid diamonds are reanalysed values while the crosses are other data points in these mass regions (see ref. [117]). Solid and dotted lines are results of the TSFM calculations, with and without shell effects, respectively, of ref. [117]. Dashed and dot-dashed lines are the corresponding results from ref. [109]. (Adapted from ref. [117].)

and, hence, with T . In the original work, T was calculated after subtracting the rotational energy and the GDR energy from E_X in the first step. This does not represent the average temperature over various stages of the multi-step emission of the GDR γ -rays. Using the proper estimates [117] of $\langle T \rangle$, which are less than those quoted in the original papers, the extracted width was seen to increase from ~ 5.5 to 12 MeV for $T = 1.3$ to 2.4 MeV in ^{120}Sn as shown in fig. 8. (For ^{208}Pb , the width increases from ~ 5 to 8 MeV for $T = 1.1$ to 1.7 MeV). The above assumption of $E_X = \Delta E$ was questioned in another work [144]. From the measurement of neutron spectra in coincidence with the scattered α -particles in the reaction $\alpha + ^{209}\text{Bi}$ at $E_b = 240$ MeV, it was concluded that for a given ΔE , there is a range of E_X populated in the target due to the PEQ particle emission. The SM calculation for the effective E_X , under the condition of the subsequent emission of high-energy γ -rays, showed that the average E_X is a fraction of ΔE . The fraction decreases with the increase in ΔE with a typical value of ~ 0.8 for $\Delta E \sim 100$ MeV. This would further reduce the values of $\langle T \rangle$.

The GDR widths obtained within the ACM for ^{120}Sn (and ^{208}Pb) as a function of T are shown in fig. 8. The upper panels, with uncorrected temperatures, show a reasonable agreement with the data. In the case of ^{120}Sn , the agreement improves at higher T after including the effect of the compound nuclear lifetime [145, 146]. (The inclusion of shell effects was important in the case of ^{208}Pb .) These

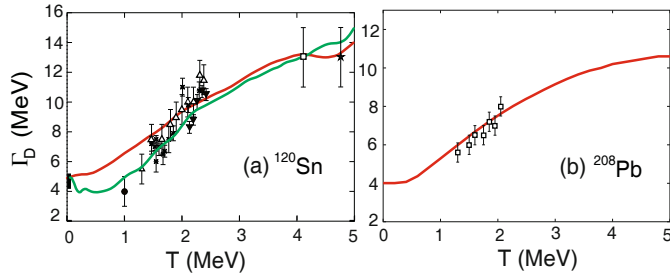


Fig. 9. GDR widths in (a) Sn isotopes and (b) ^{208}Pb and predictions of the PDM. In (a) solid circle is from ref. [147], open triangles are from ref. [117], open square and star are from refs. [148,149] (with uncorrected T), the GS-GDR ($T = 0$ MeV) width is for Sn isotopes with $A = 116\text{--}124$ [150] and other data points are from ref. [151]. In (b) data points are from ref. [143]. Green and red lines show calculations (for ^{120}Sn and ^{208}Pb) with and without pairing, respectively.

TSFM calculations were repeated by another group [117]. The calculated widths in ref. [117] for ^{120}Sn are, however, larger than those of ref. [109] at large T , despite the fact that a lower value of $T_0 = 3.8$ MeV was used in the former case as compared to 5 MeV in the latter. (For ^{208}Pb a similar discrepancy was seen.) The lower panels show the comparison of the calculation of ref. [117] with the T -corrected data. As can be seen, the agreement is reasonable for ^{208}Pb but not quite so for ^{120}Sn , particularly, at lower T (below ~ 1.5 MeV). The failure of the TSFM at low T was later seen for other nuclei (discussed later).

The GDR widths obtained within the PDM for Sn isotopes are shown in fig. 9(a). The comparison with the data up to a moderate T (obtained from the experiments discussed so far) is good and reveals the important role of thermal pairing at low T . The temperatures for the data points beyond $T = 4$ MeV, however, were corrected later and the apparent experimental saturation of the GDR width is thus debatable (see later). (The results of the PDM calculations for the GDR width in ^{208}Pb agree well with the data as shown in fig. 9(b). However, the comparison using the corrected values of T would worsen the good agreement with the data.)

The GDR widths calculated using the CDM for ^{120}Sn (and ^{208}Pb) are shown in fig. 10 in comparison with the experimental data. The calculations agree reasonably well with the experiment when the vacuum NN scattering cross-sections are used and strongly underestimate the data if the in-medium NN scattering cross-sections are used instead. The experimental data in this figure are, however, shown with uncorrected T . The calculated widths increase with T without any sign of saturation.

The question of the saturation of the GDR width at higher T , which will be discussed in a later section, was addressed in an experiment [151] on the $^{18}\text{O} + ^{100}\text{Mo}$ reaction populating ^{118}Sn at various E_b between 125 and 217 MeV. An important point established in this work was that the effect of PEQ particle emission should be included [152] for getting the proper estimate of E_X , A and Z of the equilibrated source emitting GDR γ -rays. Moreover, its temperature should be calculated from the

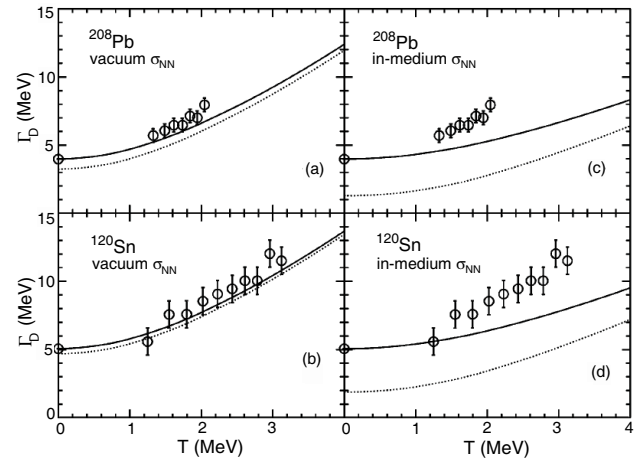


Fig. 10. Experimental GDR widths (open circles) for ^{208}Pb ((a), (c)) and ^{120}Sn ((b), (d)) from ref. [143] and the predictions of CDM. Solid and dotted lines, respectively, are with and without wall friction contribution. Results shown in (a) and (b) are obtained using vacuum NN scattering cross-sections and those in (c) and (d), using in-medium NN cross-sections. (Adapted from ref. [99].)

weighted average $\langle E_X \rangle$ over the decay steps starting with the PEQ-corrected initial E_X . The analysis revealed a continuous increase of the extracted GDR widths from ~ 8.3 to 10.6 MeV for T changing from 2.14 to 2.42 MeV. The TSFM calculations showed an overall agreement with the data.

4.1.3 Experiments in Er-Dy-Gd isotopes ($A \sim 154\text{--}166$)

The evolution of the nuclear shape, from prolate to oblate, and the effect of the shape fluctuation have been mainly addressed in these nuclei which have ground-state deformation. A general comment is worth making at this point. In the case of large thermal shape fluctuations, as is expected in many experiments, the extraction of the deformation parameter β , just from the energies of the two-component GDR fitting the measured γ -ray spectrum, is not meaningful. This gives neither the equilibrium deformation β_{eq} nor the ensemble-averaged deformation $\langle \beta \rangle$ [38]. The angular anisotropy data cannot definitely establish the shape because of the dilution caused by the shape and orientation fluctuations. These points should be borne in mind while appreciating the conclusions drawn about the shape change in many experimental works.

As mentioned earlier, the first evidence for deformation was seen in excited Er nuclei. The results of the two inclusive experiments [133, 134] on ^{166}Er were consistent with a prolate to oblate shape transition at $T \sim 1.6$ MeV. On the other hand, in a subsequent experiment on ^{160}Er [153], populated in the reaction $^{19}\text{F} + ^{141}\text{Pr}$ at $E_X = 59\text{--}90$ MeV, it was concluded that none of the prolate, oblate or triaxial shapes of the excited nuclei could be discarded and no obvious abrupt shape transition was evidenced with the increase in E_X .

In a J -gated measurement [149] on ^{166}Er and ^{158}Er at $E_X = 60$ and 47 MeV, respectively, γ -ray spectra were

measured for $\langle J \rangle = 12, 20$ and 26 . The SM analysis, using a two-component GDR strength function, concluded that ^{166}Er shows a prolate to oblate shape transition with the increase in J . For ^{158}Er , the shape was deduced to be oblate even at low J with the value of β increasing with J . This was attributed to the relative softness of ^{158}Er .

In an experiment on the shape evolution in ^{156}Dy [154], populated at $E_X = 75$ MeV, γ -ray spectra and angular distributions were measured for $\langle J \rangle = 18, 28$, and 40 . A shape transition from prolate at $J = 18$ to oblate at $J = 40$ was deduced, with a reduction in β from 0.36 to 0.19 . A comparison of the calculated and experimental anisotropies for $J = 18$ and 40 , however, could not distinguish between collective prolate or NC oblate shapes.

In another experiment [155] on the same nucleus at a higher $E_X = 90$ MeV, a similar conclusion was reached. The data pointed towards a change of shape from prolate at $\langle J \rangle = 32$, with $\beta = 0.16$, to oblate at higher $\langle J \rangle$ up to 62 , with β increasing from 0.13 to 0.28 . However, when the experiment was repeated [156] with a thinner target, no definite evidence for a prolate to oblate shape transition was seen. The experimental data could be understood by the TSFM calculations which utilised the PES with a NC oblate minimum at all J with the magnitude of β_{eq} going up with J . However, the ensemble-averaged $\langle \beta \rangle$ changes very little with J thus masking the shape change effect.

The same experimental group reported the measurements of F-gated γ -ray spectra from the CN ^{154}Dy and those in coincidence with high-spin isomers from the CNs ^{156}Dy and ^{154}Dy . The latter condition selected a higher J -range and a narrower E_X -range. For ^{156}Dy [157], the isomer-gated spectra, for $J = 30$ – 65 and $T = 1.6$ – 1.9 MeV, showed an oblate shape whereas both oblate and prolate shapes were acceptable for the ungated spectra. The magnitude of β in both cases was derived as ~ 0.3 . For ^{154}Dy [158, 159], the isomer-gated spectra, for $J = 30$ – 50 and $T = 1.35$ – 1.55 MeV, showed a large deformation of $\beta \sim 0.4$ – 0.5 with both prolate and oblate shapes. The analysis of the J -dependent and prompt γ -ray-gated spectra showed a large increase of width with J , changing by 40 – 50% for $\langle J \rangle$ changing from 32 to 50 .

A similar observation was made on Gd isotopes. In a study [160] on ^{154}Gd at $E_X = 80$ MeV, high-energy γ -rays were measured in the 8π -spectrometer in Chalk River. Angular distributions were measured with respect to the spin axis defined by the plane of the low-energy electric quadrupole $E2$ γ -rays. For $\langle J \rangle = 27$ – 55 , an increase in deformation with J was deduced with $\beta = 0.08$ – 0.35 . Interestingly, however, the shape was deduced as prolate even at higher J values. The conclusion was supported by the angular distribution data. This is in contrast to the general behaviour of the prolate or spherical nuclei attaining a NC oblate shape at high J and T . The authors, however, did not present any PES calculation for this case.

4.1.4 Experiments in heavy nuclei ($A > 170$)

In heavy nuclei with small GS deformation, the experiments addressed the spherical to prolate shape evolu-

tion, the effects of shape fluctuations and the emission of GDR γ -rays in competition with the fission process. In $A \sim 200$ region, an evolution from the spherical to prolate shape was predicted theoretically. For example, a calculation [161] showed that ^{196}Pb has a superdeformed minimum with $\beta = 0.5$ at $T = 0$ MeV and $J \sim 30$. At $T \sim 0.8$ MeV, the depth of the potential minimum reduces making the PES flatter with an average $\beta \sim 0.35$. At still higher T , the deformation minimum vanishes. A general problem in the experiments in heavy nuclei is worth mentioning here. In many cases, the fission cross-section is significant and the contribution to the γ -ray spectrum from the excited fission fragments must be calculated and subtracted before making the SM analysis.

The first evidence of the J -induced deformation in spherical Pb nuclei of $A \sim 200$ was reported [162] from a study of $^{16}\text{O} + \text{W}$ and $^{19}\text{F} + ^{181}\text{Ta}$ reactions, populating the isotopes 198 – ^{202}Pb at $E_X = 66$ – 102 MeV and with $J_{max} \sim 38$ – 66 . The measured γ -ray spectrum at the lowest E_X was described with a two-component GDR corresponding to a prolate shape. In a subsequent experiment [163], populating ^{200}Pb at a lower $E_X = 57.6$ MeV and $J_{max} \sim 22$, an evolution of the shape from spherical, below $J \sim 16$, to prolate, at higher J , was deduced. The earlier data at $E_X = 66$ MeV was also found to be consistent with such a conclusion. The extracted values of β were almost the same (~ 0.37 and 0.41) at both E_X corresponding to $T \sim 0.9$ and 1.1 MeV. In an exclusive measurement [164], on the same reaction at $E_b = 105$ and 141 MeV, fission-fragment-gated γ -ray spectra and the angular anisotropy with respect to the spin axis (constructed from the fragment directions) were measured. At the lower E_b , a slightly larger $\beta \sim 0.43$ was derived from the data analysis. Noting that the fission-fragment-gating selects a higher J -range, all these findings showed a J -driven deformation and are generally consistent with the theoretical predictions mentioned above. The observation of the spherical to prolate shape transition was corroborated in a later M_γ -gated measurement [165] on the $^{19}\text{F} + ^{181}\text{Ta}$ reaction at $E_b = 101$ MeV.

The general feature of the J -induced deformation in this mass region was seen in another work [166] on the $^{16}\text{O} + ^{181}\text{Ta}$ reaction populating ^{197}Tl at $E_X \sim 60$ MeV. The measured γ -ray spectra and angular distributions could be described by a two-component GDR implying the J -induced deformation. A Gaussian-parameterised shape- and orientation-fluctuation calculation established a deformation slightly increasing ($\beta \sim 0.26$ – 0.29) with J and a drive towards triaxiality at high J .

In an exclusive measurement [167], the reaction $^{48}\text{Ca} + ^{142}\text{Nd}$ populated ^{190}Hg at $E_X \sim 52$ MeV. High-energy γ -ray spectra were measured in coincidence with specific ERs. The spectrum gated with ^{188}Hg was analysed with a Monte Carlo version of the CASCADE code. Over the J -range populated up to ~ 28 , a prolate shape of $\beta \sim 0.28$ was deduced. In another measurement, addressing the J -dependence of the GDR width [168] in Hg isotopes at higher E_X , the reaction $^{30}\text{Si} + ^{164}\text{Dy}$ populated ^{194}Hg at $E_X = 60$ MeV. High-energy γ -ray spectra were created with M_γ -gating as well as in coincidence with the γ -rays

from the ERs. The GDR widths extracted from the analysis were the same (~ 6.2 MeV), within error bars, for $\langle J \rangle = 24\text{--}36$ and $\langle T \rangle \sim 1.3$ MeV. Results of the TSFM calculation agreed with the experiment. The ensemble-averaged deformation was calculated as $\langle \beta \rangle \sim 0.3$, much higher than $\beta_{eq} (< 0.05)$, at all J . The small values of β_{eq} were related to the small rotational frequencies in these heavy nuclei. These observations are different from those in Pb isotopes showing a large J -driven deformation. A search for the superdeformation in Hg isotopes from this experiment yielded no positive result.

A similar conclusion was derived [169] from an experiment on ^{176}W formed in the reaction $^{28}\text{Si} + ^{148}\text{Nd}$ at $E_X = 75$ MeV. The extracted GDR widths for $\langle J \rangle = 36\text{--}45$ and $\langle T \rangle \sim 1.4\text{--}1.5$ MeV showed a very small change from 8.4 to 8.9 MeV. The TSFM calculation, including the orientation fluctuation, showed a reasonable agreement with the spectral shape and the measured angular distributions. The calculated β_{eq} of the NC oblate shapes changed from 0.06 to 0.14 for $J = 35$ to 55 and the ensemble averaging produced an almost J -independent $\langle \beta \rangle$.

In an experiment [170] on the $^{16}\text{O} + ^{159}\text{Tb}$ reaction populating ^{175}Ta at a higher $E_X = 123$ MeV, both ER- and fission-fragment-gated γ -ray spectra were measured. The ER-gated spectrum was consistent with $\beta \sim 0.24$ whereas the fission-fragment-gated spectrum was consistent with a large $\beta \sim 0.55$. In the latter case, the pre-fission γ -rays were emitted from a higher J -range 60–80 and $T \sim 1.8$ MeV. Various interesting speculations were made to understand the results. These included the Jacobi transition near the fission limit in this heavy nucleus and the emission of γ -rays during the journey towards the saddle point sampling very large deformations.

As a last example, we discuss an experiment [171] in a very heavy nucleus ^{272}Hs populated in the reaction $^{40}\text{Ar} + ^{232}\text{Th}$ at $E_b = 6.8, 10.5$ and 15 MeV/nucleon. The extraction of the GDR γ -rays from this highly fissile CN is feasible if the large contribution from the fission fragments can be experimentally suppressed. This was possible because of the delay in the fission process arising due to the effect of viscosity of the nuclear fluid in the journey to the scission point [16]. During this process, the CN cools to a low excitation energy, say, E_f before it fissions. If the experiment is done at two excitation energies, both above E_f , the subtracted spectrum from these two measurements should eliminate the fission-fragment contribution. In this experiment, the difference spectrum (after subtracting the bremsstrahlung component), for $E_b = 15$ and 10.5 MeV/nucleon, showed no post-fission γ -rays whereas that measured for $E_b = 10.5$ and 6.8 MeV/nucleon showed such a component. This implied that the fission process is indeed delayed and starts between $E_X = 92$ and 218 MeV. The first difference spectrum showed a nice bump at $E_\gamma \sim 12.2$ MeV corresponding to the GDR in the superheavy nucleus ^{272}Hs . The spectral shape was consistent with either a prolate or an oblate shape of $\beta \sim 0.19$. The angular distribution, measured with respect to the spin axis, agreed with this conclusion.

4.2 Statistical GDR up to a moderate T: recent experiments

The experimental work reported in the years 2000 onwards can be classified into three categories. In category A, the experiments further addressed the general feature of the (T, J) -dependence of the GDR damping. In category B, the experimental results showed a deviation from the widely applied TSFM. In category C, the experiments addressed the GDR in highly deformed nuclei manifesting the Jacobi transition and superdeformed shapes.

4.2.1 Category A

In an experiment [172], performed at the Niels Bohr Institute (NBI), ^{147}Eu was populated in the $^{37}\text{Cl} + ^{110}\text{Pd}$ reaction at $E_X = 74\text{--}81$ MeV and $J_{max} \sim 58\text{--}65$. The F-gated high-energy γ -ray spectra were measured in the HECTOR array. Spectra were also measured in coincidence with the characteristic γ -ray transitions in various ERs detected in the NORDBALL array. The SM analysis of the spectra, for $\langle J \rangle = 37\text{--}50$ and $\langle T \rangle = 1.22\text{--}1.36$ MeV, showed that the GDR width varies over a small range 8.4–8.9 MeV. The TSFM calculations of the GDR widths agreed with the experiment. The overall conclusion, after considering the earlier results for Sn and heavier mass region, was that the J -dependence of the GDR width is pronounced in Sn isotopes of $A \sim 110$, weak in $A \sim 176\text{--}190$ region and of an intermediate nature in the ^{147}Eu region. These observations are consistent, as mentioned earlier, with the importance of the rotational frequency (decreasing with A for a given J) in deciding the J -driven effects on the GDR width.

In the heavier mass region, an experiment, performed in Legnaro, was reported [173] on ^{216}Rn populated at $E_X = 56$ MeV in the $^{18}\text{O} + ^{198}\text{Pt}$ reaction. The motivation was to study the GDR strength function up to the J -range near the fission limit and to look for large deformations seen in lighter nuclei. The experiment was done using the HECTOR array for detecting high-energy γ -rays in coincidence with a BGO-array for measuring M_γ . In addition, measurements were made in coincidence with delayed γ -rays, detected by BGO detectors placed around a catcher foil, from two isomers in ^{212}Rn ($J = 30, 154$ ns) and ^{211}Rn ($J = 63/2, 201$ ns). This selected high- $J \sim 40$ near the fission limit. For $\langle J \rangle = 23\text{--}35$, the extracted GDR widths were almost constant at $\sim 7.0\text{--}7.3$ MeV showing no pronounced J -induced effect. The temperature in each case was ~ 1 MeV. The TSFM calculations were done with the PES calculated using the LSD model [112, 113] for the liquid-drop part. The shell effect was assumed to vanish at $T \sim 1$ MeV. The calculated β_{eq} was almost zero at $T = 1$ MeV for J up to 40 (with a very mild increase above $J = 30$). This, thus, showed no effect like the Jacobi transition seen in light nuclei (mentioned earlier). The ensemble-averaged $\langle \beta \rangle$ was ~ 0.1 at all J resulting in an almost constant GDR width independent of J . The LSD model, predicting a nearly spherical shape in ^{216}Rn and the Jacobi transition in ^{46}Ti (discussed later) at J near

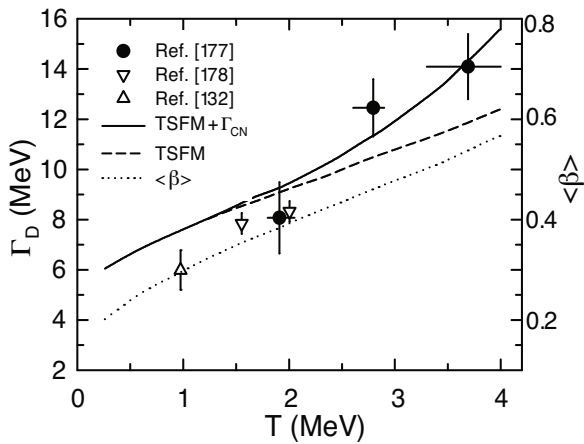


Fig. 11. Experimental and calculated GDR widths in $A \sim 130$ nuclei. Solid and dashed lines are results of the TSFM calculations with and without Γ_{CN} contribution, respectively. The dotted line shows the calculated average β . (Adapted from ref. [177].)

the fission limit was thus successful in describing the nuclear shape evolution in two widely different mass regions (see fig. 25 later).

The agreement between the experimental data and the TSFM calculations was seen in ^{113}Sb [174] at $\langle T \rangle = 1.7\text{--}2\text{ MeV}$ and $\langle J \rangle = 41\text{--}54$ and in ^{144}Sm [175, 176] at $\langle T \rangle = 1.1\text{--}2.1\text{ MeV}$ and $\langle J \rangle \sim 25\text{--}65$. The experiments, performed in coincidence with M_γ -detector arrays, were reported from the VECC and the IUAC groups, respectively. In the latter experiment, the disentangling of the effects of T and J on the GDR width revealed a mild dependence on T and a strong dependence on J . This was attributed, from the TSFM calculations, to an increasing softness towards triaxial deformation at higher J .

The necessity of incorporating the contribution from the decay widths of the CN (Γ_{CN}) to the GDR width was seen in an experiment [177], performed in Legnaro, populating ^{132}Ce at $E_X = 100\text{--}200\text{ MeV}$ in the reaction $^{64}\text{Ni} + ^{68}\text{Zn}$. High-energy γ -ray spectra were measured with the HECTOR array in coincidence with ERs detected in PPACs. The formation of an equilibrated CN was established by measuring the α -particle spectra, which could be reproduced by the SM calculations. The angular momenta populated in the CN at all E_X were in the same range, being limited by the fission process, with $\langle J \rangle = 45$. The GDR widths, extracted from the SM analysis done with an E_X -dependent NLD parameter, showed (fig. 11) an increase from 8 to 14 MeV for $\langle T \rangle$ increasing from 2 to 3.7 MeV. The results of the TSFM calculations were compared with the experimental widths including those from earlier measurements at lower T (and J) in this mass region. The agreement was reasonably good for $T \leq 2\text{ MeV}$. At higher T , the experimental widths could be reproduced after the inclusion of Γ_{CN} . The authors concluded that, the data did not leave room for any other effect, such as the collisional damping, to explain the GDR width. It should, however, be mentioned that in this work, $\langle T \rangle$

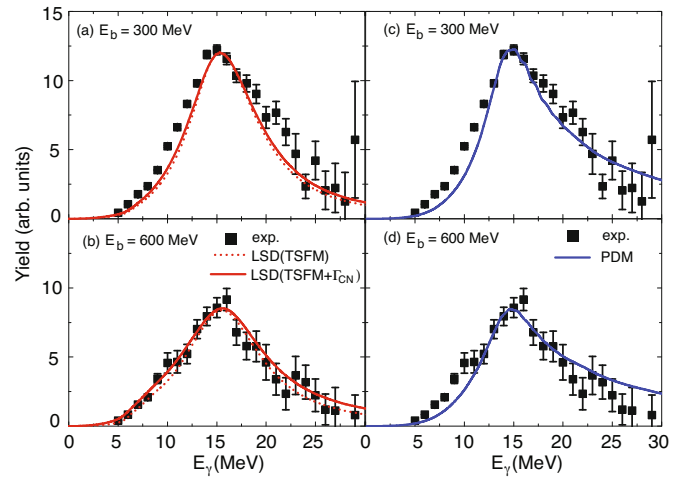


Fig. 12. (Colour online) Experimental GDR strength functions in ^{88}Mo at two E_X corresponding to the indicated beam energies in $^{48}\text{Ti} + ^{40}\text{Ca}$ reaction. Results of the TSFM (including Γ_{CN} contribution) ((a), (b)) and PDM ((c), (d)) calculations are shown by continuous lines. Dotted lines in (a), (b) are TSFM results without Γ_{CN} contribution. (Adapted from ref. [179].)

was extracted from the SM calculation after introducing a lower cut-off in E_X corresponding to $\sim 50\%$ of the total yield of the GDR γ -rays. This, in principle, is not necessary because below a certain E_X , the contribution to the γ -ray spectrum in the GDR region becomes low. Hence, the corresponding weight factors in calculating $\langle T \rangle$ are also reduced. Without incorporating the lower cut-off, the values of $\langle T \rangle$ would be lower. This would imply a faster increase of GDR width with T and could suggest the need for other effects beyond the TSFM and that from Γ_{CN} .

In a very recent experiment [179] done in Legnaro, ^{88}Mo was populated at $E_X = 124$ and 261 MeV in the reaction $^{48}\text{Ti} + ^{40}\text{Ca}$. High-energy γ -rays were measured with the HECTOR array in coincidence with ERs detected in phoswich detectors. As in the work mentioned earlier, the proton and α -particle spectra, measured with the GARFIELD [180, 181] detector array, could be explained by the SM calculation establishing the absence of any non-compound events. The maximum J populated at both energies was limited to 64 due to the fission process at higher J . The analysis of the bremsstrahlung-subtracted γ -ray (and particle) spectra was done with the Monte Carlo code GEMINI++ [182]. The same value of the GDR width was assumed at each decay step following the usual practice. The GDR widths were deduced from the extracted effective GDR strength functions shown in fig. 12. The widths (representing an average over various decay steps) at the two E_X were almost the same, *viz.*, ~ 9.9 and 10.3 MeV , within error bars (fig. 13). The corresponding values of $\langle T \rangle$ were obtained from an elaborate calculation with the Monte Carlo code as 2.0 and 3.1 MeV , respectively. These were extracted without introducing a lower cut-off in E_X , as was done in the earlier work. The spread in T around the mean values were ~ 1.1 and 1.5 MeV , respectively, at the two energies.

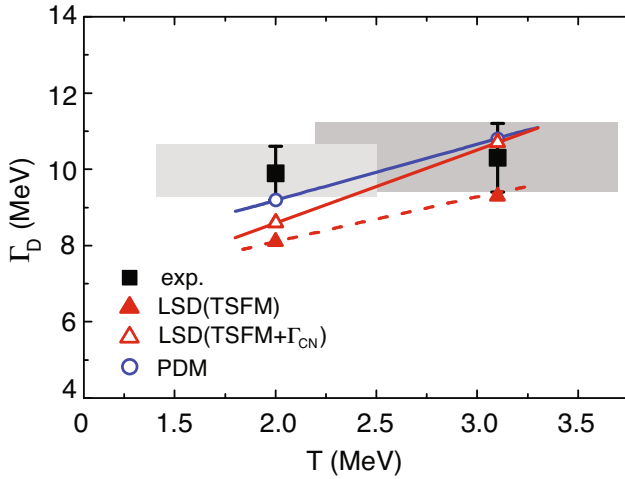


Fig. 13. (Colour online) Experimental and calculated (with the models mentioned in fig. 12) GDR widths in ^{88}Mo at two T . (Adapted from ref. [179].)

The experimentally extracted effective strength functions and the GDR widths were compared with calculations done within the TSFM and the PDM. In the first case, the liquid-drop part of the PES was calculated within the LSD model. The calculations were done at various values of J , T and A encountered by the decaying nucleus in the cooling process. The average strength function for each case was calculated using an ensemble average over various deformations due to thermal fluctuations. Finally, these were further averaged over the distribution of T , J and A , populated at various stages, as given by the Monte Carlo calculations. It was necessary to include the contribution from the evaporation width Γ_{CN} . This T -dependent contribution was calculated using the SM. The calculation within the PDM was also carried out for various T and J and averaged over the above-mentioned distributions.

The comparisons of the calculated effective strength functions and the GDR widths with the experiment are shown in figs. 12 and 13. The agreement is good at the higher E_X . At the lower E_X , the calculated width using the TSFM (including Γ_{CN}) is ~ 1.5 MeV less than the experimental value. Thus, the increase of GDR width with T is faster in the TSFM model as compared to the experimental data. The PDM results at both energies are closer to the data. The shape of the strength functions for $E_\gamma < 12$ MeV was not very well described at the higher E_X . However, this could be due to the neglect of the Coriolis splitting in the PDM calculations.

The dependence of the measured GDR width on T is weaker compared to the observation in ^{132}Ce [177]. This can be related to the higher rotational frequency and the associated deformation effect which are similar at both E_X . Another possibility is the width saturation at $T \sim 3$ MeV. This was corroborated by comparing the derived widths in this work with the ones from earlier measurements (fig. 14) for various Mo isotopes. The figure shows a fast increase of the experimental GDR width with T for $T < 2$ MeV and a flattening out at higher T .

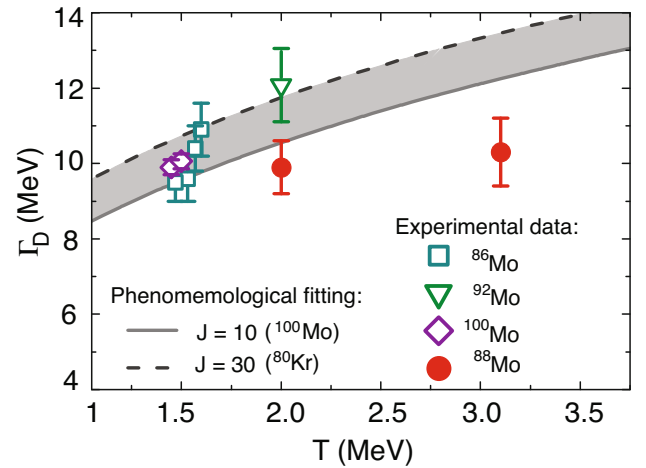


Fig. 14. (Colour online) Experimental GDR widths in various Mo isotopes as a function of T . Data are obtained from ref. [179] and other experiments cited in this reference. Lines show the predictions of pTSFM [117]. (Adapted from ref. [179].)

4.2.2 Category B

The overall success of the TSFM, seen in the previous examples, has been confronted in many cases showing a discrepancy between its prediction and the experimental data. This, particularly, has been the case at low T below ~ 1.5 MeV. In the work on the scaling properties of the TSFM calculations [117] done in the liquid-drop regime, it was seen that for $^{59,63}\text{Cu}$ and Sn isotopes, the TSFM calculations overestimate the GDR widths at low T . In ^{208}Pb , the shell effect was the reason of the discrepancy at low T . However, data for $T \leq 1$ MeV were very sparse for making a definite conclusion about the discrepancy.

In an exclusive measurement [183] on the reaction $^{90}\text{Zr} + ^{89}\text{Y}$ populating ^{179}Au at $E_X \sim 20$ MeV, high-energy γ -rays were measured in four arrays of 37-element BaF_2 detectors in coincidence with ERs detected in the Fragment Mass Analyser (FMA) at ANL. This measurement addressed the GDR at $T \sim 0.7$ MeV and for $J_{max} \sim 16$. The γ -ray spectrum in coincidence with ^{179}Au detected in the FMA extended to $E_\gamma \sim 14$ MeV. In the data analysis, a split GDR strength function was used with the component energies corresponding to $E_{D0} = 14.2$ MeV and $\delta = 1.6$ in eqs. (4) and (5). The parameters β , γ and Γ_0 were varied to fit the data. The best fit to the γ -ray spectrum was obtained with $\beta = 0.1 \pm 0.1$ and $\Gamma_0 = 5.0 \pm 0.35$ MeV. Since no TSFM calculation was available for ^{179}Au , the authors made a comparison with the calculated widths for ^{208}Pb after incorporating an approximate extrapolation. The value without the shell correction (as should be the case for ^{179}Au) was ~ 6.4 MeV which was more than the experimental value. However, the comparison should be made not with the extracted Γ_0 but with the actual FWHM of the strength function. Taking $\beta = 0.1$, the calculated FWHM would be ~ 0.5 MeV more than Γ_0 , thus, making the discrepancy smaller. The authors, however, concluded that detailed

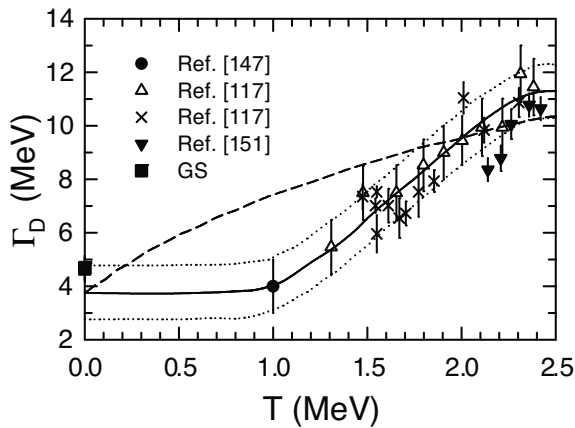


Fig. 15. Experimental GDR widths in Sn isotopes as a function of T from different experiments. Solid line guides the eye through the measured widths. Dotted lines denote the experimental uncertainty. Dashed curve is the TSFM prediction. (Adapted from ref. [147].)

calculations are needed before drawing any conclusion about the disagreement.

In an experiment [147] on ^{120}Sn , high-energy γ -rays were detected in two large arrays of 68-element BaF_2 detectors in coincidence with the inelastically scattered ^{17}O projectile. The experiment was performed at the NSCL Michigan, using a 80 MeV/nucleon beam and the scattered particles were detected in a magnetic spectrometer. The spectra were created for various energies of ^{17}O corresponding to the energy loss (ΔE) of 20–90 MeV. For the lowest ΔE bin of 20–30 MeV, E_X in ^{120}Sn was taken to be the same as ΔE . The SM analysis, done with a fixed width at each decay step, extracted the average GDR width as ~ 4.0 MeV at $\langle T \rangle \sim 1.0$ MeV. For the higher ΔE bins, a distribution of E_X was used, guided by earlier experiments [144], in the SM analysis. The analysis was done with a different approach. A smooth curve was drawn through the widths obtained from the earlier experiments at higher T and the derived value of 1 MeV for the lowest ΔE bin (fig. 15). This T -dependence is at variance with the TSFM calculation. The γ -ray spectra calculated with this T -dependence of the width incorporated at different decay steps, agreed with experiment for all ΔE bins. This observation established that the TSFM overestimates the width up to $T \sim 1.7$ MeV.

In another experiment [184] on ^{117}Sn and ^{118}Sn at $E_X = 70.4$ and 84.6 MeV populated in the reactions $^{17}\text{O} + ^{100}\text{Mo}$ and $^{18}\text{O} + ^{100}\text{Mo}$, respectively, high-energy γ -rays were measured in four arrays of 37-element BaF_2 detectors in coincidence with ERs detected by the FMA at ANL. In the SM calculations done with the GDR width changing with T and J at each decay step, the above-mentioned T -dependence was used. The J -dependence was taken as that prescribed by the TSFM, guided by the results from ref. [48]. The measured spectra could be reproduced with these prescriptions implying again a failure of the TSFM at low T in these systems.

A series of experiments was reported recently, by the VECC group, using α -particle as the projectile. High-

energy γ -ray spectra were measured by the LAMBDA array in coincidence with a M_γ -detector array. Neutron spectra were measured in some cases to constrain the NLD parameter in the SM analysis. The bremsstrahlung contribution was estimated from the forward-backward asymmetry of the γ -ray yield and subtracted from the measured spectra. For the CN ^{119}Sb populated at $E_X = 31.4$ – 43.0 MeV [185], the extracted GDR widths were in the range ~ 3.9 to 5.8 MeV for $\langle T \rangle$ changing from 0.9 to 1.4 MeV. In another experiment [186], measurements were made on the compound nuclei ^{201}Tl and ^{63}Cu . An analysis of the F-gated γ -ray spectra showed that the extracted widths in ^{201}Tl changed from 3.4 to 4.5 MeV for $\langle T \rangle$ in the range 0.8 – 1.12 MeV. In ^{63}Cu , the widths were 7.5 and 8 MeV at $\langle T \rangle = 1.15$ and 1.3 MeV, respectively. The predicted widths by the TSFM, in all cases, were larger than the experimental values. Combining with the earlier data [136, 143] in ^{63}Cu , ^{120}Sn and ^{208}Pb regions, a systematic trend of a constant width up to a certain temperature T_c and an increase at higher T , was deduced (fig. 16). The extracted T_c was seen to decrease with A following an empirical relation $T_c = 0.7 + 37.5/A$. In the third experiment [187] on ^{97}Tc ($E_X = 29.3$ – 50.4 MeV), the extracted widths showed an increase from 5.5 to 7.5 MeV for $\langle T \rangle$ changing from 0.8 to 1.51 MeV. The widths, which were lower than the TSFM values, also followed the above trend of remaining constant up to $T \sim 1$ MeV and increasing at higher T . The data have been compared with the results of the PDM calculations. In all these cases, the PDM predictions agreed with the data (see figs. 9 and 17) after the inclusion of the pairing correlation and its fluctuation. As mentioned earlier, the fluctuations make the pairing correlation decrease monotonically with T without an abrupt vanishing at a critical temperature.

A critical temperature fluctuation model (CTFM) was introduced by the VECC group [186] to explain the suppression of the width with respect to the TSFM. This was based on the assertion [188] that the GDR itself induces a quadrupole moment as the oscillating incompressible neutron and proton fluids distort the surface (in the Goldhaber-Teller picture). It was conjectured that if the extent of the deformation $\Delta\beta$ due to the thermal shape fluctuation is insignificant with respect to the induced deformation β_{GDR} due to GDR vibration, the GDR width should remain at the GS value up to a $T = T_c$ at which $\Delta\beta$ and β_{GDR} become comparable. This argument was based on the observation within the TSFM where $\beta_{eq} < \Delta\beta$ at low J and the effect of the J -induced deformation on the GDR width is masked by the larger contribution from the shape fluctuation. In the CTFM, $\Delta\beta < \beta_{GDR}$ at low T so that the effect of the thermal fluctuation on the width is assumed to be small. This would, however, imply that the GDR width should be at least equal to the contribution from the shape fluctuation. It is not clear how the GDR-induced deformation can suppress this contribution. Moreover, the widths at $T > T_c$ were obtained by a fitting formula to mimic the increase of the width with T and J . This model is, therefore, purely empirical although it reasonably describes the experimental data in many cases as shown in fig. 16.

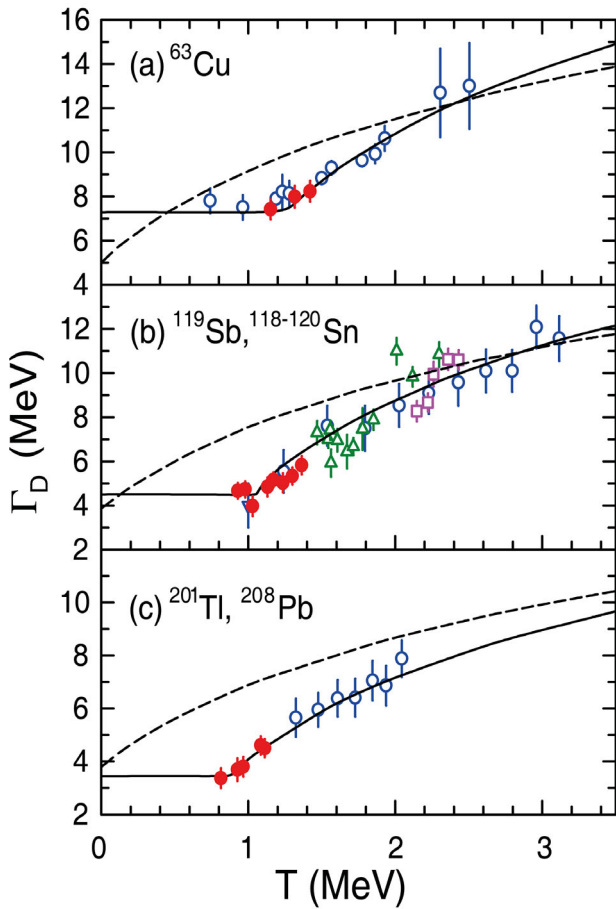


Fig. 16. (Colour online) T -dependence of experimental GDR width from various experiments. Filled circles are for ^{63}Cu (a), ^{119}Sb (b) and ^{201}Tl (c) from ref. [186]. Open symbols are for ^{63}Cu (a), $^{118-120}\text{Sb}$ (b) and ^{208}Pb (c) from experiments mentioned in ref. [186]. Dashed curves are the TSFM predictions without shell effect. Full lines are the CTFM results. Data for Sn and Pb are shown with uncorrected T . (Adapted from ref. [186].)

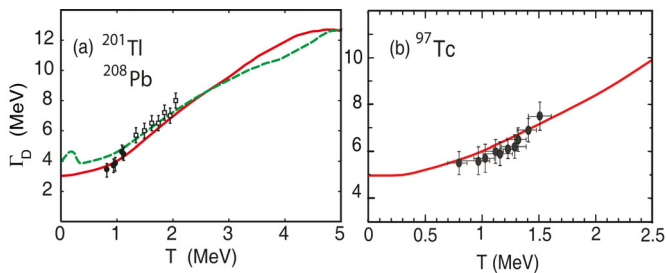


Fig. 17. (Colour online) Experimental GDR widths in (a) ^{201}Tl (filled circles) and ^{208}Pb (open squares) and (b) ^{97}Tc . In (a) data for ^{208}Pb are shown with uncorrected T . Solid and dashed lines are predictions of the PDM, for ^{201}Tl (a) and ^{97}Tc (b), with and without pairing, respectively.

It should be mentioned at this point that the systematic observation of the GDR width at $T \leq 1$ MeV being equal to the GS value is not consistent with one earlier observation on ^{114}Sn [189]. The measured width at a low

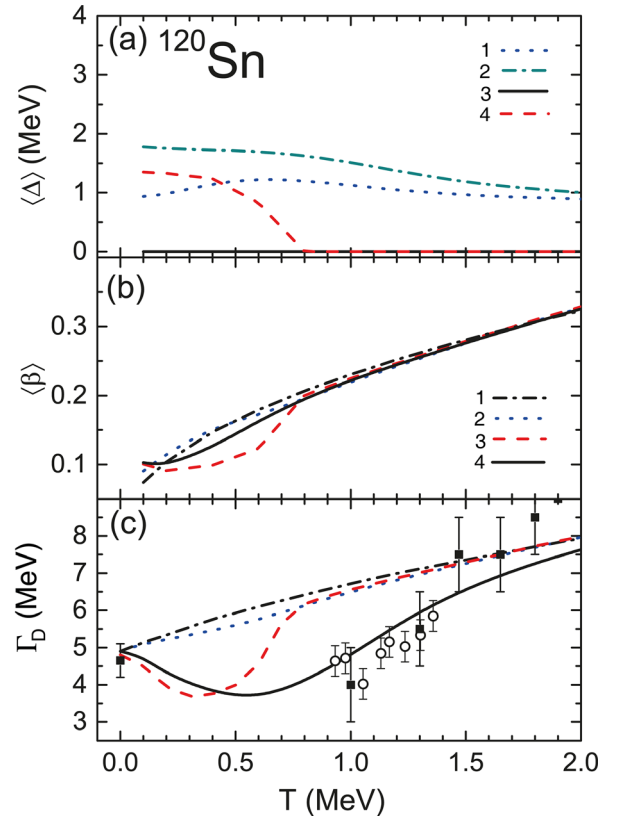


Fig. 18. (Colour online) (a) Average pairing gap, (b) average quadrupole deformation parameter and (c) GDR width as a function of T . In (c), solid squares are experimental widths for ^{120}Sn from refs. [117,147], open circles are those for ^{119}Sb from ref. [185] and calculations are for ^{120}Sn . Calculations without pairing are done within CE. Those with BCS pairing (BCS) and pairing fluctuations (PF) are done within GCE. The legend 1–4 in (a) denotes $\langle \Delta_Z \rangle_{\Delta_Z, \Delta_N, \beta, \gamma}$ (PF), $\langle \Delta_N \rangle_{\Delta_Z, \Delta_N, \beta, \gamma}$ (PF), $\langle \Delta_Z \rangle_{\beta, \gamma}$ (BCS), and $\langle \Delta_N \rangle_{\beta, \gamma}$ (BCS), respectively. The legend 1–4 in (b) stands for LDM, without pairing (CE), BCS (GCE) and PF (GCE), respectively, and is applicable to (c) also. (Adapted from ref. [120].)

$E_X \sim 26$ MeV was ~ 7 MeV which is about 2 MeV more than the GS width. In this case, T for the final state after the GDR γ -ray emission can be estimated to be ~ 0.9 MeV.

The calculations of the GDR width down to low T have been recently reported in ref. [119,120]. These calculations include the pairing field fluctuations in the TSFM, as discussed earlier. The average pairing gaps $\langle \Delta \rangle$, the average quadrupole deformation parameters β and the GDR widths Γ_D obtained within this formalism for ^{120}Sn , ^{97}Tc , and ^{208}Pb are shown in figs. 18–20 [120]. The results clearly show that for open-shell nuclei the inclusion of the pairing fluctuations in the TSFM significantly improves the comparison with experiment at low T . In closed-shell nuclei, such as ^{208}Pb , the effect of pairing fluctuations on the GDR width is negligible and the shell effects play an important role at low T .

Besides the experiments at low T , the results of some experiments at higher T and J [39,190] suggested a dis-

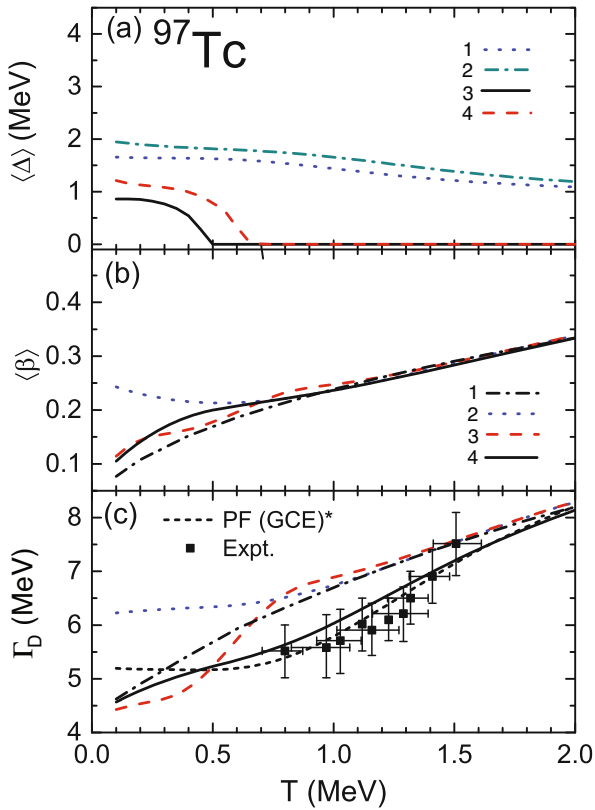


Fig. 19. (Colour online) Similar to fig. 18 but for ^{97}Tc . Solid squares are experimental widths from ref. [187]. PF(GCE)* stands for the results using $\delta = 1.9$ in eq. (5). All other calculations used $\delta = 1.8$. (Adapted from ref. [120].)

crepancy with the TSFM. In an experiment, performed at PLF Mumbai, ^{152}Gd was populated at $E_X = 87$ and 116 MeV in the $^{28}\text{Si} + ^{124}\text{Sn}$ reaction at $E_b = 149$ and 185 MeV, respectively. High-energy γ -ray spectra were measured in coincidence with a 38-element M_γ -array and ERs (at higher E_X). The ERs were detected in an annular PPAC placed in the forward direction. At lower E_X , F-gated spectra above a certain F , for which the non-CN contributions were small, were analysed. Keeping the GDR width the same at each step of decay, the effective widths were extracted for various average $\langle J \rangle$ and $\langle T \rangle$ from the SM analysis using the SMCC code mentioned earlier. Over the range $\langle T \rangle \sim 1.34$ – 1.91 MeV and $\langle J \rangle \sim 13$ – 57 , the extracted widths (using the NLD parameter $a = A/9.5$ MeV $^{-1}$) varied from ~ 8.7 to 10.6 MeV (see footnote¹), as seen in fig. 21. Next, a proposed (T, J) -dependence of the width was incorporated at each step of decay in the SMCC calculation and the F-gated spectra were created. Using the earlier method (keeping the same width at each decay step), the GDR widths for these calculated spectra were derived for each F-window and com-

¹ An error in the calculation of the FWHM of the GDR absorption cross-section from the two-parameter fits to the data has been corrected. The fit parameters of ref. [39] remain unchanged. Figures 21, 22 and the modified Kusnezov parameterisation are therefore different from those in ref. [39].

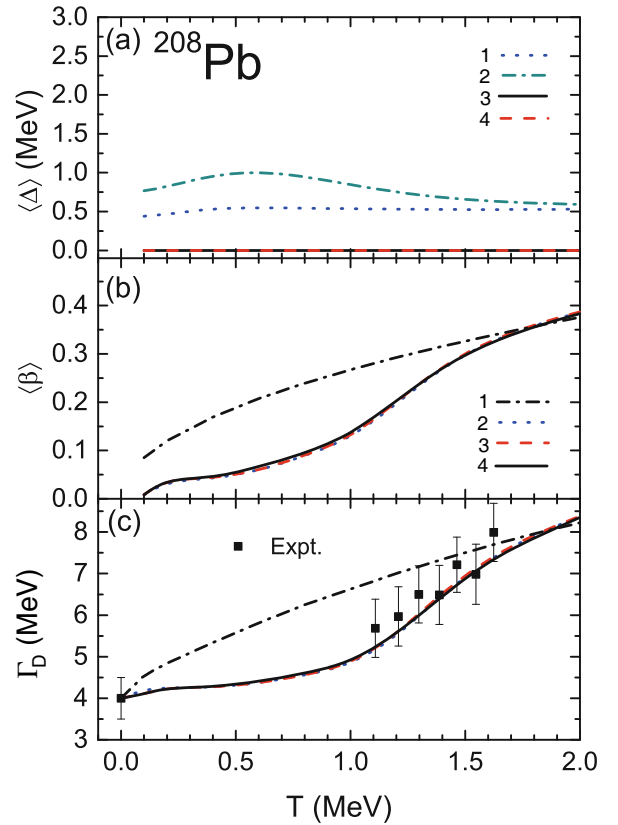


Fig. 20. (Colour online) Similar to fig. 18 but for ^{208}Pb . Solid squares are experimental widths from ref. [117]. (Adapted from ref. [120].)

pared with the experimental effective widths. The Kusnezov parameterisation [117], which is a representation of the TSFM, could not describe the data at both E_X with the same value of Γ_0 (eq. (66)). The parameter Γ_0 represents the width of the GS-GDR and should be independent of E_X . The introduction of an extra T^2 -dependence and a change in the J -dependence in eqs. (66), (67) reproduced the data with the same value of Γ_0 . This is shown in fig. 21 which was obtained with the following modifications. In eq. (66) a term $0.68 T^2$ was added in the expression for $\Gamma_D(J, T = 0, A)$ and the exponent was set to 1. Equation (67) was modified as

$$L(x) = 1 + \frac{1.8}{1 + e^{(1.24-x)/0.2}}, \quad c(A) = 5.0 - A/100.$$

Figure 22 shows the modified parameterisation fitting the data as compared to the Kusnezov parameterisation for two subsets of (T, J) . These observations point towards the effect of both shape fluctuation and collisional damping on the GDR width contrary to the conclusions in some earlier work.

Recently, the TSFM calculation of the GDR width in ^{152}Gd has been reported [191]. The authors, however, misinterpreted the linearised representation of the data as the average absorption cross-section while comparing the calculated and the experimental spectral shapes [192]. The calculated widths were ~ 0.3 MeV higher at the higher E_X

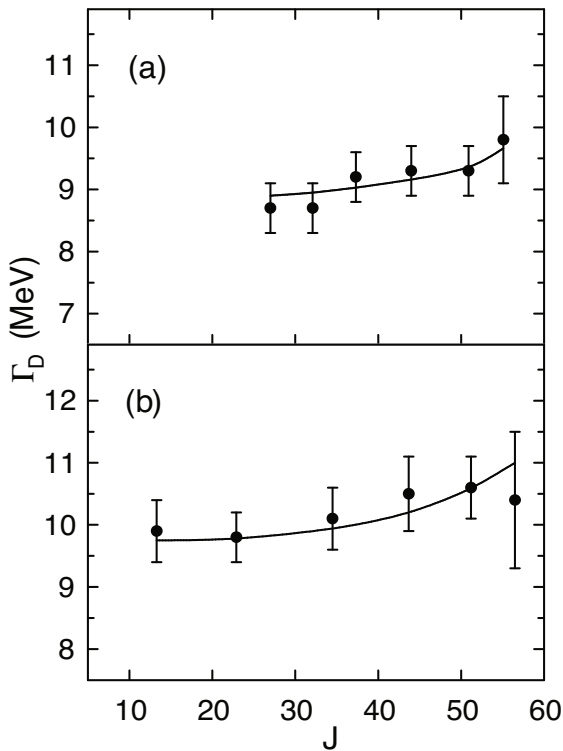


Fig. 21. Experimental GDR width as a function of J (corresponding to different F-windows) at $E_b = 149$ MeV (a) and 185 MeV (b) in the reaction $^{28}\text{Si} + ^{124}\text{Sn}$. Full lines are drawn through the fitted GDR widths using modified Kusnezov parameterisation for the (T, J) -dependence (see text) and $\Gamma_0 = 3.7$ MeV. The figure is different from that in ref. [39] (see footnote ¹).

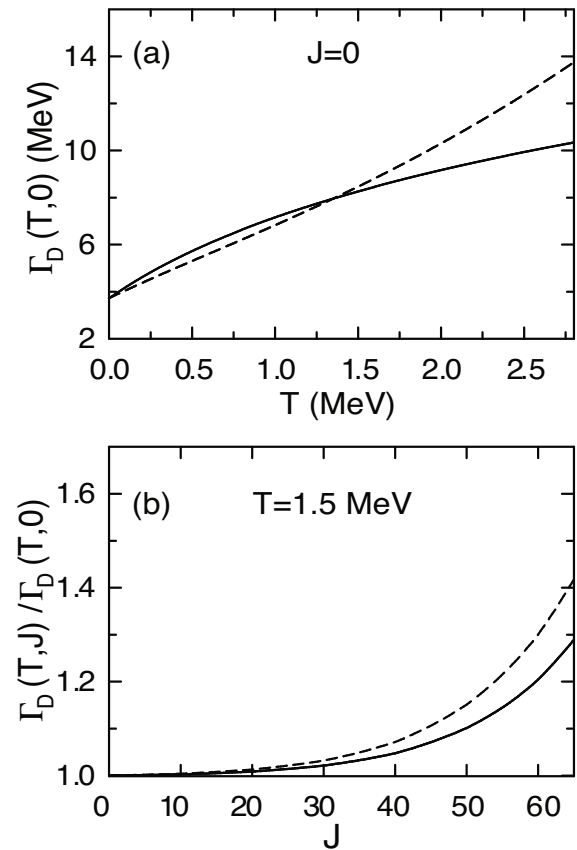


Fig. 22. (a) T -dependence for $J = 0$ and (b) J -dependence for $T = 1.5$ MeV of the GDR width (dashed curves) fitting the data as shown in fig. 21. Continuous curves are pTSMF predictions [117]. The figure is different from that in ref. [39] (see footnote ¹).

contrary to the experimental observation of an increase of > 1 MeV. While this finding also supports an additional T -dependence of the GDR width beyond the TSFM, it may be necessary to do a more elaborate calculation which includes the GDR strength function at various T and J for the nuclei involved in the decay path of the CN, as has been done recently [179].

A discrepancy with the TSFM was seen [50, 193] in another experiment, performed at PLF Mumbai, on ^{86}Mo populated at $\langle J \rangle \sim 11$ –31 and $\langle T \rangle \sim 1.1$ –1.6 MeV in the $^{28}\text{Si} + ^{58}\text{Ni}$ reaction. A simplified shape-fluctuation calculation was done by assuming Gaussian distributions in β and γ and calculating the average GDR strength function with the standard procedure using eqs. (4) and (5). The mean and FWHM of the β , γ distributions, E_{D0} and Γ_0 were varied keeping $\delta = 1.8$. The analysis revealed that the value of $\Gamma_0 \sim 6$ MeV, independent of J , could explain the J -gated spectra at $T = 1.25$ –1.31 MeV. However, an increase in Γ_0 from 4 to 8 MeV was needed to explain the T -gated spectra (for $T = 1.1$ to 1.6 MeV) at $J = 21$ –24. This suggested that the shape fluctuation alone could not reproduce the data. The Kusnezov parameterisation described the J -dependence but not the T -dependence. A detailed TSFM calculation, however, was not reported.

4.2.3 Category C

In the liquid-drop regime, a rotating nucleus attains a NC oblate shape. However, at very high rotational frequencies, it is expected to undergo a drastic shape transition, known as the Jacobi transition, from the NC oblate to a very elongated triaxial (almost prolate) shape, rotating around the shortest axis. This was suggested [194] from the study of rotating charged liquid drops (based on a finding in rotating gravitational systems by Jacobi in 1834) and formulated in the semiclassical models [195, 196]. The critical angular momentum J_{cr} for the transition, which goes up with A as $A^{5/6}$, is higher than the fission limit in heavy nuclei. The study of the Jacobi transition is thus possible in light and medium-mass nuclei.

Whereas the Jacobi transition is manifested in the liquid-drop regime, the superdeformed (SD) shapes are seen in the near-yrast region and are decided by the shell effects. The population of the SD shapes in a nuclear reaction is an open problem. The enhanced γ -ray transition with $E_\gamma \sim 8$ –10 MeV, from the GDR built on SD states, could be one important mechanism. A study of the GDR related to the SD shapes can address this issue.

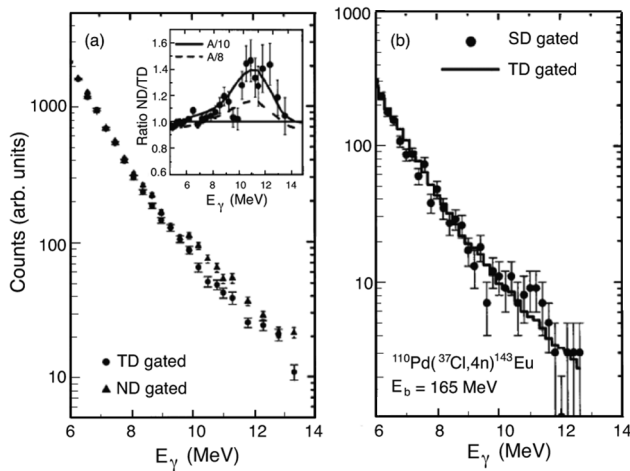


Fig. 23. Left panel: high-energy γ -ray spectra in coincidence with low-energy γ -rays from ND and TD bands in ^{143}Eu . The inset shows the ratio of the two spectra. Solid and dashed lines show the SM calculations with different and same NLD parameters, respectively, for the normal and superdeformed configurations (see text). Right panel: comparison of the spectra measured in coincidence with SD-band and TD-band γ -rays. (Adapted from ref. [197].)

In one exclusive measurement [197], performed in Legnaro, on the GDR built on the SD shapes, ^{147}Eu was populated in the reaction $^{37}\text{Cl} + ^{110}\text{Pd}$ at $E_X = 79$ MeV with $J_{max} > 62$. High-energy γ -ray spectra were measured in the HECTOR array in coincidence with the γ -rays emitted by ERs and detected in the EUROBALL. The residue ^{143}Eu was populated with the highest cross-section at this E_X . This nucleus shows both spherical (ND) and triaxially-deformed (TD) bands at low spin and becomes superdeformed at high spin. The SD yrast band and the excited SD states in the continuum finally populate the ND states only. A comparison of the high-energy γ -ray spectra in coincidence with γ -rays from the ND and TD bands should, therefore, show the evidence for the GDR built on the SD states. Besides, a coincidence with the γ -rays from the SD band itself can address the issue directly (although with much lesser statistics).

The left panel of fig. 23 shows the high-energy γ -ray spectra (normalised at 5 MeV) measured in coincidence with γ -rays from the ND and TD bands. The shapes of the spectra are different in the region $E_\gamma = 8$ –12 MeV. This is further exemplified by their ratio shown in the inset. The excess yield, in coincidence with the ND-band γ -rays, is consistent with the emission from the lower energy component of the GDR in a deformed shape with $\beta \sim 0.6$. In the right panel of the figure, high-energy γ -ray spectra in coincidence with the SD-band and the TD-band γ -rays are compared. The comparison suggests an excess yield in the similar E_γ -region. These results are consistent with the decay of the GDR built on the SD states. The calculated ratio of the γ -ray spectra agreed with the data as shown in the inset. In this calculation, 40% of the population at $J = 40$ –55 and $U < 15$ MeV, where U is the excitation energy above the yrast line, was assumed to

have a SD shape. The energies of the GDR components for the SD shape were taken as 10.5 and 17 MeV. The calculation, done with different NLD parameters for the normal ($a = A/8 \text{ MeV}^{-1}$) and the SD ($a = A/12 \text{ MeV}^{-1}$) shapes, agreed with the data. This observation showed that the superdeformed shape is populated in a nucleus only within ~ 10 –15 MeV above the yrast line. This is in contrast to the Jacobi transition at high E_X discussed in the following.

As mentioned earlier, the first evidence of the Jacobi transition was seen in ^{45}Sc [135]. The search for the high-energy GDR component at ~ 25 MeV, which is a signature of the Jacobi shape, was made in ^{46}Ti [198]. The nucleus was populated at $E_X = 81$ MeV in the reaction $^{18}\text{O} + ^{28}\text{Si}$ in an experiment at NBI Copenhagen. High-energy γ -rays were measured with the HECTOR array in coincidence with a 38-element M_γ -detector array. The SM analysis of the F-gated spectra was made with a two-component GDR. The high-energy component at ~ 24 MeV was found to be stronger at higher F-windows corresponding to higher values of J . This conclusion is similar to that from the singles measurements on ^{45}Sc done at various beam energies. The angular distribution for the highest F-window ($F = 9$ –11) showed the expected behaviour of a change in a_2 coefficient from negative to positive values with the increase in E_γ . This F-window corresponded to $J \sim 25$ –33 extending beyond J_{cr} . The average temperature was $\langle T \rangle \sim 1.3$ MeV.

For a highly deformed nucleus, one expects a very low-energy GDR component corresponding to the vibration along the longest axis. Moreover, the Coriolis splitting [161], expected in triaxial and prolate nuclei, should further split the strength, spreading it down to a still lower energy. In the experimental studies discussed so far, the low-energy component was not reported. The observation of such a component at $E_\gamma \sim 10$ MeV was first reported in ^{46}Ti in an exclusive experiment [199–201] done at the Strasbourg VIVITRON accelerator. The nucleus was populated at $E_X = 86$ MeV in the reaction $^{18}\text{O} + ^{28}\text{Si}$ with $J_{max} = 34$. High-energy γ -ray spectra were measured in the HECTOR array in coincidence with a 83-element M_γ -detector array and the characteristic γ -rays from the ERs detected in the EUROBALL array. The spectrum, gated with $F = 11$ –20 and with a simultaneous selection of characteristic γ -rays from ^{42}Ca , corresponded to a very high J -range extending beyond J_{cr} . The SM analysis was done using the Monte Carlo CASCADE program incorporating a 3-component GDR. The best fit to the spectrum (fig. 24) showed a narrow low-energy component at $E_\gamma \sim 10$ MeV. The TSFM calculation was done using the LSD model for the PES, which predicted the Jacobi transition at $J \sim 28$. The calculations done for $J = 28$ –34 and $T = 2$ MeV, including the Coriolis splitting, showed a good agreement with the experimental spectrum (for $E_\gamma > 10$ MeV) as shown in fig. 25. (The same figure shows the data, discussed earlier, and the calculation for ^{216}Rn . In this case, the LSD model does not predict the Jacobi transition in accordance with the experiment.)

Another interesting observation from these experiments [201] pertained to the population of a highly de-

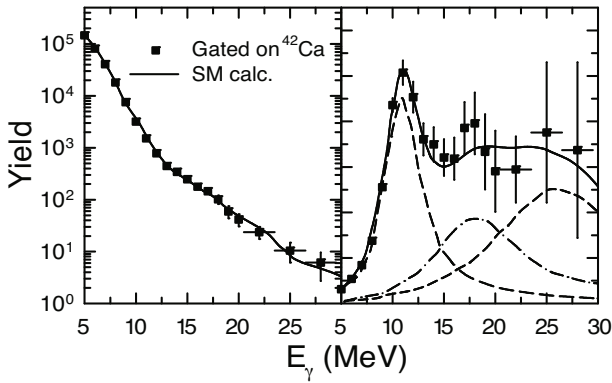


Fig. 24. Left panel: experimental γ -ray spectrum from ^{46}Ti in coincidence with high F-window and discrete transition in ^{42}Ca . The solid line shows the SM fit. Right panel: linearised plots of the data and SM fit (solid line). The dashed lines show the different GDR components in the fit. (Adapted from refs. [199, 200].)

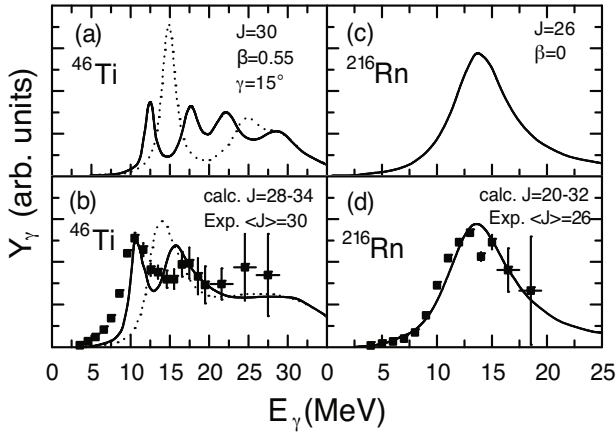


Fig. 25. Experimental GDR strength functions in ^{46}Ti (b) (the same as in right panel of fig. 24) and ^{216}Rn (d). Solid and dotted lines show TSMF calculations (using the LSD model for the PES) with and without Coriolis splitting, respectively. Panels (a) and (c) are calculations at a given J . Panels (b) and (d) are for a range of J corresponding to the experiment. (Adapted from ref. [114].)

formed (HD) band (akin to SD shape) in ^{42}Ca in coincidence with the high-energy γ -rays. The HD band was seen to be preferentially populated in coincidence with the low-energy component of the GDR at ~ 10 MeV. This suggested that in these light nuclei, the population of the HD band might be assisted by the Jacobi transition.

The evidence for the Jacobi transition was seen in ^{47}V in an experiment by the VECC group [202] populating the nucleus at $E_X = 108$ MeV in the reaction $^{20}\text{Ne} + ^{27}\text{Al}$. In ^{47}V , $J_{cr} \sim 29$ and the populated J_{max} was ~ 38 . High-energy γ -rays were measured in coincidence with a M_γ -detector array. Spectra measured for two F-gates, corresponding to $\langle J \rangle \sim 28$ and 31 , showed a narrow structure at $E_\gamma \sim 10$ MeV in the linearised plots. The TSMF calculation was done based on the rotating liquid-drop model, which shows the evolution towards the Jacobi transition

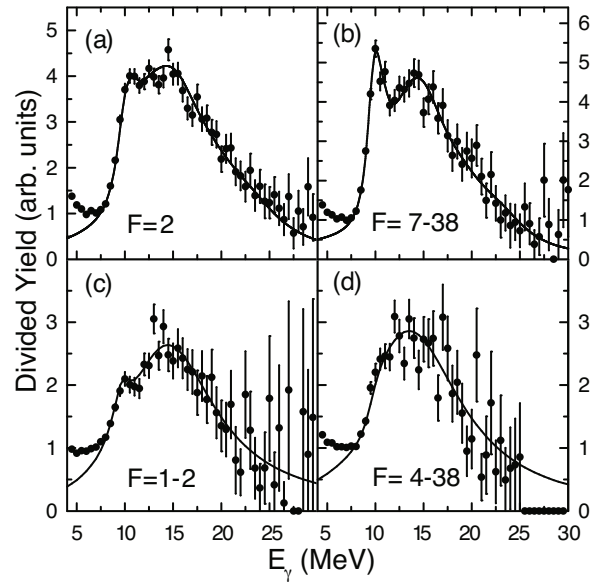


Fig. 26. Linearised plots of various F-gated γ -ray spectra and SM fits at $E_b = 125$ MeV ((a), (b)) and 75 MeV ((c), (d)) in the $^{19}\text{F} + ^{27}\text{Al}$ reaction populating ^{46}Ti . (Adapted from ref. [203].)

at high J , and including the Coriolis effect. The experimental spectra were reproduced above $E_\gamma \sim 8$ MeV.

Further investigations on the Jacobi transition in ^{46}Ti were carried out in an experiment at PLF Mumbai [203] using the reaction $^{19}\text{F} + ^{27}\text{Al}$ at $E_b = 75$ and 125 MeV. The nucleus was populated, respectively, at $E_X = 68$ and 98 MeV and $J_{max} \sim 27$ and 36 . Considering the expected $J_{cr} \sim 28$, the experiment thus addressed both the presence (at high E_X) and the absence (at low E_X) of the transition. High-energy γ -ray spectra were measured in coincidence with ERs detected in an annular PPAC and a 38-element M_γ -detector array. Linearised plots of the measured spectra at $E_X = 98$ MeV (for $F = 2$ and $7-38$) and at $E_X = 68$ MeV (for $F = 1-2$ and $4-38$) are shown in fig. 26. The figure shows a narrow low-energy component in the spectrum at $E_\gamma \sim 10$ MeV at the higher F-window and higher E_X . This is weak at the lower F-window and is absent in the spectra at lower E_X . (A discernible weak peak at the lower F-window was attributed to a different unexplained origin). For the SM calculations, the J_{CN} -distributions corresponding to different F-windows were obtained from the Monte Carlo calculations. From the SM analysis of the spectra, done with the calculated J_{CN} -distributions, the effective photoabsorption cross-sections $\sigma_{abs}(E_\gamma)$ were extracted. As expected, the low-energy component in the extracted σ_{abs} was prominent at the higher E_X and the higher F-window. The values of J_{CN} corresponding to different F-windows straddled a wide range (as expected for light systems). The calculation showed that at higher E_X , the fractional population of J_{CN} above the expected J_{cr} was $\sim 22\%$ and 40% , respectively, for the lower and the upper F-windows. These values were $\sim 4\%$ and 8% at the lower E_X . These observations thus provided further evidence for the Jacobi transition for $J > J_{cr}$.

4.3 Statistical GDR at high T

The study of the GDR at $T \sim 2.5$ to 5 MeV addresses two important issues, *viz.*, the saturation of the GDR width and the quenching of the collective vibration. The experiments in this regime are in general more involved because the ICF process and the PEQ particle emission become very important. The characterisation of the equilibrated source emitting the GDR photons is not straightforward. On the other hand, by selecting different regions of the incomplete momentum transfer, the study of the GDR over a wide range of E_X , albeit with changing A , can be made at one beam energy.

4.3.1 Saturation of GDR width

The first evidence of the saturation of the GDR width was seen in an experiment [148], performed in Grenoble, on ^{110}Sn populated in the $^{40}\text{Ar} + ^{70}\text{Ge}$ reaction at $E_b = 10$ MeV/nucleon. High-energy γ -ray spectra were measured in coincidence with the heavy residues. The velocity spectrum of the residues was compatible with the complete fusion process and $E_X = 230$ MeV. The extracted GDR width of ~ 13 MeV was not very different from ~ 11 MeV at $E_X = 130$ MeV [31] implying a trend towards width saturation. According to the TSFM, in the low E_X region, GDR width increases due to the J -driven deformation and the T -driven fluctuations. At high bombarding energies, there is a limit in the populated J due to the fission process. The J -driven effect should, therefore, saturate beyond this limiting J and the width should further increase only due to the T -driven effect.

In an experiment [204] on the deep inelastic reaction $^{136}\text{Xe} + ^{48}\text{Ti}$ at $E_b = 18.5$ MeV/nucleon, performed in Darmstadt, high-energy γ -rays were detected in coincidence with the target- and projectile-like products having different kinetic energies. The contribution to the spectrum in the GDR region was dominated by that from the excited Xe-like fragments. The extracted GDR widths varied between ~ 9.0 and 10.0 MeV for $E_X/A \sim 1.1$ –2.3 MeV, thus, implying the width saturation.

In another experiment [205] on the reaction $^{16}\text{O} + ^{118}\text{Sn}$ at $E_b = 200$ and 280 MeV, performed at KVI Groningen, ^{134}Ce was populated at an effective $E_X = 165$ and 235 MeV, respectively. High-energy γ -ray spectra were created in coincidence with a segmented sum-spectrometer selecting the central collision events. The extracted GDR widths were ~ 10.5 and 11.0 MeV at these two values of E_X showing the width saturation.

The saturation of the GDR width was discussed in an experiment [41], done in Saclay, on the $^{19}\text{F} + ^{93}\text{Nb}$ reaction at $E_b = 157$ and 184 MeV, corresponding to $E_X = 130$ and 152 MeV, respectively, in ^{112}Sn . High-energy γ -rays were measured in coincidence with heavy residues. In the SM calculations, a T -dependent [34] NLD parameter was used which made a significant difference as compared to those using a T -independent NLD parameter. The analysis was done with various prescriptions [42, 206, 207] for the T -dependent GDR width in-

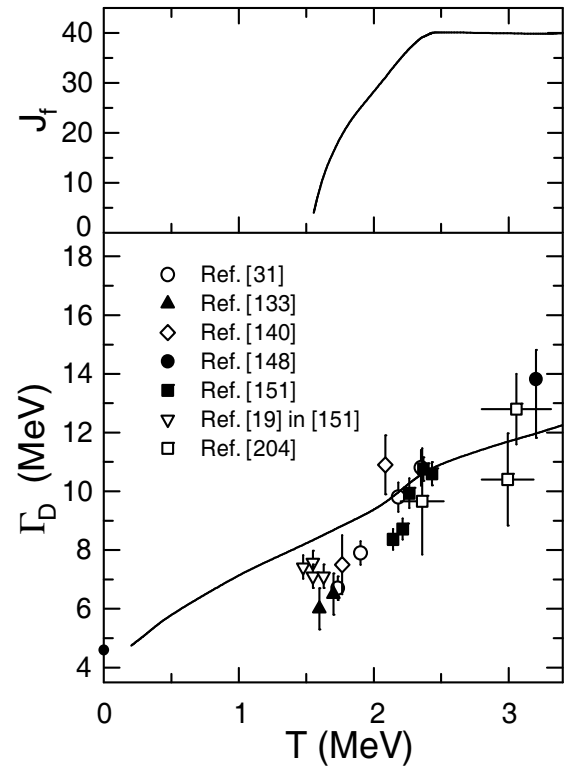


Fig. 27. Lower panel: reanalysed GDR widths as a function of revised T [151] using data from various experiments in Sn and nearby nuclei with $A \sim 110$ –130. The full line shows the TSFM calculation. Upper panel: average J_f of the final states for GDR decay in $^{18}\text{O} + ^{100}\text{Mo}$ reaction. (Adapted from ref. [151].)

cluded at various decay steps in the SM calculation. The probability of γ -ray emission at various steps was multiplied by a reduction factor due to the competition between the GDR equilibration time and the CN lifetime (see later). The result of the analysis was not very conclusive and showed that the data could be reproduced with or without the saturation in the width provided it reaches a large value of 15–20 MeV above $E_X = 100$ MeV. This is higher than the saturation value of ~ 13 MeV suggested in an earlier experiment mentioned above.

The saturation of the width was questioned in a paper [151] reporting an experiment on the $^{18}\text{O} + ^{100}\text{Mo}$ reaction at various E_b . The analysis of the experimental data, mentioned in an earlier section, was made taking into account the effect of PEQ particle emission. This effect, as discussed above, reduces the E_X of the equilibrated source [152] emitting the GDR γ -rays. The effect of the PEQ particle emission was considered in the analysis of the other experimental data, mentioned in this subsection. The correction to the E_X due to the PEQ effect was obtained using a linear fit through two data points and applied to all other cases. The reanalysis of the data revealed a continuous increase of the width up to $T \sim 3.2$ MeV (fig. 27) without any saturation. The TSFM calculation also showed an increase with T (although the reproduction of the experimental data was not good at lower T) even after the saturation in J due to the fission

process. This showed that the T -dependent fluctuation effect is comparable to the J -dependent effect. (It should be mentioned that the data points of ref. [205] were not included in fig. 27.)

We leave the topic of width saturation at this stage after mentioning again the latest experimental result [179] on ^{88}Mo at $T = 2.0$ and 3.1 MeV. The work suggested a saturation (figs. 13 and 14) of the GDR width, thus, reopening the debate on this issue.

4.3.2 Quenching of GDR

The experiments at very high E_X or T (> 3 MeV) address the evolution and persistence of the collective motion in very hot nuclei. The topic of GDR quenching has been reviewed in detail in a recent paper [17].

The first demonstration of the quenching of the GDR at high T came from an experiment [208] on the reaction $^{40}\text{Ar} + ^{70}\text{Ge}$ at $E_b = 15$ and 24 MeV/nucleon done in Grenoble. High-energy γ -ray spectra were measured in coincidence with the reaction products. Although the maximum values of E_X transferred to the compound system were 360 and 610 MeV, the SM analysis of the spectra, after including the bremsstrahlung component, reproduced the data in the GDR region assuming a lesser $E_X = 320$ MeV at both beam energies. In the calculations, the GDR width was fixed at 15 MeV at all decay steps and the strength was 100% of TRK . This observation suggested that the GDR γ -ray emission is inhibited above $E_X = 320$ MeV. In another work from the same group [209], the same reaction was studied at four beam energies between 10 and 24 MeV/nucleon. The measured γ -ray spectra could be reproduced with $E_X = 300$ MeV and a GDR width of 13 MeV at all E_b . This was attributed to the vanishing of the collective motion at $T \sim 5$ MeV.

A very different interpretation of the vanishing of the GDR was proposed by the RIKEN group [42–44]. The authors analysed the experimental data from the ^{40}Ar -induced reactions, on Ni, ^{92}Mo and ^{122}Sn , done at $E_b = 21$ to 26 MeV/nucleon. High-energy γ -ray spectra were measured gated by different residue velocities. The integrated yield for $E_\gamma = 12$ – 20 MeV in the GDR region (after the bremsstrahlung subtraction) showed a flat behaviour as a function of E_X . This is contrary to the normal expectation of an increase of the yield with E_X , coming from the higher number of steps available for the emission of the GDR γ -rays. In the SM analysis, an E_X -dependent GDR width was used at different decay steps, as opposed to the earlier analyses. The dependence for ^{92}Mo target was ascertained to be $\Gamma_D(E_X) = 4.8 + 0.0015 E_X + 0.0002 E_X^2$. The flat behaviour mentioned above was reasonably reproduced. The authors defined a limiting E_X for the GDR survival at which the width becomes 30 MeV (somewhat arbitrarily). The corresponding limiting temperature was derived as $T \sim 4.5$ MeV for all the targets.

The proposition of the RIKEN group was refuted in an elaborate experiment done in GANIL [210,211] on the reaction $^{36}\text{Ar} + ^{90}\text{Zr}$ at $E_b = 27$ MeV/nucleon. High-energy

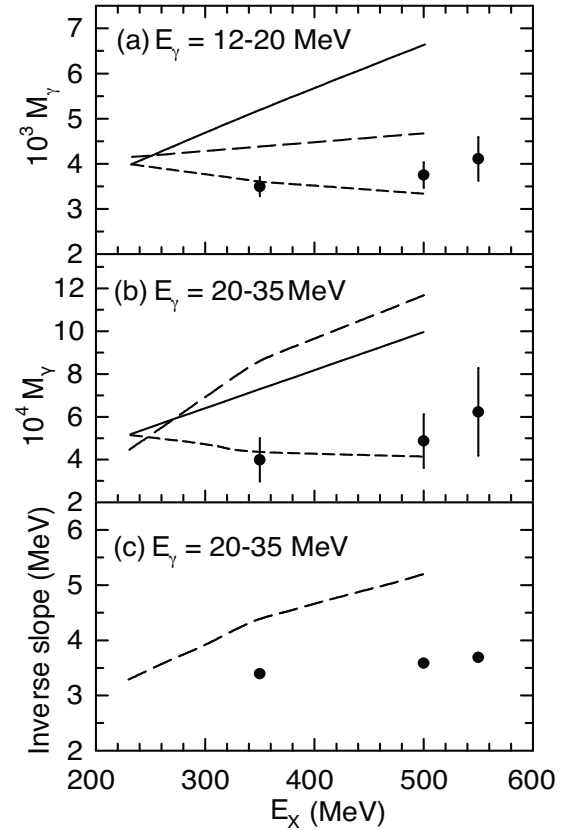


Fig. 28. Experimental and calculated γ -ray multiplicities as a function of E_X , for (a) $E_\gamma = 12$ – 20 MeV and (b) $E_\gamma = 20$ – 35 MeV, in $^{36}\text{Ar} + ^{90}\text{Zr}$ reaction at $E_b = 27$ MeV/nucleon. Solid lines are the results of the standard SM calculation and long-dashed lines are the ones with an assumption of the width increasing with E_X . Short dashed lines are obtained with a cut-off E_X for GDR γ -ray emission. (c) Inverse slope of the measured bremsstrahlung-subtracted spectra for $E_\gamma = 20$ – 35 MeV and the result of the SM calculation with increasing GDR width. (Adapted from ref. [211].)

γ -ray spectra were measured in the MEDEA array in coincidence with three velocity bins of the heavy residues. Coincident proton spectra were also measured in order to characterise the temperature of the emitting source. A detailed analysis deduced the equilibrated E_X for the three velocity bins as 350 , 500 and 550 MeV. The integrated multiplicities for two windows, *viz.*, $E_\gamma = 12$ – 20 (GDR region) and 20 – 35 MeV (above GDR), were created from the bremsstrahlung-subtracted γ -ray spectra. These are shown in fig. 28 where a small change of the γ -ray yield (in the GDR region) is seen with increasing E_X . This is contrary to the standard SM calculations (solid lines) and corroborates the earlier observations on the saturation of the GDR γ -ray yield. However, the small change even for the higher E_γ -window is contrary to the proposition of a continuous increase of the GDR width with E_X , as shown by the long-dashed lines. The behaviour of the inverse slope parameter of the measured spectra (fig. 28(c)) is also not consistent with this proposition.

Various theoretical ideas on the change of the GDR width with E_X and the hindrance of the γ -ray emission due to the competition between the GDR equilibration time and the CN lifetime were tried in the SM calculations. Bortignon *et al.* [212] proposed the reduction in the probability of γ -ray emission, arising from the consideration of the GDR equilibration time, as

$$P(E_\gamma) = \Gamma_0 / (\Gamma_0 + \Gamma_{CN})$$

with the intrinsic width $\Gamma_0 = 4.8$ MeV. An excitation-energy dependent GDR width was used up to $E_X \sim 130$ MeV. At higher E_X , the width was assumed to saturate at 12 MeV. Calculations for $E_X = 500$ MeV compared well with the data at higher E_γ but grossly underestimated the yield below $E_\gamma \sim 15$ MeV. Smerzi *et al.* [98, 213] proposed, from the CDM, a continuous increase of Γ_D with E_X without any saturation. In the above probability factor, Γ_0 was replaced by Γ_D at each E_X . The calculated spectrum reasonably reproduced the data near the GDR energy but overestimated the data at higher E_γ . Chomaz *et al.* [145, 146] proposed an additional contribution of $2\Gamma_{CN}$ to the width, where Γ_{CN} is the evaporation width of the states connecting the GDR γ -ray transition. This leads to an increase in the GDR width with E_X due to the increase in Γ_{CN} . Using this prescription, the prediction was even worse at higher E_γ . All these comparisons showed that the proposition of a continuous increase in GDR width with E_X , which reduces the contribution in the GDR region and enhances the yield at higher E_γ , is contrary to the experimental results.

The simplest way to explain the data was to assume a sharp decrease of the γ -ray yield from the GDR above a certain E_X . Using the same $E_X = 250$ MeV for the three energy bins and a constant $\Gamma_D = 12$ MeV at each decay step, the spectra were well reproduced above $E_\gamma = 12$ MeV (fig. 28(a) and (b)). However, the calculated yield was less than the data for $E_\gamma = 8$ –12 MeV. This suggested some extra strength in this region which could be due to the PEQGDR γ -ray emission (discussed in the next section). This emission takes place from the system with a large deformation and contributes to the spectrum at lower E_γ .

It may be mentioned at this stage that the quenching of the GDR is predicted by the PDM. In a calculation [90] on ^{120}Sn and ^{208}Pb , extended to high T (> 4 MeV), the model predicted the saturation of the GDR width. Using the calculated widths, the trend of the quenching of the GDR γ -rays was reproduced in the $A \sim 120$ region (see fig. 9 in ref. [90]).

The measurements on the GDR quenching were made by the same group [21, 214, 215] at a higher beam energy of $E_b = 37$ MeV/nucleon in the reaction $^{36}\text{Ar} + ^{98}\text{Mo}$. Considering the results from earlier experiments in the similar mass region, it was deduced that in the GDR region ($E_\gamma = 12$ –20 MeV) the γ -ray multiplicity decreases from 5.2×10^{-3} at $E_b = 21$ MeV/nucleon to 2.4×10^{-3} at $E_b = 37$ MeV/nucleon. A calculation of the reaction dynamics, using the Boltzmann-Nordheim-Vlasov (BNV) equation [216], revealed that the time required to form the

final equilibrated nucleus is more at higher E_b . Due to the PEQ particle emissions during this period, the E_X at the final stage gets reduced. The statistical GDR γ -rays, emitted at this stage, thus, has a lower multiplicity at higher E_b supporting the observations. However, as mentioned in ref. [17], the differences in the experimental multiplicities could be attributed, in some measure, to the differences in the experimental setups and methods of data analysis. In the final analysis of the data at 37 MeV/nucleon [21], three velocity bins of the heavy residues were used. After a detailed characterisation through the measurement of particle spectra, the excitation energies for the three bins were deduced as $E_X = 300, 350$ and 430 MeV with $A = 105, 108$ and 111 , respectively. Using a sharp cut-off in E_X for the presence of the GDR vibration, as mentioned above, the cut-off values were deduced as 220, 230 and 220 MeV, respectively, establishing again the vanishing of the GDR at high T .

The quenching of the GDR in a different mass region was studied [217] at LNS Catania using the reactions $^{40}\text{Ca} + ^{48}\text{Ca}$ and $^{40}\text{Ca} + ^{46}\text{Ti}$ at $E_b = 25$ MeV/nucleon. High-energy γ -rays and charged particles were detected in the multi-detector system TRASMA. The SM analysis of the γ -ray spectra was done after characterising the E_X of the source, utilising the earlier experimental results for a similar system, *viz.*, $^{40}\text{Ca} + ^{48}\text{Ti}$ [218]. Interestingly, after taking the reduction factor $R = \Gamma_\downarrow / (\Gamma_\downarrow + \Gamma_{CN})$ in the γ -ray decay probability at each stage (with $\Gamma_\downarrow = 6.5$ MeV), a sharp cut-off in E_X was not needed to explain the data. The authors defined the cut-off energy as the value of E_X at which $R = 1/2$. The deduced values of E_{cutoff}/A were ~ 5.4 and 4.7 MeV for the two reactions with a larger error bar for the second reaction. These values are significantly higher than ~ 2 MeV in the $A \sim 110$ region.

In a recent experiment [21], the study was extended to lower beam energies in the inverse-kinematic reactions $^{116}\text{Sn} + ^{12}\text{C}$ at $E_b = 17$ and 23 MeV/nucleon and $^{116}\text{Sn} + ^{24}\text{Mg}$ at $E_b = 17$ MeV/nucleon. In the earlier experiments, the nuclei were populated at E_X much higher than the E_{cutoff} values. This measurement addressed the gradual vanishing of the GDR vibration as a function of E_X . The experiment was done at LNS Catania using the MEDEA detector array. Fusion-like residues were detected by a solenoid spectrometer. From a detailed analysis of the charged particle spectra and the charge distribution of the residues, the values of E_X were deduced as $\sim 150, 190$ and 270 MeV for the above three cases and the mass numbers of the equilibrated sources were 124, 123 and 132, respectively. With the GDR widths of ~ 11.0 and 12.5 MeV, the experimental spectra were reproduced at the two lower E_X (*i.e.* up to $E_X = 190$ MeV) without any quenching of the GDR. At $E_X = 270$ MeV, the analysis needed a cut-off in E_X for the GDR vibration, as was seen in the earlier works, in order to reproduce the experimental spectrum. The value of E_{cutoff}/A was deduced as ~ 1.7 MeV with $A \sim 132$. This showed that the phenomenon of quenching sets in gradually above a certain E_X .

In order to quantify the gradual vanishing of the GDR with E_X , the experimental and the SM-calculated spectra were integrated between 12 and 20 MeV (in the GDR re-

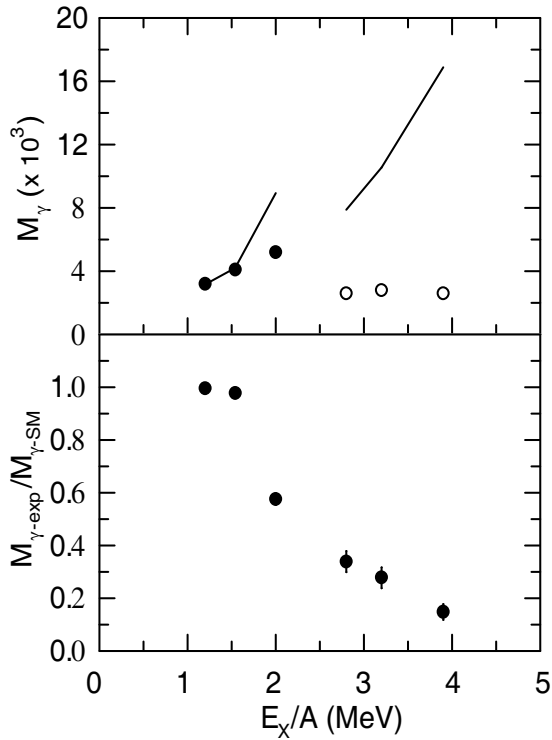


Fig. 29. Upper panel: experimental GDR γ -ray multiplicity ($E_\gamma = 12\text{--}20$ MeV) and SM prediction (continuous lines) for $^{116}\text{Sn} + ^{12}\text{C}$ and $^{116}\text{Sn} + ^{24}\text{Mg}$ reactions at $E_b = 17$ and 23 MeV/nucleon (filled circles) and $^{36}\text{Ar} + ^{98}\text{Mo}$ reaction at higher E_b (open circles). Lower panel: gradual quenching of the GDR with E_X/A shown as the ratio of experimental and SM-calculated γ -ray multiplicities in the upper panel. (Adapted from ref. [21].)

gion). These are shown in fig. 29 as a function of excitation energy per nucleon for different reactions including those at much higher energies. A decrease in the experimental yield, as compared to the calculation, is seen at higher E_X . The lower panel in the figure shows the ratio between the two yields. A smooth decrease of this ratio is observed as a function E_X/A , starting above ~ 1.5 MeV and continuing up to the highest energy, indicating a quenching of the GDR which sets in at ~ 2 MeV per nucleon.

A connection between the vanishing of the GDR vibration and the liquid-to-gas (LG) phase transition has been proposed by many authors. In the experiments on the caloric curve studies, a plot of the deduced T as a function of E_X showed a flat region signifying a mixed phase [219]. The excitation energy at which the flattening starts signals the setting in of the phase transition. A plot of this excitation energy per nucleon as a function of A shows a decrease with A (fig. 30). From the experimental results in different mass regions [21,217], the limiting excitation energies (E_X^{limit}/A) for the existence of the GDR were summarised [21] as ~ 5.0 , 2.1 and 1.7 MeV for $A \sim 60\text{--}70$, 105–111 and 132, respectively. These, thus, also show a decrease with A (fig. 30). A broad similarity in the A -dependence of the limiting excitation energies per nucleon, related to both phenomena, provides an experi-

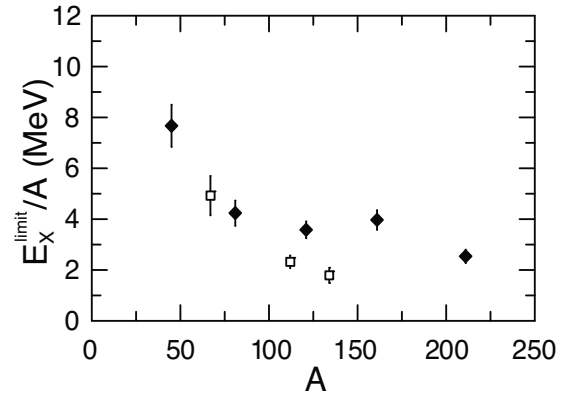


Fig. 30. Excitation energy per nucleon at which the LG phase transition sets in (filled symbols) and the GDR vibration is quenched (open symbols) showing a broad similarity in the A -dependence. (Adapted from ref. [21].)

mental indication [21] of the connection between the GDR quenching and the LG phase transition.

4.4 Specific shear viscosity of hot nuclei from GDR

Recent experiments on ultra-relativistic heavy-ion collisions at the Relativistic Heavy-Ion Collider (RHIC) [220–223] at Brookhaven National Laboratory and the Large Hadron Collider (LHC) [224,225] at CERN have made key discoveries on the creation and study of the quark-gluon plasma (QGP). The analysis of the data revealed that the strongly interacting matter formed in these collisions is a nearly perfect fluid with a very low specific shear viscosity η/s where η is the shear viscosity and s is the entropy volume density. In order to apply hydrodynamics to nuclear systems such as a hot nucleus, the quantum mechanical uncertainty principle requires that it has a finite viscosity. Kovtun, Son and Starinets [226] conjectured that η/s has a universal lower bound of $\hbar/(4\pi k_B) = KSS$, known as the KSS bound or unit, for all fluids.

As mentioned earlier the giant resonance damping, in semiclassical theories, is related to the nuclear viscosity. By evaluating the \mathbf{p} -moments, eq. (46) is reduced to the Navier-Stokes-like equations of motion with the memory-dependent coefficient of shear viscosity $\eta(T)$ [106]. For $T < \epsilon_F$ and $\omega_0 < \epsilon_F$, the shear viscosity is found within the FLDM as [106,227]

$$\eta(T) = \frac{2}{5} \rho \epsilon_F \frac{\bar{\tau}}{1 + (\omega_0 \bar{\tau})^2}, \quad (76)$$

where the notation $\bar{\tau}$ denotes τ_{coll} in eq. (52) at $\zeta = 1$ and at $\bar{\tau}$ given by the parameterisation (eq. (53))

$$\bar{\tau} = \tau_{\text{coll}}(\zeta = 1, \bar{\tau} = \alpha/T^2). \quad (77)$$

Adopting $\epsilon_F = 40$ MeV, $\rho = 0.16 \text{ fm}^{-3}$, $\alpha = 9.2$ MeV and $\omega = 20$ MeV, Auerbach and Shlomo [227] obtained $\eta/s \simeq 4\text{--}19$ and 2.5–12.5 KSS for heavy and light nuclei, respectively. The shortcomings of these results are

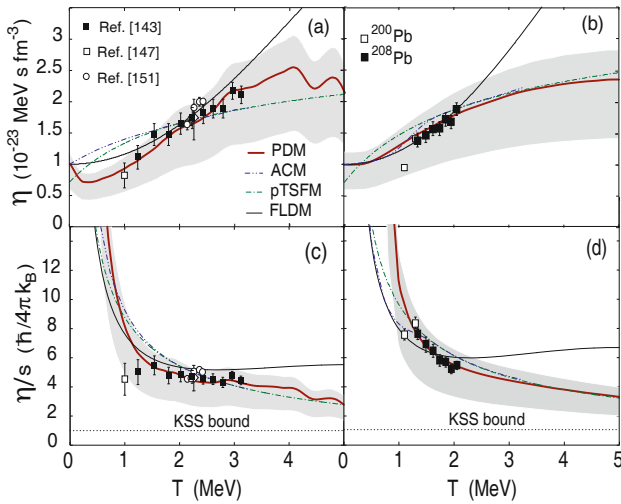


Fig. 31. Empirical (points) and calculated (lines) shear viscosity η and specific shear viscosity η/s as a function of T for nuclei in the Sn region ((a) and (c)) and Pb isotopes ((b) and (d)) using various models and $\eta(0)=1u$. Gray areas are PDM predictions using $0.6u \leq \eta(0) \leq 1.2u$. Experimental data for GDR widths in the Sn region are from the references shown and for Pb isotopes, from ref. [20].

the large uncertainty and the use of the Fermi-gas entropy $S = 2aT$ in estimating the specific shear viscosity.

A better estimation of η/s was proposed in ref. [228] where the Green-Kubo's relation was used to derive the T -dependence of η in terms of the GDR parameters as

$$\eta(T) = \eta(0) \frac{\Gamma_D(T)}{\Gamma_D(0)} \frac{E_D(0)^2 + [\Gamma_D(0)/2]^2}{E_D(T)^2 + [\Gamma_D(T)/2]^2}. \quad (78)$$

This expression and the microscopic entropy can be used to calculate η/s using the GDR widths and energies with $\eta(0)$ as a parameter. The value of $\eta(0)$ is between $0.6u$ and $1.2u$ where $u = 10^{-23} \text{ MeV s fm}^{-3}$, as discussed in refs. [12, 229].

The predictions of η and η/s as a function of T by using the PDM, pTSFM, ACM and FLDM, for ^{120}Sn and ^{208}Pb , are shown in fig. 31. The figure also shows the empirical results derived from the experimental GDR parameters [20]. It is seen from the figure that the PDM provides the best overall agreement with the empirical results. The ratio η/s decreases sharply with T up to $\sim 1.5 \text{ MeV}$ and more gradually at higher T to reach $\sim 2\text{--}3 \text{ KSS}$ at $T = 5 \text{ MeV}$. In the same work [228], a model-independent estimate was made assuming the maximal value of the GDR width $\Gamma_{max} \simeq 3\Gamma_D(0) \simeq 0.9E_D(0)$ and $E_D(T) = E_D(0)$. This gives $\eta_{max} \simeq 2.55 \times \eta(0)$. The high- T limit of the entropy density was obtained as $s_{max} \simeq 0.22 k_B$. The derived minimum value of the specific shear viscosity was $(\eta/s)_{min} \simeq 2.2_{-0.9}^{+0.4} \text{ KSS}$ using $\eta(0) = 1.0_{-0.4}^{+0.2} u$. Based on this model-independent assessment as well as the results from various models discussed above, one can conclude that for medium-mass and heavy nuclei $\eta/s \sim 1.3\text{--}4.0 \text{ KSS}$ at $T = 5 \text{ MeV}$. This is about 3–5 times smaller (and of lesser uncertainty) than 4–19 KSS

predicted by the FLDM [227] for heavy nuclei (derived using $\eta(0) = 0.6 u$). These discussions indicate that the specific shear viscosity in hot nuclei at $T = 5 \text{ MeV}$ is expected to have nearly the same value as that of the QGP ($1.5\text{--}2.5 \text{ KSS}$) at $T > 170 \text{ MeV}$.

4.5 Pre-equilibrium GDR

The discussion so far has been on the statistical GDR excited in an equilibrated nucleus. However, before the equilibration, a direct mechanism of the GDR excitation is possible. This arises due to a large-amplitude dipole oscillation, termed as the pre-equilibrium GDR (PEQGDR), induced in the charge-asymmetric reaction channels with different N/Z ratio of the projectile and the target. In the first stage of the collision, nuclei move towards the N/Z equilibration inducing the PEQGDR. Since this mode is excited before equilibration, when the nuclear system is very deformed, the GDR energy is lower than that of the equilibrated system. Experimentally, the PEQGDR has been studied by measuring high-energy γ -ray spectra in fusion reactions and deep inelastic collisions (DIC).

The first indication of the PEQGDR was seen [230] in the reactions $^{35}\text{Cl} + ^{64}\text{Ni}$ and $^{35}\text{Cl} + ^{92}\text{Mo}$ at $E_b = 271$ and 260 MeV , respectively, studied in Saclay. High-energy γ -ray spectra were measured in coincidence with the outgoing fragments. From a comparison of the experimental and calculated γ -ray spectra emitted from the excited fragments, an excess yield was observed at $E_\gamma \sim 10\text{--}11 \text{ MeV}$. This was attributed to the GDR γ -ray emission at a highly deformed pre-equilibrium stage. In a similar experiment [231] on the reaction $^{32}\text{S} + ^{74}\text{Ge}$ at $E_b = 320 \text{ MeV}$, performed in Legnaro, the measured γ -ray spectrum in coincidence with the reaction products revealed an excess yield at $E_\gamma \sim 10\text{--}15 \text{ MeV}$ when compared with the SM calculations. This was consistent with the emission from a touching configuration of the projectile and the target. The analysis of the measured fragment- γ -ray angular correlation also showed a pre-equilibrium component at a similar energy.

In an experiment [232], performed in Legnaro, a comparative study was made between the reactions $^{32}\text{S} + ^{64}\text{Ni}$ and $^{32}\text{S} + ^{58}\text{Ni}$. The magnitude of the difference ($\delta_{N/Z}$) between the N/Z of the projectile and the target are ~ 0.28 and 0.07 , respectively, for the two reactions. High-energy γ -ray spectra were measured in coincidence with the reaction products. The spectra created in coincidence with the quasi-elastic (QE) events were similar for the two reactions whereas those in coincidence with the DIC events showed a difference. In the latter case, there was an excess yield at $E_\gamma \sim 10\text{--}18 \text{ MeV}$ in the reaction channel with a larger $\delta_{N/Z}$. This observation provided a strong evidence for the PEQGDR. Its absence in the QE reaction was attributed to the fact that the reaction time was too small to relax the charge degrees of freedom.

The first fusion reaction experiment showing the excitation of the PEQGDR [233] was performed in Chalk River. High-energy γ -rays were measured using the 8π -spectrometer [234] in the $^{36}\text{S} + ^{104}\text{Pd}$ and $^{40}\text{Ca} + ^{100}\text{Mo}$

reactions (with $\delta_{N/Z} = 0.01$ and 0.38 , respectively) populating ^{144}Sm at $E_X = 71$ MeV. An enhanced yield of $\sim 16\%$, seen for $E_\gamma \sim 8\text{--}18$ MeV in the second reaction, was attributed to the PEQGDR γ -rays. A Boltzmann-Uehling-Uhlenbeck (BUU) [235] calculation showed consistency with the experimental findings.

A series of experiments was reported [236–238] on a systematic study of the energy dependence of the PEQGDR excitation considering the theoretical predictions of a rise and fall of its excitation probability as a function of E_b [239,240]. The pairs of reactions, leading to the similar composite systems, studied were (a) $^{32}\text{S} + ^{100}\text{Mo}$ and $^{36}\text{S} + ^{96}\text{Mo}$ at $E_b = 6$ and 9 MeV/nucleon and (b) $^{40}\text{Ar} + ^{92}\text{Zr}$ and $^{36}\text{Ar} + ^{96}\text{Zr}$ at $E_b = 15\text{--}16$ MeV/nucleon. The mass asymmetry, defined in terms of the radii as $(R_P - R_T)/(R_P + R_T)$ where P and T refer to the projectile and the target, respectively, were almost the same in both pairs. This eliminated the possible mass-asymmetry-dependent effects in the reactions [241].

The first pair of reactions (with $\delta_{N/Z} \sim 0.38$ and 0.04 , respectively) was studied in Legnaro. High-energy γ -ray spectra were measured at various angles, including 90° , in coincidence with the fusion-like residues. The contribution from the bremsstrahlung process was subtracted in the data analysis. The reduction in E_X due to the PEQ particle emission was calculated with the existing systematics [151]. The effective values of E_X were 117 and 173.5 MeV, for both reactions, at the lower and the higher E_b , respectively. The comparisons of the spectra measured in the two reactions are shown in fig. 32. At the lower E_b , the spectra in both reactions were identical and could be described by a SM calculation with the GDR energy of 14.3 MeV. The excess yield in the more charge-asymmetric channel was thus consistent with zero. At the higher E_b , the spectra showed a large difference. For the reaction channel with $\delta_{N/Z} \sim 0.04$, the SM calculation explained the data with the GDR energy of ~ 14 MeV. In the other reaction with $\delta_{N/Z} \sim 0.38$, there was an excess yield of $\sim 25\%$ at $E_\gamma = 8\text{--}21$ MeV at $\theta = 90^\circ$. These observations established that the PEQGDR emission depends on the beam energy or the reaction time.

The dependence on the reaction time was supported by a different observation in another experiment [242] on the reaction pair $^{16}\text{O} + ^{98}\text{Mo}$ and $^{48}\text{Ti} + ^{64}\text{Ni}$. These have $\delta_{N/Z} \sim 0.33$ and 0.10 , respectively. Although the difference in $\delta_{N/Z}$ is less here, an excess yield of $\sim 36\%$ was seen in the first reaction in a similar E_γ -range. In this case, ($E_X \sim 110$ MeV in the CN) the beam energy is even less than 9 MeV/nucleon. However, the reaction pair has a large mass-asymmetry difference and the first reaction, with more mass asymmetry, has a faster reaction time to produce the CN. This showed that the excitation of the PEQGDR depends on the reaction time. This, in turn, agrees with the finding that for a given mass asymmetry, the excess yield goes up at higher E_b .

The second pair of reactions (with $\delta_{N/Z} \sim 0.08$ and 0.40 , respectively) was studied at LNS Catania. High-energy γ -ray spectra were measured with the MEDEA array in coincidence with fusion-like residues. Proton and

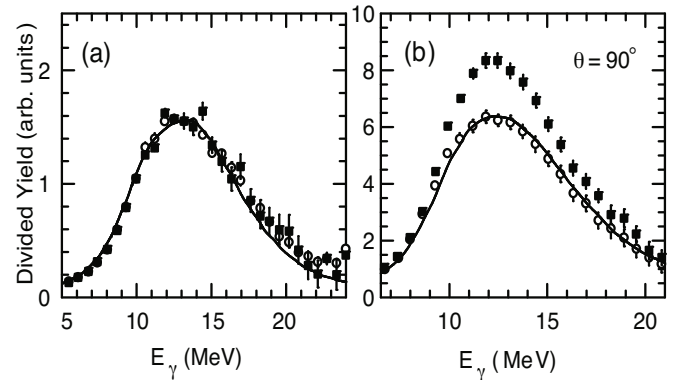


Fig. 32. Linearised plots of γ -ray spectra in $^{32}\text{S} + ^{100}\text{Mo}$ and $^{36}\text{S} + ^{96}\text{Mo}$ reactions at (a) $E_b \sim 6$ MeV/nucleon and (b) $E_b \sim 9$ MeV/nucleon. Data shown as solid squares and open circles are for the first and second reaction, respectively. Continuous lines show SM fits. (Adapted from [236,237].)

α -particle spectra were measured in order to characterise the effective E_X and A of the source. These were deduced, in both channels, as $E_X \sim 285$ MeV and $A \sim 126$, respectively. For the more charge-symmetric reaction, the bremsstrahlung-subtracted spectrum was fitted with the SM calculations. (However, the fit could be obtained by using a lower $E_X = 250$ MeV, which implies the quenching of the statistical GDR as discussed earlier). A comparison of the bremsstrahlung-subtracted spectra showed an increase in yield in the more charge-asymmetric channel. In this case, the integrated yield for $E_\gamma \sim 8\text{--}21$ MeV showed only a 12% increase at $\theta = 90^\circ$. This is lower than that measured at $E_b = 9$ MeV/nucleon and, hence, shows a rise and fall of the PEQGDR excitation with beam energy.

The difference spectra between the charge-asymmetric and charge-symmetric reactions, measured at $E_b = 9$ and 16 MeV/nucleon, were fitted with Lorentzian shapes. The extracted GDR energies (widths) were ~ 11.4 (3.0) MeV and 12.2 (3.7) MeV, respectively. The energies are lower than the CN-GDR energies of ~ 14 MeV implying a deformed source for the PEQGDR γ -rays. The analysis of the measured angular distribution of γ -rays provided more information. For the charge-symmetric reaction, the a_2 values for different E_γ -bins were consistent with the statistical GDR γ -ray emission from a non-collective oblate nucleus. On the other hand, the angular dependence of the difference in the yields between the two channels (for $E_\gamma \sim 9\text{--}21$ MeV) showed a prominent anisotropy consistent with $a_2 = -1$. This implied that the GDR γ -ray emission takes place from a system oscillating along the beam direction, as is expected for the PEQGDR.

For a quantitative understanding, the BNV calculation was done at $E_b = 6, 9$ and 16 MeV/nucleon. The calculations revealed, as mentioned earlier, that a faster reaction time is conducive to the PEQGDR excitation. However, at a high beam energy ($15\text{--}20$ MeV/nucleon), the γ -ray emission gets hindered by a faster damping of the mode and the faster particle emissions. These calculations, which depend on the NN collision cross-section σ_{NN} and the nuclear density ρ , showed an agreement with the data at $E_b = 6$

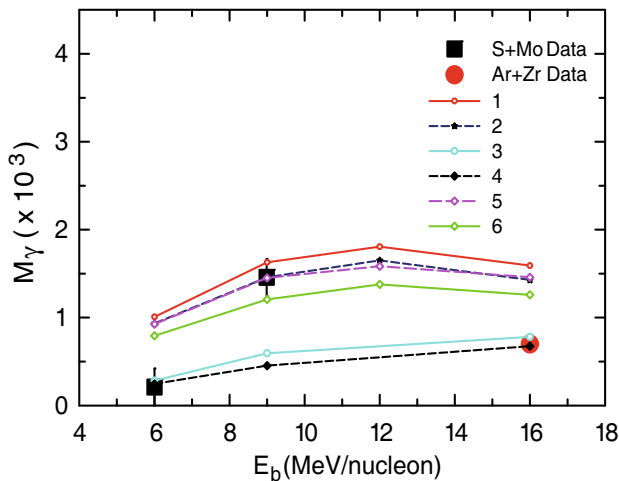


Fig. 33. Multiplicity of PEQGDR γ -rays at various beam energies in Ar + Zr and S + Mo reactions and results of BNV calculations elaborated in ref. [238]. Lines 1,3,5 refer to the first reaction and 2,4,6 to the second. Lines 1,2 are obtained with asymmetric soft equation of state and 5,6, with asymmetric stiff equation of state, both sets using nuclear density $\rho = 0.14 \text{ fm}^{-3}$. Lines 3,4 are obtained using free NN cross-sections. (Adapted from ref. [238].)

and 16 MeV/nucleon. The data at $E_b = 9 \text{ MeV/nucleon}$ could, however, be reproduced with a lower in-medium σ_{NN} and a constant $\rho = 0.14 \text{ fm}^{-3}$ (fig. 33). The authors concluded that this aspect should be further investigated both experimentally and theoretically in future.

The PEQGDR was observed at a much higher beam energy [217] of $E_b = 25 \text{ MeV/nucleon}$ in the reaction pair $^{40}\text{Ca} + ^{48}\text{Ca}$ and $^{40}\text{Ca} + ^{46}\text{Ti}$. The experiment was discussed in an earlier section. The ratios of the γ -ray yields, in coincidence with heavy residues, from the two reactions were created at various angles. An enhancement in the yield for the more charge-asymmetric channel, as expected for the PEQGDR excitation, was seen in a broad E_γ region around 10 MeV. The γ -ray spectra at all angles were added after applying the Doppler correction assuming the source velocity to be that of the fusion-like residues. The ratio of the angle-summed spectra for the two reactions also showed an enhancement at $E_\gamma \sim 10 \text{ MeV}$ indicating that the PEQGDR γ -rays are emitted from a source with velocity of the fusion-like residues.

5 Summary and outlook

In this review we have discussed the developments and the present status in the field of the damping of the GDR in hot and rotating nuclei. The research work in the field of the PEQGDR has been briefly addressed.

The measurement of the GDR width, which arises due to the damping, as a function of temperature and angular momentum requires the use of exclusive experimental techniques which have progressed considerably over the years. This has been matched by the progress in the theoretical understanding as well.

Experimental observations on the T - and J -dependence of the GDR width covering a wide range of T , J and nuclear systems, can be broadly summarised as follows. The GDR width is rather insensitive to the change of T up to $\sim 1 \text{ MeV}$ and increases rapidly up to a moderate T of $\sim 2.5 \text{ MeV}$. At higher T , there are claims of observing the saturation of the GDR width. This observation has, however, been questioned in some works which have emphasised the need for a better characterisation of the E_X and T of the source. A reanalysis of the data, after taking into account the pre-equilibrium effects in the mass-asymmetric channel, has shown a monotonic increase of the width at least up to $T \sim 3.2 \text{ MeV}$. On the other hand, a recent experiment in a mass-symmetric channel, which shows negligible PEQ effects, has suggested the saturation of the GDR width at $T \sim 3 \text{ MeV}$. This highlights the need to resolve this important issue in future experiments. At still higher temperatures, there are observations pointing to the quenching of the GDR strength. In this regime again, various authors use a saturated GDR width in the data analysis. The GDR quenching has been related to the competition between the equilibration time for the excitation of the GDR and the lifetime of the nucleus or the transition of the hot nucleus to a chaotic regime. In this regard, an interesting suggestion has been made on the connection between the vanishing of the collective vibration and the liquid-to-gas phase transition in nuclear systems.

The disentangling of the effects of J and T on the GDR width has been made mostly in the moderate T -regime. The GDR width depends weakly on J at low J -values and increases more rapidly beyond a certain J . This value of J depends on the nuclear mass number, being, for example, ~ 30 for $A \sim 110$. In heavier nuclei ($A \sim 180$) the width is roughly constant up to the highest measured $J \sim 50$. An interesting aspect of the GDR at high angular momentum in certain systems is the Jacobi transition which leads to a highly deformed shape beyond a certain critical J . Measurements in $A \sim 40\text{--}60$ systems have shown strong evidence of such a transition. There are also indications of the GDR built on the superdeformed shapes in ^{143}Eu .

Among the several theoretical approaches to calculating the GDR strength function in hot and rotating nuclei, the TSFM has been most widely employed in the comparison with the experimental data. The J -dependence of the width is explained reasonably well by the model. Here, the contribution to the width at low J comes from the thermal shape fluctuations. On the other hand, the J -driven shape changes and the consequent width increase become important at high J . The T -dependence of the width is not very well reproduced by this model, particularly at low T . An improvement in this model, by including pairing fluctuations, is able to describe the GDR width at low T . Due to the fluctuations, the pairing correlations do not vanish abruptly but decrease monotonically with T . At higher T , the inclusion of the additional CN-decay width seems to be enough to explain some data while other experiments point to the need of an additional T -dependent contribution which could arise from the collisional damping. The macroscopic model CDM predicts a monotonic

increase of the width with T but does not address the J -dependence. The experimental data at high T do not agree with the CDM predictions. At medium T its predictions reasonably agree with the experimental data provided the free NN scattering cross-sections are used rather than the more appropriate in-medium cross-sections.

The microscopic models, which go beyond the FT-RPA, have shown that the GDR (quantal) spreading width Γ^\downarrow , which arises from the coupling to $2p2h$ configurations, is almost independent of T . Among the various microscopic models, the PDM is the most successful one. The results of the PDM calculations including pairing fluctuations agree with the T -dependence of the experimental widths at low and moderate T . The model also predicts the saturation of the width as well as the quenching of the GDR γ -ray yield at very high T .

An interesting offshoot of the GDR studies is the extraction of the T -dependence of specific shear viscosity η/s of a hot nuclear system using the corresponding GDR parameters. If η/s is extrapolated to $T \sim 5$ MeV it roughly matches with that for a very different system, *viz.*, the QGP at $T > 170$ MeV. The values are not far from the KSS lower bound.

Although considerable progress has been made in both theory and experiment in this field, more efforts are needed for a detailed understanding of the GDR in highly excited nuclei. In the regime of moderate T and high J , different procedures are often employed by different groups in the data analysis and in the evaluation of the average values of T and J for comparing with the theory. This leads to varied opinions on the success of a particular model. Ideally, the comparison should be made between the experimental γ -ray cross-sections and the statistical model calculations in which the theoretical (E_X, J)-dependent GDR strength function is used at various steps of decay. The next best choice would be to use the theoretical (T, J)-dependent strength function. A uniform prescription of the NLD employed in various experiments is very important. Keeping these aspects in mind, more systematic measurements are necessary for establishing the success or failure of various models. One particular example could be to establish whether or not the (T, J)-dependence of the GDR width needs the inclusion of additional contributions, besides those from the shape fluctuation and the CN-lifetime effects. Another systematic measurement would be on the dependence on the N/Z ratio of the CN. An extension of these measurements will be carried out in future experiments with exotic beams addressing the pygmy dipole resonance in hot neutron-rich nuclei.

More systematic measurements at low T are needed to confirm that the GDR width remains at almost the GS value up to a certain T . Any controversial observation (for example in ^{114}Sn) in this regard should be revisited. Measurements should also be made at low T and high J because in this case the pairing-fluctuation effect, which seems to explain the low- T behaviour at low J , should be negligible.

Highly deformed shapes (Jacobi or superdeformed) have been seen or suggested only in a few cases using the GDR measurements. These interesting phenomena need

to be established in more systems. A particularly important issue in this area is the mechanism of population of these shapes and their survival in the decay chain of an excited compound nucleus.

In the high- T regime, the important point of the proper characterisation of the nuclear systems should be addressed critically in the analysis of the γ -ray spectra. This needs additional measurements of particle spectra, as has been done in some experiments. The saturation of the GDR width needs to be addressed with more experiments considering the present controversial claims. This is particularly important because of the different predictions of the various models on this issue. The connection of the LG phase transition with the quenching of the collective vibration at high T was suggested by some authors. This important issue needs more systematic measurements to validate the assertion.

The experimental study of the PEQGDR has progressed over the years establishing this phenomenon in different systems. The comparison with the theoretical predictions is generally satisfactory but needs more work for a full understanding of the phenomenon. The PE-QGDR γ -ray emission could have important consequences in the production of superheavy elements in heavy-ion reactions. As has been pointed out by some authors, this phenomenon provides a fast cooling process in the fusion path. This will be particularly relevant in future experiments with exotic beams.

One of the authors (DRC) acknowledges the financial support from the Department of Science and Technology, Government of India. Many theoretical results in this review were obtained by using the RIKEN HOKUSAI-Great Wave computer system. M. Ciemala and A.K. Rhine Kumar are thanked for providing some of the postscript figure files.

References

1. A. Bohr, B.R. Mottelson, *Nuclear Structure*, Vols. **I** (W.A. Benjamin, New York, 1969) and **II** (W.A. Benjamin, 1975).
2. D.M. Brink, Oxford Doctoral Thesis (1955) unpublished.
3. P. Axel, *Phys. Rev.* **126**, 671 (1962).
4. R.G. Allas, S.S. Hanna, L. Meyer-Schutzmeister, R. Segel, *Nucl. Phys.* **58**, 122 (1964).
5. F.S. Dietrich, J.C. Browne, W.J. O'Connell, M.J. Kay, *Phys. Rev. C* **10**, 795 (1974).
6. J.O. Newton, B. Herskind, R.M. Diamond, E.L. Dines, J.E. Draper, K.H. Lindenberg, C. Schuck, S. Shih, F.S. Stephens, *Phys. Rev. Lett.* **46**, 1383 (1981).
7. M.N. Harakeh, A. van der Woude, *Giant Resonances: Fundamental High-Frequency Modes of Nuclear Excitation* (Oxford Science Publications, Oxford, 2001).
8. A. Vlasov, *J. Phys. (USSR)* **9**, 25 (1945).
9. L.D. Landau, *Zh. Eksp. Teor. Fiz.* **30**, 1058 (1956) (*Sov. Phys. JETP* **3**, 920 (1957)).
10. L.D. Landau, *Zh. Eksp. Teor. Fiz.* **32**, 59 (1957) (*Sov. Phys. JETP* **5**, 101 (1957)).
11. C. Fiolhais, *Ann. Phys.* **171**, 186 (1986).
12. N. Auerbach, A. Yeverechyahu, *Ann. Phys. (N.Y.)* **95**, 35 (1975).

13. P.F. Bortignon, A. Bracco, R.A. Broglia, *Giant Resonances: Nuclear Structure at Finite Temperature* (Harwood Academic Publishers, Amsterdam, 1998).
14. K.A. Snover, *Annu. Rev. Nucl. Part. Sci.* **36**, 545 (1986).
15. J.J. Gaardhøje, *Annu. Rev. Nucl. Part. Sci.* **42**, 483 (1992).
16. P. Paul, M. Thoennessen, *Annu. Rev. Nucl. Part. Sci.* **44**, 65 (1994).
17. D. Santonocito, Y. Blumenfeld, *Eur. Phys. J. A* **30**, 183 (2006).
18. J.L. Egido, P. Ring, *J. Phys. G* **19**, 1 (1993).
19. H. Hofmann, *The Physics of Warm Nuclei and of Mesoscopic Systems* (Oxford University Press, London, 2005).
20. A. Schiller, M. Thoennessen, *At. Data Nucl. Data Tables* **93**, 549 (2007).
21. D. Santonocito *et al.*, *Phys. Rev. C* **90**, 054603 (2014).
22. A. Maj, J.J. Gaardhøje, A. Atac, S. Mitarai, J. Nyberg, A. Virtanen, *Nucl. Phys. A* **571**, 185 (1994).
23. E. Migneco *et al.*, *Nucl. Instrum. Methods A* **314**, 31 (1992).
24. S. Mukhopadhyay *et al.*, *Nucl. Instrum. Methods A* **582**, 603 (2007).
25. W.R. Nelson, H. Hirayama, D.W.O. Rogers, Stanford University Report SLAC **265** (1985).
26. GEANT4 Collaboration (S. Agostinelli *et al.*), *Nucl. Instrum. Methods A* **506**, 250 (2003).
27. A. Musumarra, G. Cardella, A. Di Pietro, S.L. Li, M. Papa, G. Pappalardo, F. Rizzo, S. Tudisco, *Nucl. Instrum. Methods A* **370**, 558 (1996).
28. G. Sletten, *Proceedings of the International Seminar on Frontiers of Nuclear Spectroscopy, Kyoto 1992* (World Scientific, Singapore, 1993) p. 129.
29. D. Bazzacco, *Proceedings of the International Conference on Nuclear Structure at High Angular Momentum, Ottawa, 1992*, Vol. **2**, Proc. AECL-10613.
30. G. de Angelis, A. Bracco, D. Curien, *Europhys. News* **34**, 181 (2003).
31. D.R. Chakrabarty, S. Sen, M. Thoennessen, N. Alamanos, P. Paul, J.J. Gaardhøje, *Phys. Rev. C* **36**, 1886 (1987).
32. A. V. Ignatyuk, G.N. Smirenkin, A.S. Tishin, *Yad. Fiz.* **21**, 485 (1975) (*Sov. J. Nucl. Phys.* **21**, 255 (1975)).
33. W. Reisdorf, *Z. Phys. A* **300**, 227 (1981).
34. W. E. Ormand, P.F. Bortignon, A. Bracco, R.A. Broglia, *Phys. Rev. C* **40**, 1510 (1989).
35. S. Shlomo, J.B. Natowitz, *Phys. Rev. C* **44**, 2878 (1991).
36. R.J. Charity, *Phys. Rev. C* **82**, 014610 (2010).
37. F. Pühlhofer, *Nucl. Phys. A* **280**, 267 (1977).
38. J.H. Gundlach, K.A. Snover, C.A. Gossett, M. Kicińska-Habior, K.T. Lesko, *Phys. Rev. Lett.* **65**, 2523 (1990).
39. D.R. Chakrabarty, V.M. Datar, Suresh Kumar, E.T. Mirgule, A. Mitra, V. Nanal, R.G. Pillay, P.C. Rout, *J. Phys. G* **37**, 055105 (2010).
40. G. Gervais, M. Thoennessen, W.E. Ormand, *Phys. Rev. C* **58**, R1377 (1998).
41. D. Pierroutsakou, F. Auger, N. Alamanos, P.R.S. Gomes, J.L. Sida, A. Gillibert, N. Frascaria, I. Lhenry, J.C. Roynette, T. Suomijarvi, *Nucl. Phys. A* **600**, 131 (1996).
42. K. Yoshida, J. Kasagi, H. Hama, M. Sakurai, M. Kodama, K. Farutaka, K. Ieki, W. Galster, T. Kubo, M. Ishihara, *Phys. Lett. B* **245**, 7 (1990).
43. J. Kasagi *et al.*, *Nucl. Phys. A* **538**, 585 (1992).
44. J. Kasagi, K. Yoshida, *Nucl. Phys. A* **569**, 195 (1994).
45. P. Carlos, R. Bergere, H. Beil, A. Lepretre, A. Veysiere, *Nucl. Phys. A* **219**, 61 (1974).
46. A.R. Junghans, G. Rusev, R. Schwengner, A. Wagner, E. Groose, *Phys. Lett. B* **670**, 200 (2008).
47. Deepak Pandit, S. Mukhopadhyay, Srijit Bhattacharya, Surajit Pal, A. De, S.R. Banerjee, *Nucl. Instrum. Methods A* **624**, 148 (2010).
48. M. Mattiuzzi, A. Bracco, F. Camera, W.E. Ormand, J.J. Gaardhøje, A. Maj, B. Million, M. Pignanelli, T. Tveter, *Nucl. Phys. A* **612**, 262 (1997).
49. M. Thoennessen, E. Ramakrishnan, J.R. Beene, F.E. Bertrand, M.L. Halbert, D.J. Horen, P.E. Mueller, R.L. Varner, *Phys. Rev. C* **51**, 3148 (1995).
50. S.K. Rathi, D.R. Chakrabarty, V.M. Datar, S. Kumar, E.T. Mirgule, A. Mitra, V. Nanal, H.H. Oza, *Phys. Rev. C* **67**, 024603 (2003).
51. D.R. Chakrabarty, *Nucl. Instrum. Methods A* **560**, 546 (2006).
52. D.N. Zubarev, *Sov. Uspekhi* **3**, 320 (1960) (*Usp. Fiz. Nauk.* **71**, 71 (1960)).
53. A.V. Ignatyuk, *Izv. Acad. Nauk, Ser. Fiz.* **38**, 2613 (1974).
54. A.V. Ignatyuk, *Sov. J. Nucl. Phys.* **21**, 10 (1975).
55. M.I. Baznat, A.V. Ignatyuk, N.I. Pyatov, *Sov. J. Nucl. Phys.* **30**, 493 (1979).
56. H.M. Sommermann, *Ann. Phys. (N.Y.)* **151**, 163 (1983).
57. D. Vautherin, N. Vinh Mau, *Phys. Lett. B* **50**, 162 (1983).
58. D. Vautherin, N. Vinh Mau, *Nucl. Phys. A* **422**, 140 (1984).
59. H. Sagawa, G.F. Bertsch, *Phys. Lett. B* **146**, 138 (1984).
60. P. Ring, L.M. Robledo, J.L. Egido, M. Faber, *Nucl. Phys. A* **419**, 261 (1984).
61. N. Dinh Dang, *J. Phys. G* **11**, L125 (1985).
62. N. Dinh Dang, N. Zuy Thang, *J. Phys. G* **14**, 1471 (1988).
63. L.G. Moretto, *Phys. Lett. B* **40**, 1 (1972).
64. A.L. Goodman, *Nucl. Phys. A* **352**, 30 (1981).
65. A.L. Goodman, *Phys. Rev. C* **29**, 1887 (1984).
66. R. Rossignoli, P. Ring, N.D. Dang, *Phys. Lett. B* **297**, 9 (1992).
67. N.D. Dang, P. Ring, R. Rossignoli, *Phys. Rev. C* **47**, 606 (1993).
68. V. Zelevinsky, B.A. Brown, N. Frazier, M. Horoi, *Phys. Rep.* **276**, 85 (1996).
69. D.J. Dean, S.E. Koonin, K. Langanke, P.B. Radha, Y. Alhassid, *Phys. Rev. Lett.* **74**, 2909 (1995).
70. N. Quang Hung, N. Dinh Dang, *Phys. Rev. C* **79**, 054328 (2009).
71. N.D. Dang, A. Arima, *Phys. Rev. C* **68**, 014318 (2003).
72. N. Dinh Dang, V. Zelevinsky, *Phys. Rev. C* **64**, 064319 (2001).
73. N. Dinh Dang, A. Arima, *Phys. Rev. C* **67**, 014304 (2003).
74. N. Dinh Dang, *Nucl. Phys. A* **784**, 147 (2007).
75. N. Dinh Dang, N. Quang Hung, *Phys. Rev. C* **77**, 064315 (2008).
76. B. Lauritzen, P. Arve, G.F. Bertsch, *Phys. Rev. Lett.* **61**, 2835 (1988).
77. A. Volya, B.A. Brown, V. Zelevinsky, *Phys. Lett. B* **509**, 37 (2001).
78. N. Dinh Dang, N. Quang Hung, *Phys. Rev. C* **86**, 044333 (2012).
79. V.G. Soloviev, *Theory of Atomic Nuclei: Quasiparticle and Phonons* (IOP, Bristol, 1992).
80. N. Dinh Dang, *Nucl. Phys. A* **504**, 143 (1989).

81. I. Hamamoto, Nucl. Phys. A **126**, 545 (1969).
82. G.F. Bertsch, P.F. Bortignon, R.A. Broglia, C.H. Dasso, Phys. Lett. B **80**, 161 (1979).
83. P.F. Bortignon, R.A. Broglia, Nucl. Phys. A **371**, 405 (1981).
84. S.P. Kamerdhiev, G.Ya. Tertychny, V.I. Tselyaev, Russ. J. Phys. Elem. Part. At. Nucl. **28**, 334 (1997).
85. P.F. Bortignon, R.A. Broglia, G.F. Bertsch, J. Pacheco, Nucl. Phys. A **460**, 149 (1986).
86. N. Dinh Dang, A. Arima, Phys. Rev. Lett. **80**, 4145 (1998).
87. N.D. Dang, A. Arima, Nucl. Phys. A **636**, 427 (1998).
88. N. Dinh Dang, K. Tanabe, A. Arima, Phys. Rev. C **58**, 3374 (1998).
89. N. Dinh Dang, K. Tanabe, A. Arima, Phys. Lett. B **445**, 1 (1998).
90. N. Dinh Dang, K. Tanabe, A. Arima, Nucl. Phys. A **645**, 536 (1999).
91. N. Dinh Dang, A. Arima, Phys. Rev. C **68**, 044303 (2003).
92. N. Dinh Dang, Phys. Rev. C **85**, 064323 (2012).
93. M. Brack, P. Quentin, Phys. Lett. B **52**, 159 (1974).
94. P. Bonche, S. Levit, D. Vautherin, Nucl. Phys. A **436**, 265 (1985).
95. N. Dinh Dang, M. Ciemala, M. Kmiecik, A. Maj, Phys. Rev. C **87**, 054313 (2013).
96. Cai Yanhuang, M. Di Toro, Phys. Rev. C **39**, 105 (1989).
97. G.F. Burgio, M. Di Toro, Nucl. Phys. A **476**, 189 (1988).
98. A. Smerzi, A. Bonasera, M. Di Toro, Phys. Rev. C **44**, 1713 (1991).
99. M. Di Toro, V.M. Kolomietz, A.B. Larionov, Phys. Rev. C **59**, 3099 (1999).
100. J. Blocki, Y. Boneh, J.R. Nix, J. Randrup, M. Robel, A.J. Sierk, W.J. Swiatucki, Ann. Phys. **113**, 330 (1978).
101. A.A. Abrikosov, I.M. Khalatnikov, Rep. Prog. Phys. **22**, 329 (1959).
102. D. Pines, P. Nozieres, *The Theory of Quantum Liquids*, Vol. 1 (W.A. Benjamin, New York, 1966).
103. J.J. Griffin, M. Dworzecka, Phys. Lett. B **156**, 39 (1985).
104. C. Yannouleas, Nucl. Phys. A **439**, 336 (1985).
105. C. Yannouleas, R.A. Broglia, Ann. Phys. (N.Y.) **217**, 105 (1992).
106. V.M. Kolomietz, S. Shlomo, Phys. Rep. **390**, 133 (2004).
107. V.M. Kolomietz, V.A. Plujko, S. Shlomo, Phys. Rev. C **52**, 2480 (1995).
108. Y. Alhassid, B. Bush, S. Levit, Phys. Rev. Lett. **61**, 1926 (1988).
109. W.E. Ormand, P.F. Bortignon, R.A. Broglia, A. Bracco, Nucl. Phys. A **614**, 217 (1997).
110. Y. Alhassid, B. Bush, Nucl. Phys. A **549**, 12 (1992).
111. Y. Alhassid, Nucl. Phys. A **649**, 107 (1999).
112. K. Pomorski, J. Dudek, Phys. Rev. C **67**, 044316 (2003).
113. J. Dudek, K. Pomorski, N. Schunck, N. Dubray, Eur. Phys. J. A **20**, 15 (2004).
114. N. Dubray, J. Dudek, A. Maj, Acta Phys. Pol. B **36**, 1161 (2005).
115. J. Dudek, Phys. Rev. C **23**, 920 (1981).
116. J. Dudek *et al.*, Phys. Rev. C **26**, 1712 (1982).
117. D. Kusnezov, Y. Alhassid, K.A. Snover, Phys. Rev. Lett. **81**, 542 (1998) and references therein.
118. A. Schiller, M. Thoennessen, K.M. McAlpine, Nucl. Phys. A **788**, 231 (2007).
119. A.K. Rhine Kumar, P. Arumugam, N. Dinh Dang, Phys. Rev. C **90**, 044308 (2014).
120. A.K. Rhine Kumar, P. Arumugam, N. Dinh Dang, Phys. Rev. C **91**, 044305 (2015).
121. A. Ansari, N. Dinh Dang, A. Arima, Phys. Rev. C **63**, 024310 (2001).
122. P. Arumugam, G. Shanmugam, S.K. Patra, Phys. Rev. C **69**, 054313 (2004).
123. P. Arumugam, A. Ganga Deb, S.K. Patra, Eur. Phys. Lett. **70**, 313 (2005).
124. A. Ansari, N. Dinh Dang, A. Arima, Phys. Rev. C **62**, 011302(R) (2000).
125. B.K. Agrawal, A. Ansari, P. Ring, Nucl. Phys. A **165**, 183 (1997).
126. J.A. Draper, J.O. Newton, L.G. Sobotka, H. Lindenberg, G.J. Wozniak, L.G. Moretto, F.S. Stephens, R.M. Diamond, R.J. McDonald, Phys. Rev. Lett. **49**, 434 (1982).
127. W. Hennerici *et al.*, Nucl. Phys. A **396**, 329 (1983).
128. B. Haas, D.C. Radford, F.A. Beck, T. Byrski, C. Gehringer, J.C. Merdinger, A. Nourredine, Y. Schutz, J.P. Vivien, Phys. Lett. B **120**, 79 (1983).
129. J.J. Gaardhøje, O. Andersen, R.M. Diamond, C. Ellegaard, L. Grodzins, B. Herskind, Z. Sujkowski, P.M. Walker, Phys. Lett. B **139**, 273 (1984).
130. A. Lazzarini, H. Habs, W. Hennerici, R. Kroth, J. Schirmer, V. Metag, Phys. Rev. Lett. **53**, 1045 (1984).
131. Th. Arctadius, Chr. Bargholtz, R.E. Ekstrom, K. Fransson, B. Ritzen, P.E. Tegner, Phys. Lett. B **158**, 205 (1985).
132. E.F. Garman, K.A. Snover, S.H. Chew, S.K.B. Hesmondhalgh, W.N. Catford, P.M. Walker, Phys. Rev. C **28**, 2554 (1983).
133. J.J. Gaardhøje, C. Ellegaard, B. Herskind, S.G. Steadman, Phys. Rev. Lett. **53**, 148 (1984).
134. C.A. Gossett, K.A. Snover, J.A. Behr, G. Feldman, J.L. Osborne, Phys. Rev. Lett. **54**, 1486 (1985).
135. M. Kicińska-Habior, K.A. Snover, J.A. Behr, C.A. Gossett, Y. Alhassid, N. Whelan, Phys. Lett. B **308**, 225 (1993).
136. M. Kicińska-Habior, K.A. Snover, C.A. Gossett, J.A. Behr, G. Feldman, H.K. Glatzel, J.H. Gundlach, Phys. Rev. C **36**, 612 (1987).
137. Z.M. Drebi, K.A. Snover, A.W. Charlop, M.S. Kaplan, D.P. Wells, D. Ye, Y. Alhassid, Phys. Rev. C **52**, 578 (1995).
138. G. Viesti *et al.*, Phys. Rev. C **40**, R1570 (1989).
139. M. Kicińska-Habior, K.A. Snover, J.A. Behr, C.A. Gossett, J.H. Gundlach, G. Feldman, Phys. Rev. C **45**, 569 (1992).
140. J.J. Gaardhøje, C. Ellegaard, B. Herskind, R.M. Diamond, M.A. Deleplanque, G. Dines, A.O. Macchiavelli, F.S. Stephens, Phys. Rev. Lett. **56**, 1783 (1986).
141. A. Bracco, F. Camera, M. Mattiuzzi, B. Million, M. Pignanelli, J.J. Gaardhøje, A. Maj, T. Ramsøy, T. Tveter, Z. Zelazny, Phys. Rev. Lett. **74**, 3748 (1995).
142. E. Ramakrishnan *et al.*, Phys. Rev. Lett. **76**, 2015 (1996).
143. T. Baumann *et al.*, Nucl. Phys. A **635**, 428 (1998) and references therein.
144. G. Viesti *et al.*, Nucl. Phys. A **652**, 17 (1999).
145. Ph. Chomaz, Nucl. Phys. A **569**, 203 (1994).
146. Ph. Chomaz, Phys. Lett. B **347**, 1 (1995).
147. P. Heckman *et al.*, Phys. Lett. B **555**, 43 (2003).
148. A. Bracco *et al.*, Phys. Rev. Lett. **62**, 2080 (1989).

149. J.J. Gaardhøje, A.M. Bruce, B. Herskind, Nucl. Phys. A **482**, 121 (1988).
150. S.S. Dietrich, B.L. Berman, At. Data Nucl. Data Tables **38**, 199 (1988).
151. M.P. Kelly, K.A. Snover, J.P.S. van Schagen, M. Kicińska-Habior, Z. Trznadel, Phys. Rev. Lett. **82**, 3404 (1999).
152. M.P. Kelly, J.F. Liang, A.A. Sonzogni, K.A. Snover, J.P.S. van Schagen, J.P. Lestone, Phys. Rev. C **56**, 3201 (1997).
153. D.R. Chakrabarty, M. Thoennessen, S. Sen, P. Paul, R. Butsch, M.G. Herman, Phys. Rev. C **37**, 1437 (1988).
154. A.M. Bruce, J.J. Gaardhøje, B. Herskind, R. Chapman, J.C. Lisle, F. Khazaie, J.N. Mo, P.J. Twin, Phys. Lett. B **215**, 237 (1988).
155. A. Stolk, M.N. Harakeh, W.H.A. Hesselink, H.J. Hofmann, R.F. Noorman, J.P.S. van Schagen, Z. Sujkowski, H. Verheul, M.J.A. de Voigt, D.J.P. Witte, Phys. Rev. C **40**, R2454 (1988).
156. J.P.S. van Schagen *et al.*, Phys. Lett. B **308**, 231 (1993).
157. J.P.S. van Schagen, M.N. Harakeh, W.H.A. Hesselink, R.F. Noorman, Nucl. Phys. A **581**, 145 (1995).
158. R.F. Noorman *et al.*, Phys. Lett. B **292**, 257 (1992).
159. R.F. Noorman *et al.*, Nucl. Phys. A **574**, 501 (1994).
160. S. Flibotte, B. Haas, P. Taras, H.R. Andrews, D.C. Radford, D. Ward, Nucl. Phys. A **531**, 205 (1991).
161. M. Gallardo, M. Diebel, T. Dossing, R.A. Broglia, Nucl. Phys. A **443**, 415 (1985).
162. D.R. Chakrabarty, M. Thoennessen, N. Alamanos, P. Paul, S. Sen, Phys. Rev. Lett. **58**, 1092 (1987).
163. M. Thoennessen, D.R. Chakrabarty, R. Butsch, M.G. Herman, P. Paul, S. Sen, Phys. Rev. C **37**, 1762 (1988).
164. R. Butsch, M. Thoennessen, D.R. Chakrabarty, M.G. Herman, P. Paul, Phys. Rev. C **41**, 1530 (1990).
165. N. Gelli *et al.*, Eur. Phys. J. A **7**, 361 (2000).
166. D.R. Chakrabarty, V.M. Datar, R.K. Choudhury, B.K. Nayak, Y.K. Agarwal, C.V.K. Baba, M.K. Sharan, Phys. Rev. C **53**, 2739 (1996).
167. A. Atac *et al.*, Phys. Lett. B **252**, 545 (1990).
168. F. Camera *et al.*, Phys. Rev. C **60**, 014306 (1999).
169. M. Mattiuzzi, A. Bracco, F. Camera, B. Million, M. Pignanelli, J.J. Gaardhøje, A. Maj, T. Ramsøy, T. Tveter, Z. Zelazny, Phys. Lett. B **364**, 13 (1995).
170. M. Thoennessen *et al.*, Phys. Lett. B **282**, 288 (1992).
171. T.S. Tveter *et al.*, Phys. Rev. Lett. **76**, 1035 (1996) and references therein.
172. M. Kmiecik, A. Maj, A. Bracco, F. Camera, M. Casanova, S. Leoni, B. Million, B. Herskind, R.A. Bark, W.E. Ormand, Nucl. Phys. A **674**, 29 (2000).
173. M. Kmiecik *et al.*, Phys. Rev. C **70**, 064317 (2004).
174. Srijit Bhattacharya *et al.*, Phys. Rev. C **77**, 024318 (2008).
175. Ish Mukul *et al.*, Phys. Rev. C **88**, 024312 (2013).
176. Ish Mukul *et al.*, J. Phys. G **41**, 115103 (2014).
177. O. Wieland *et al.*, Phys. Rev. Lett. **97**, 012501 (2006).
178. R.J. Wojtech, R. Butsch, V.M. Datar, M.G. Herman, R.L. McGrath, P. Paul, M. Thoennessen, Phys. Rev. C **40**, R2441 (1989).
179. M. Ciemala *et al.*, Phys. Rev. C **91**, 054313 (2015).
180. F. Gramegna *et al.*, Nucl. Instrum. Methods A **389**, 474 (1997).
181. M. Bruno *et al.*, Eur. Phys. J. A **49**, 128 (2013).
182. M. Ciemala, M. Kmiecik, M. Krzysiek, A. Maj, K. Mazurek, R. Charity, D. Mancusi, Acta Phys. Pol. B **44**, 611 (2013) and references therein.
183. F. Camera *et al.*, Phys. Lett. B **560**, 155 (2003).
184. P. Heckman *et al.*, Nucl. Phys. A **750**, 175 (2005).
185. S. Mukhopadhyay *et al.*, Phys. Lett. B **709**, 9 (2012).
186. Deepak Pandit, S. Mukhopadhyay, Surajit Pal, A. De, S.R. Banerjee, Phys. Lett. B **713**, 434 (2012).
187. Balaram Dey *et al.*, Phys. Lett. B **731**, 92 (2014).
188. C. Simenel, Ph. Chomaz, Phys. Rev. C **80**, 064309 (2009).
189. A. Stolk, A. Balanda, M.N. Harakeh, W.H.A. Hesselink, J. Penninga, H. Rijneveld, Nucl. Phys. A **505**, 241 (1989).
190. D.R. Chakrabarty, V. Nanal, V.M. Datar, Suresh Kumar, A. Mitra, E.T. Mirgule, R.G. Pillay, Nucl. Phys. A **770**, 126 (2006).
191. A.K. Rhine Kumar, P. Arumugam, Phys. Rev. C **92**, 044314 (2015).
192. D.R. Chakrabarty, V.M. Datar, Comment on ref. [191], submitted to Phys. Rev. C.
193. Sarla Rathi, Phys. Rev. C **74**, 024608 (2006).
194. R. Beringer, W.J. Knox, Phys. Rev. **121**, 1195 (1961).
195. S. Cohen, F. Plasil, W.J. Swiatecki, Ann. Phys. (N.Y.) **82**, 557 (1974).
196. W.D. Myers, W.J. Swiatecki, Acta Phys. Pol. B **32**, 1033 (2001).
197. A. Bracco, F. Camera, S. Leoni, Nucl. Phys. A **682**, 449 (2001).
198. A. Maj *et al.*, Acta Phys. Pol. B **32**, 2433 (2001).
199. A. Maj *et al.*, Eur. Phys. J. A **20**, 165 (2004).
200. A. Maj *et al.*, Nucl. Phys. A **731**, 319 (2004).
201. M. Kmiecik *et al.*, Acta Phys. Pol. B **36**, 1169 (2005).
202. Deepak Pandit *et al.*, Phys. Rev. C **81**, 061302 (2010).
203. D.R. Chakrabarty *et al.*, Phys. Rev. C **85**, 044619 (2012).
204. G. Enders *et al.*, Phys. Rev. Lett. **69**, 249 (1992).
205. H.J. Hofmann, J.C. Bacelar, M.N. Harakeh, T.D. Poelheken, A. van der Woude, Nucl. Phys. A **571**, 301 (1994).
206. R.A. Broglia, P.F. Bortignon, A. Bracco, Prog. Part. Nucl. Phys. **28**, 517 (1992).
207. A. Bonasera, M. Di Toro, A. Smerzi, D.M. Brink, Nucl. Phys. A **569**, 215 (1994).
208. J.J. Gaardhøje *et al.*, Phys. Rev. Lett. **59**, 1409 (1987).
209. A. Bracco, F. Camera, J.J. Gaardhøje, B. Herskind, M. Pignanelli, Nucl. Phys. A **519**, 47 (1990).
210. J.H. Le Faou *et al.*, Phys. Rev. Lett. **72**, 3321 (1994).
211. T. Suomijarvi *et al.*, Phys. Rev. C **53**, 2258 (1996).
212. P.F. Bortignon, A. Bracco, D. Brink, R.A. Broglia, Phys. Rev. Lett. **67**, 3360 (1991).
213. A. Smerzi, M. Di Toro, D.M. Brink, Phys. Lett. B **320**, 216 (1994).
214. P. Piattelli *et al.*, Nucl. Phys. A **649**, 181 (1999).
215. D. Santonocito *et al.*, Phys. Rev. C **66**, 044619 (2002).
216. A. Bonasera, F. Gulminelli, J. Molitoris, Phys. Rep. **243**, 1 (1994).
217. F. Amorini *et al.*, Phys. Rev. C **69**, 014608 (2004).
218. T.M.V. Bootsma, G.J. van Nieuwenhuizen, P.F. Box, R. Kamermans, P.G. Kuijter, C.T.A.M. de Laat, C.J.W. Twenhofel, P. Decowski, K.A. Griffioen, Z. Phys. A **359**, 391 (1997).
219. J.B. Natowitz, R. Wada, K. Hagel, T. Keutgen, M. Murray, A. Makeev, L. Qin, P. Smith, C. Hamilton, Phys. Rev. C **65**, 034618 (2002) and references therein.
220. PHENIX Collaboration (K. Adcox *et al.*), Nucl. Phys. A **757**, 184 (2005).
221. B.B. Back *et al.*, Nucl. Phys. A **757**, 28 (2005).

222. BRAHMS Collaboration (J. Arsene *et al.*), Nucl. Phys. A **757**, 1 (2005).
223. STAR Collaboration (J. Adams *et al.*), Nucl. Phys. A **757**, 102 (2005).
224. ALICE Collaboration (K. Arnold *et al.*), Phys. Rev. Lett. **105**, 252302 (2010).
225. ATLAS Collaboration (G. Aad *et al.*), Phys. Rev. Lett. **105**, 252303 (2010).
226. P.K. Kovtun, D.T. Son, A.O. Starinets, Phys. Rev. Lett. **94**, 111601 (2005).
227. N. Auerbach, S. Shlomo, Phys. Rev. Lett. **103**, 172501 (2009).
228. N. Dinh Dang, Phys. Rev. C **84**, 034309 (2011).
229. K.T.R. Davies, A.J. Sierk, J.R. Nix, Phys. Rev. C **13**, 2385 (1976).
230. L. Campajola *et al.*, Nucl. Phys. A **583**, 119 (1995).
231. M. Sandoli *et al.*, Eur. Phys. J. A **6**, 275 (1999).
232. D. Pierroutsakou *et al.*, Eur. Phys. J. A **16**, 423 (2003).
233. S. Flibotte *et al.*, Phys. Rev. Lett. **77**, 1448 (1996).
234. J.P. Martin *et al.*, Nucl. Instrum. Methods A **257**, 301 (1987) and references therein.
235. M. Colonna, N. Colonna, A. Bonasera, M. DiToro, Nucl. Phys. A **541**, 295 (1992).
236. D. Pierroutsakou *et al.*, Eur. Phys. J. A **17**, 71 (2003).
237. D. Pierroutsakou *et al.*, Phys. Rev. C **71**, 054605 (2005).
238. D. Pierroutsakou *et al.*, Phys. Rev. C **80**, 024612 (2009).
239. V. Baran, M. Cabibbo, M. Colona, M. Di Toro, N. Tsoneva, Nucl. Phys. A **679**, 373 (2001).
240. V. Baran, D.M. Brink, M. Colona, M. Di Toro, Phys. Rev. Lett. **87**, 182501 (2001).
241. M. Thoennessen, J.R. Beene, F.E. Bertrand, C. Baktash, M.L. Halbert, D.J. Horen, D.G. Sarantites, W. Spang, D.W. Stracener, Phys. Rev. Lett. **70**, 4055 (1993) and references therein.
242. M. Cinausero *et al.*, Nuovo Cimento **111**, 613 (1998).



Dipak Ranjan Chakrabarty is an experimental nuclear physicist. He received his doctoral degree in 1984 from the University of Mumbai during his tenure as a research scientist in the Nuclear Physics Division of the Bhabha Atomic Research Centre (BARC), Mumbai, India (1973–2012). He was at SUNY (Stony Brook) for two years (1985–87) as a post-doctoral fellow. He has worked on the topics of radiative proton and alpha capture, transfer reactions, giant dipole resonance in hot rotating nuclei, nuclear level density, molecular resonances and on the associated detector developments.



Nguyen Dinh Dang is a theoretical nuclear physicist. He received the degrees of candidate of physics and mathematical sciences from the Joint Institute for Nuclear Research (Dubna) in 1985 and doctor of physics and mathematical sciences from the Moscow State University in 1990. He is a RIKEN Nishina Center research scientist (Wako) and a senior scientist of the Institute for Nuclear Science and Techniques (Hanoi). The subjects of his research include nuclear collective excitations and properties of highly excited nuclei. Giant dipole resonance in hot rotating nuclei is a topic, which he has been studying in the last three decades.



Vivek Datar is a Senior Professor at Tata Institute of Fundamental Research, Mumbai since May 2015. After his PhD from the University of Mumbai (1983) he did post-doctoral work at IPN, Orsay, France (1986–87) and SUNY (Stony Brook), USA (1987–88). Before moving to TIFR he was at Nuclear Physics Division, Bhabha Atomic Research Centre (1975–2015). His areas of interest include low energy nuclear physics, tests of conservation laws and symmetries and neutrino physics. Presently he is part of a national effort, the India based Neutrino Observatory project, which aims to build a large underground laboratory at Pottipuram, Tamil Nadu.